High-Dimensional Mapping of the Immune Atlas in the Central Nervous System During Health, Aging and Disease

Dissertation

zur

Erlangung der naturwissenschaftlichen Doktorwürde

(Dr. sc. nat.)

vorgelegt der

Mathematisch-naturwissenschaftlichen Fakultät

der

Universität Zürich

von

Dunja Mrdjen

aus

Serbien & Südafrika

Promotionskommission

Prof. Dr. Burkhard Becher

(Vorsitz und Leitung der Dissertation)

Prof. Dr. Bernd Bodenmiller

Prof. Dr. Christian Münz

Prof. Dr. Ari Waisman

Zürich, 2018

Disclaimer

This thesis was based upon and adapted from the following publication:

High-Dimensional Single-Cell Mapping of Central Nervous System Immune Cells Reveals Distinct Myeloid Subsets in Health, Aging and Disease

Dunja Mrdjen, Anto Pavlović, Felix J. Hartmann, Bettina Schreiner, Sebastian Utz, Brian Leung, Iva Lelios, Frank L. Heppner, Jonathan Kipnis, Doron Merkler, Melanie Greter and Burkhard Becher.

And partially from the publications:

High Dimensional Cytometry of Central Nervous System Leukocytes During Neuroinflammation

Dunja Mrdjen, Felix J. Hartmann, Burkhard Becher.

and

The end of gating? An introduction to automated analysis of high dimensional cytometry data

Florian Mair*, Felix J. Hartmann*, **Dunja Mrdjen**, Vinko Toševski, Carsten Krieg, Burkhard Becher. *Contributed equally

Table of contents

Zusammenfassung

Das zentrale Nervensystem (ZNS) wurde lange Zeit als Ort eingeschränkter Immunüberwachung beschrieben. Allerdings stellt das ZNS ein strukturell stark unterteiltes Organ dar, welches aus dem Parenchym, den Ventrikeln, den verschiedenen Hirnhautschichten und aus mehreren dazwischenliegenden Barrieren besteht. In all diesen Strukturen befinden sich verschiedene Immunzellen, die unterschiedliche Rollen in der Überwachung von Geweben, in der Homöostase von Neuronen, der Immunabwehr, sowie in neurologischen Erkrankungen spielen.

Trotz der Bedeutung ZNS-residenter Immunzellen sind unsere Möglichkeiten diese Populationen zu charakterisieren und somit ihre unterschiedlichen Funktionen zu verstehen erheblich eingeschränkt. Eine eindeutige Unterscheidung zwischen den verschiedenen Immunzellen innerhalb des ZNS hing bisher überwiegend von Bildgebungsverfahren ab, bei denen die spezifische Zellform und deren Lokalisation zur Identifikation der Zellen diente. Darüber hinaus reagieren diese Zellen während einer Erkrankung des ZNS, was üblicherweise durch die Veränderung ihrer Morphologie beschrieben wird. Dies ist jedoch oftmals nicht eindeutig und erschwert somit die Unterscheidung zwischen verschiedenen ZNS-residenten Zelltypen und aus dem Blut einwandernden Zellen.

In dieser Arbeit setzen wir hochdimensionale Massen- und Durchflusszytometrie in Kombination mit Algorithmus-basierter Analyse ein, um ZNS Immunzellen auf unvoreingenommene Weise zu analysieren. Wir konnten alle im normalen ZNS der Maus vorkommenden Immunzelltypen eindeutig identifizieren und des weiteren die Existenz neuer Untergruppen von sogenannten “Border-assoziierten Makrophagen“ (BAMs) und deren spezifische Lokalisation nachweisen. Außerdem untersuchten wir verschiedene Formen von ZNS-Erkrankungen die beispielsweise im erhöhten Alter oder in Mausmodellen für Alzheimer und Multiple Sklerose eintreten und konnten sowohl krankheitsspezifische als auch krankheitsübergreifende Eigenschaften von Mikrogliazellen und BAMs identifizieren. Zusammengefasst tragen unsere Erkenntnisse somit zum Verständnis der Immunzelllandschaft des ZNS bei und stellen eine wichtige Ressource für die Erforschung von ZNS Krankheitsmechanismen, potentieller Biomarker und neuen Zielobjekten in der therapeutischen Behandlung dar.

Summary

The central nervous system (CNS) was long regarded as a site of limited immune surveillance. However, the CNS is a compartmentalized organ comprising the parenchyma, the ventricles containing the choroid plexus and cerebrospinal fluid, the meningeal layers which envelop the parenchyma, and several 'absolute' and semi-permeable barriers. Within these compartments are located various CNS-resident immune cell types with diverse roles in tissue surveillance, neuronal and brain tissue homeostasis, immune defense and neurological diseases.

Despite the importance of CNS-resident immune cells, our ability to fully characterize these populations and subsequently to understand their distinct functions has thus far been severely limited. Reliable discrimination between different immune cells within the CNS has largely depended on imaging techniques where their distinct patterns of localization provide a surrogate for their identification. Furthermore, during CNS pathology, CNS-resident immune cells become reactive. Reactive cells were commonly described by their morphological changes. However, these changes were often ambiguous, presenting a challenge in differentiating types of reactive CNS-resident cells as well as differentiating them from infiltrating blood-derived cells during neuroinflammatory diseases.

In order to overcome localization- and morphology-dependent limitations, we applied high-dimensional single-cell mass and fluorescence cytometry combined with algorithm-guided analysis. These techniques allow for the multiplexing of cell-identifying protein markers to an unprecedented scale and the unbiased analysis of immune cell populations. We unambiguously identified all the immune cells within the normal murine CNS and uncovered the existence of novel subsets within CNS border-associated macrophages (BAMs), further showing their enrichment in specific CNS compartments. We extended our analysis to different forms of CNS pathology, including aging and murine models for Alzheimer's disease and Multiple Sclerosis. We revealed that microglia, the main immune cells of the CNS, and BAMs exhibit disease-specific and -unspecific reactivity across CNS pathologies. Together, these data add to our understanding of the immune landscape of the CNS and provide a powerful resource for the study of CNS disease mechanisms, potential biomarkers and therapeutic targets.

Abbreviations

Aβ	amyloid-β
AD	Alzheimer's disease
amu	atomic mass unit
APC	antigen presenting cell
APP	amyloid precursor protein
BAMS	border-associated macrophage
BBB	blood-brain barrier
BSA	bovine serum albumin
CCR	chemokine (C-C motif) receptor
CLARA	clustering for large applications
CNS	central nervous system
CSF	cerebrospinal fluid
CyTOF	cytometry by time-of-flight
DAMP	danger-associated molecular pattern
DC	dendritic cell
DNA	deoxyribonucleic acid
DOTA	1,4,7,10-tetraazacyclododecane-1,4,7,10-tetraacetic acid
DTPA	diethylene triamine pentaacetic acid
E	embryonic day
EAE	experimental autoimmune encephalomyelitis
EDTA	ethylenediaminetetraacetic acid
FACS	fluorescence-activated cell sorting
FlowSOM	flow cytometry data analysis using self- organizing map
GFP	green fluorescent protein
ICP	inductively coupled plasma
IFN-γ	interferon gamma
IL	interleukin
Ir	iridium
ITCB	isothiocyanobenzyl
K	Kelvin
k-NNG	k Nearest Neighbor Graph
Ln	lanthanide
M	mass
M1	inflammatory macrophage
M2	tolerogenic macrophage

mAb	monoclonal antibody
MCB	mass-cell barcodin
MdC	monocyte-derived cell
MEM	Marker Enrichment Modeling
MHCII	major histocompatibility complex II
MS	Multiple Sclerosis
MST	minimum spanning tree
NFT	neurofibrillary tangles
One-SENSE	One-dimensional Soli-Expression by Nonlinear Stochastic Embedding
PAMP	pathogen-associated modeluclar pattern
PBS	phosphate buffered saline
PCA	principle component analysis
Pd	palladium
PFA	paraformaldehyde
PRR	pattern recognition receptor
Pt	cisplatinum
QC	quality control
RFP	red fluorescent protein
Rh	rhodium
RNA	ribonucleic acid
SAS	subarachnoid space
sc-	single-cell
s.c.	sub-cutaneously
Scaffold	single-cell analysis by fixed force- and landmark-directed
SH	sulfide
SOM	self- organizing map
SPADE	Spanning-tree Progression Analysis of Density-normalized Events
t-SNE	t-stochastic neighbor embedding
TAM	tumor-associate macrophage
TLR	toll-like receptor
TOF	time-of-flight

1. Introduction

1.1. The central nervous system has compartmentalized immune privilege

The central nervous system (CNS) is a highly compartmentalized organ which is protected by a series of layers and barriers that shield it from blood-borne pathogens and other threats, including potentially harmful inflammatory mediators. The brain itself was long regarded as a site of limited immune surveillance due to the lack of obvious lymphatic vessels, the presence of the blood brain barrier (BBB), and slow transplant rejection (Murphy and Sturm, 1923; Shirai, 1921). Thus, the functional contribution of the peripheral immune system to CNS homeostasis and neurological diseases was disregarded and the organ was considered to be "immune privileged". However, more sophisticated examination of the CNS by later studies revealed that the level of steady state immune privilege varies dramatically between compartments and is only really applicable to the parenchyma proper where neurons are found (Matyszak and Perry, 1996a). The meninges, perivascular spaces surrounding parenchymal blood capillaries, and the choroid plexus, contained within the brain ventricles, are not immune-restricted and harbor a variety of tissue resident leukocytes (Herz et al., 2017).

1.2. Protective borders and barriers separate CNS compartments

1.2.1. Meningeal layers

The different CNS compartments are separated by several 'absolute' and semi-permeable barriers (Shechter et al., 2013b). The meninges represent the first type of barrier (Figure I, a), located on the surface of the brain, and comprise three distinct layers: the thick dura mater on top, followed by the delicate, web-like arachnoid mater, shielding the CSF-containing subarachnoid space (SAS) which lies above the thin pia mater that intimately envelops the parenchyma across its entire convoluted surface area. The leptomeninges is defined as the layer of pia mater, SAS and arachnoid mater. The level of exclusion from the periphery increases with depth from the top down. The dura mater harbors arteries and veins which lack a proper BBB and are fenestrated rather than continuous. Further establishing the dura mater as connected to the periphery, recent studies in mice (Aspelund et al., 2015; Louveau et al., 2015), nonhuman primates and humans (Absinta et al., 2017) demonstrated that a lymphatic system lines the dural sinuses and drains fluid, macromolecules and immune cells from the CNS to the deep

cervical lymph nodes. The arachnoid mater is impermeable to fluids, forming a barrier that separates and shields the SAS containing the CSF from the dura mater. The pia mater separates the SAS from the parenchyma in the brain and spinal cord and also surrounds the SAS-blood vessels which emerge from the parenchyma, creating a blood-leptomeningeal barrier of tight-junction connected epithelial cells (Engelhardt et al., 2017).

1.2.2. Parenchyma and perivascular spaces

The second barrier, the BBB, is the strongest barrier against contact with the periphery and is only found in the parenchymal and leptomeningeal capillaries (Figure I, b). The BBB is formed mainly by the endothelial cells of the blood vessels which are connected by tight junctions and responsible for the controlled entry of solutes, molecules and ions into the brain parenchyma (Ransohoff and Engelhardt, 2012). The extravasation of immune cells is possible, but in steady state this only happens at the level of postcapillary venules where CSF filled perivascular spaces are present and where the further penetration of immune cells into the CNS parenchyma is blocked by the glia limitans (Owens et al., 2008). The glia limitans is a barrier formed by the association of astrocyte endfeet to the vascular basement membrane of the capillaries, it also covers the entire surface of the brain and spinal cord and is continuous with the subarachnoid space (Owens et al., 2008; Ransohoff and Engelhardt, 2012).

1.2.3. Choroid plexus

Lastly, a third barrier is formed by the epithelial cells of the choroid plexus (the blood-CSF barrier, Figure I, c), which generates the CSF and controls the movement of molecules between the blood and the CSF (Daneman & Engelhardt, 2017). The choroid plexus has also been proposed to regulate the passage of immune cells into the CSF, and is therefore considered the main site of immune surveillance within the CNS (Engelhardt et al., 2016). The choroid plexus stroma, however, is supplied by blood vessels that do not present a BBB and therefore solutes and immune cells can pass from the blood into the choroid plexus stroma (Engelhardt et al., 2017).

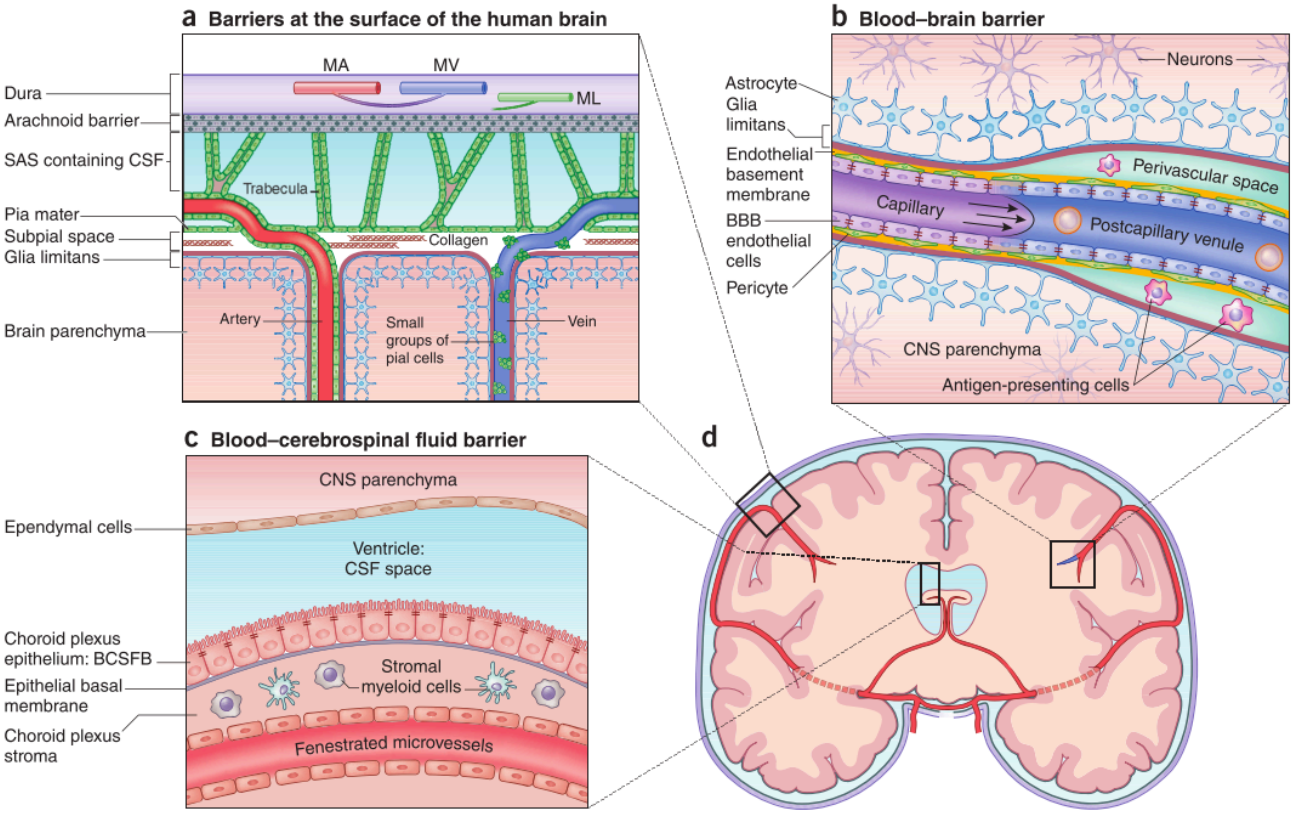

Figure I. The compartments of the CNS are separated by absolute and semi-permeable barriers. (a) Dura mater is supplied by meningeal arteries (MA) and veins (MV), and dural microvessels lack a BBB; the dura mater also contains lymphatics (ML). The dura is immediately adjacent to the arachnoid mater, which forms the outer blood-CSF barrier of the SAS. The pia mater coats veins and arteries in the SAS and surrounds arteries entering the brain forming the blood-leptomeningeal barrier. The glia limitans forms a barrier at the surface of the CNS parenchyma and around blood vessels. **(b)** Highly specialized BBB endothelial cells are coated by a basement membrane formed by the fusion of endothelial and glia limitans basement membranes. Pericytes are embedded in the endothelial basement membrane. CNS microvessels are surrounded by the glia limitans, which is composed of the parenchymal basement membrane and astrocyte end-feet. At postcapillary venules, the adjacent basement membranes leave a virtual perivascular space in which occasional APCs are embedded. **(c)** Choroid plexus epithelial cells establish the blood-CSF barrier. The choroid plexuses are localized in the ventricles of the brain and produce CSF. The choroid plexus stroma harbors DCs and macrophages and is supplied by a dense microvascular network that does not establish a BBB. **(d)** Schematic coronal brain section depicting the localization of the brain barriers. (Engelhardt et al., 2017, Nature Immunology.)

1.3. Immune sentinels within the CNS

1.3.1. Microglia

The parenchyma is the most protected and isolated compartment within the CNS, however it does host an important sentinel tissue-resident macrophage population: the microglia. As with tissue-resident macrophages in other organs throughout the body,

microglia develop from yolk-sac erythromyeloid progenitors and are seeded into the brain during embryogenesis on E8.5-E9 (embryonic day) in mice. This occurs before the establishment of the BBB, after which the brain is disconnected from the periphery and becomes "immune privileged" (Ginhoux et al., 2010). After brain colonization in the steady state, microglia are maintained by self-renewal without contribution from bone marrow monocytes (Ajami et al., 2007).

Microglia possess motile processes which form their characteristic branched morphology and are used to survey the parenchymal environment across long distances (Nimmerjahn et al., 2005). Disturbances in brain homeostasis can cause rapid and profound changes in microglial morphology, gene expression and function. Microglia were shown to actively move toward sites of tissue damage where they are involved in the elimination of debris after neuronal cell death (Hanisch and Kettenmann, 2007). Being immune cells, microglia are able to respond to infectious threats and recruit other immune cells to the brain to fight the infection. However, they also have important roles in the healthy and developing brain. Here they contribute to vascular formation (Checchin et al., 2006), alter neuronal circuits, phagocytose apoptotic neurons, contribute to synaptic maturation and pruning (Paolicelli et al., 2011; Roumier et al., 2004; Salter and Beggs, 2014; Tremblay et al., 2010). Furthermore, microglial depletion was shown to negatively influence the development of social interaction and impair learning abilities (Parkhurst et al., 2013; Zhan et al., 2014). The crucial surveying function of neuronal and synaptic homeostasis by microglia suggests that they also have important roles in neurodegenerative diseases. Indeed, there is mounting evidence linking microglia to the progression and pathogenesis of neurodegenerative diseases, however their exact contribution remains unclear and is further discussed below (Colonna and Butovsky, 2017; Prinz and Priller, 2014).

1.3.2. CNS border-associated macrophages: BAMs

Outside the brain parenchyma but within the CNS compartments, immune surveillance is thought to be mediated by rare populations of dendritic cells (DCs) as well as the more abundant macrophages. These macrophages line the meninges, choroid plexus and perivascular spaces (Bechmann et al., 2001; Goldmann et al., 2016; McMenamin, 1999). Since they are found within the border regions of the CNS and not within the

parenchyma, they can be called CNS "border-associated macrophages" (BAMs). For a long time, BAMs were thought to be bone-marrow derived cells. However, and similarly to early studies on the ontogeny of microglia, the majority of studies on BAM ontogeny were based on irradiation models and administration of chemotherapeutic drugs to deplete bone-marrow derived leukocytes (Aguzzi et al., 2013). These depletion approaches were responsible for an induced and artificial replacement of macrophages from blood monocytes, mostly because of the disruption of the BBB and production of chemo-attractants (Kierdorf et al., 2013; Mildner et al., 2007). Recent work using inducible fluorescent reporter proteins on macrophage progenitors, thus allowing for cell fate-mapping during embryogenesis, has elegantly shown that BAMs are actually seeded during development. Most likely they are seeded from the yolk sac but with a possible contribution from the fetal liver, and in that way they are similar to microglia and other tissue-resident macrophages (Goldmann et al., 2016) (Figure II). Goldmann and colleagues further demonstrated that BAMs that colonize the meninges and perivascular spaces are self-renewing and stable, while choroid plexus BAMs are slowly replaced from CCR2^{+} blood monocytes.

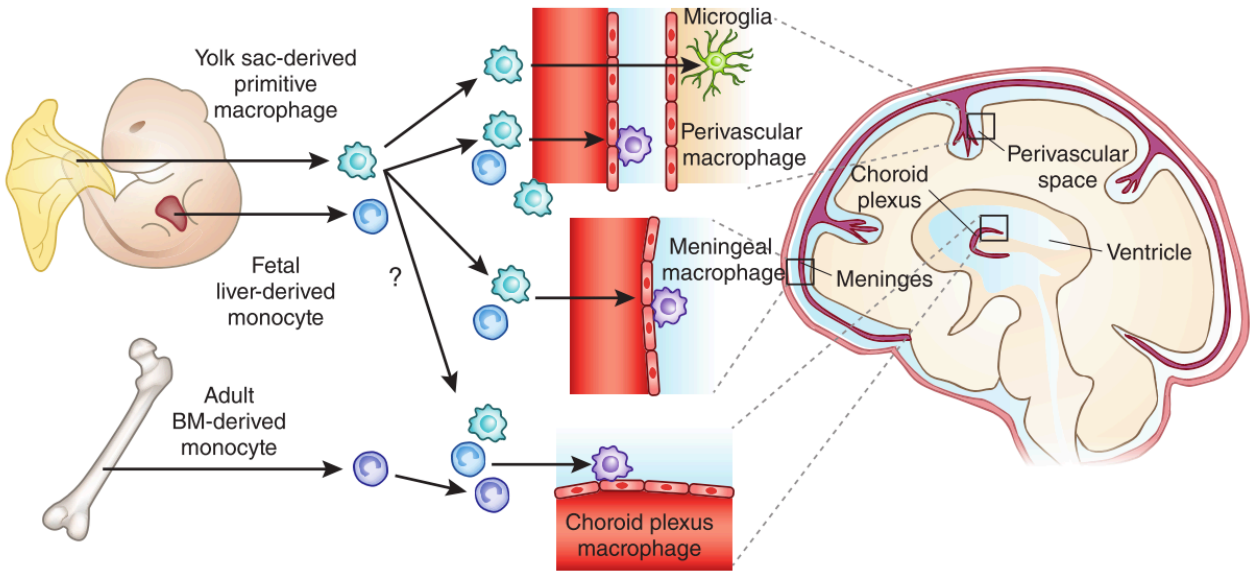

Figure II. Ontogeny of border-associated macrophages (BAMs) of the CNS. Adult microglia are derived exclusively from yolk sac progenitors. Perivascular and meningeal BAMs arise from embryonic precursors, most probably from yolk sac macrophage progenitors, with a potential contribution from fetal liver monocytes. Choroid plexus BAMs have a heterogeneous origin that encompasses adult bone marrow monocytes and embryonic precursors. (Greter, 2016, Nature Immunology).

While our knowledge on the complete functions of microglia in homeostasis and disease is still lacking, it is far ahead of what we know about the role of BAMs within the CNS, which is so far mostly based on speculation and hypothesis.

General macrophage functions throughout the body range from scavenger and professional phagocyte to tissue homeostasis and repair, remodeling of the extra-cellular matrix and angiogenesis. They have also been shown to maintain immune tolerance in the testes (Mossadegh-Keller et al., 2017) as well as in tumor microenvironments as highly problematic tumor-associated macrophages (TAMs) (Davies et al., 2013; Wynn et al., 2013). Heterogeneity within macrophage populations was initially described as a binary polarization profile based on an inflammatory (M1) and tolerogenic (M2) phenotype (Sica and Mantovani, 2012), defined by responses to the cytokine IFN-γ and activation of toll-like receptors (TLRs), or to IL-4 and IL-13 cytokines, respectively. However, this generalized categorization has since been proven inadequate as macrophages exist with a range of phenotypes and functional potential between the two extremes of M1 and M2. Transcriptional profiling of tissue-resident macrophages by the Immunological Genome Project showed that these populations have high transcriptional diversity with minimal overlap, suggesting that the many faces of the macrophage represent many unique classes (Gautier et al., 2012). In fact, macrophages are highly plastic cells which seem to adapt their identity and functional capacity according to largely uncharacterized niche-specific stimuli within their local microenvironments. Thus, it is logical to speculate that the function of BAMs may depend on their compartmental location within the CNS.

Early studies in the rat brain show that perivascular BAMs of the CNS are able to take up macromolecules injected into the blood stream or into brain ventricles, thus demonstrating their scavenger function (Kida et al., 1993; Mato et al., 1996). Like microglia, perivascular BAMs may play a role in blood vessel formation, however the distinction between microglia and perivascular BAMs was not clear in this study (Checchin et al., 2006). Another study demonstrated that perivascular and meningeal BAMs show early signs of activation in experimental allergic encephalomyelitis, preceding parenchymal invasion by peripheral leukocytes. Their depletion by stereotaxic injection of clodronate-containing liposomes into the fourth ventricle resulted in less severe disease symptoms (Polfliet et al., 2002), implying that they play a role in initiation of inflammation within the CNS. Applying the same liposome-

clodronate method in a mouse model for Alzheimer's disease (AD), perivascular BAM depletion was associated with a defective clearance of amyloid-β (Aβ) peptides in leptomeningeal and cortical blood vessels, in a phenomenon called cerebral amyloid angiopathy (Hawkes and McLaurin, 2009). BAMs were found to associate with β-amyloid peptides while microglia and astrocytes were not, thereby suggesting that the scavenger function of perivascular BAMs extends to potentially pathogenic proteins and could be harnessed in the treatment of proteopathies like AD and Parkinson's disease.

Importantly, BAMs have been shown to express MHCII in the steady state (Matyszak et al., 1992; McMenamin, 1999) while microglia do not, and because of their strategic locations at CNS interfaces, BAMs are thought to be competent CNS antigen presenting cells (APCs) (Becher et al., 2006; Prinz et al., 2017). This theory was strengthened when T cells were shown to interact with pial BAMs, allowing them to enter the CNS parenchyma during neuroinflammation (Schläger et al., 2016). However, the majority of these studies mainly based their conclusions on microscopy-based identification of cell types, in which the distinction between BAMs and microglia or DCs was unclear. Therefore, an unambiguous characterization of BAMs is necessary to understand and study their functions in both CNS homeostasis and disease.

1.3.3. CNS-resident dendritic cells

Classical DCs do not develop as early as tissue-resident macrophages but arise from precursors (pre-DCs) in the adult bone marrow. They have a relatively short life span of 1-2 weeks, are therefore constantly replenished from the bone marrow and their primary function is professional antigen presentation (Liu et al., 2009; Liu et al., 2007). DCs and macrophages (as well as neutrophils) are both professional phagocytes and surveyors, they both accumulate at sites of pathogen entry and are both capable of presenting antigen. However, DCs are highly specialized sensing and stimulating cells and the most efficient APCs. DCs phagocytose and process antigen, preserving "useful" material which is loaded onto MHCI and MHCII molecules with which DCs are the only APCs able to stimulate naïve and memory T cells (Savina and Amigorena, 2007). DCs are also patrollers. Migratory DCs patrol non-lymphoid tissues for antigen and migrate to lymphoid organs to stimulate adaptive immune responses, while

macrophages are more non-migratory sentinel cells. Furthermore, DCs are remarkably heterogeneous. Their distinctive subsets have been defined across different tissues (Guilliams et al., 2016b; Schlitzer and Ginhoux, 2013). Selective expression of antigen-sensing TLRs and pattern-recognition receptors (PRRs) (Merad et al., 2013) allows DCs to instruct tailored responses (inflammatory or tolerogenic) to particular pathogens, vaccines, tumors or self-antigens by the induction of specialized T helper cell subsets (Everts et al., 2016; Idoyaga et al., 2013; King et al., 2010; Schlitzer et al., 2013b; Tussiwand et al., 2015). Given the specialized and potent function of DCs to initiate or dampen adaptive immune responses, their presence in the CNS is highly relevant in the maintenance of a quiescent immune environment within the CNS and also in the context of initiating neuroinflammatory diseases.

Early studies that localized BAMs in rat tissue by rudimentary histology also found rare $OX6^+$ (rat MHCII equivalent), $OX62^+$ (rat CD11c equivalent) cells they called DCs within dura mater, leptomeninges and choroid plexus (McMenamin, 1999). Later histology stainings showed the presence of $CD209^+$ (DC-SIGN) DCs in the meninges of healthy human brains and not in the parenchyma (Serafini et al., 2006). Meningeal and choroid plexus DCs were then shown to have a life span of 5-7 days, and to be dependent on bone marrow progenitors and the FMS-like receptor tyrosine kinase 3 ligand (Flt3L) (Anandasabapathy et al., 2011) which is a hematopoetin required for the maintenance of peripheral DCs (Kingston et al., 2009; Waskow et al., 2008).

The functional relevance of CNS DCs as APCs was tested by co-culture experiments with sorted $CD11c^+$ meningeal DCs and T cells and found to potently activate T cell proliferation *in vitro* (Kivisäkk et al., 2009). During neuroinflammation, DCs are known to accumulate within the CNS. Early studies showed that DCs accumulate in the CNS perivascular space and adjacent parenchyma during neuroinflammation in the rat (Matyszak and Perry, 1996b). During Multiple Sclerosis (MS), $CD209^+$ DCs were shown to accumulate in the meninges and in perivascular spaces near MS lesions in close proximity to T and B cells, and also within the parenchyma (Serafini et al., 2006). A pivotal study demonstrated in experimental autoimmune encephalomyelitis (EAE), the mouse model for MS, that Flt3L-dependent $CD11c^+MHCII^+$ DCs were in fact sufficient and required for the reactivation of primed T cells and for the subsequent CNS invasion of peripheral leukocytes and progression of EAE (Greter et al., 2005). Indeed, $MHCII^+$ cells were shown *ex vivo* to interact with $CD4^+$ T cells in the

subarachnoid space during EAE (Kivisäkk et al., 2009). While these cumulative results show that CNS DCs are present in the steady state CNS and likely critical during neuroinflammation, these studies fall short of definitively assigning a non-redundant and essential role for DCs as the APCs at CNS borders during neuroinflammation. The reason for this is one of APC identity: Once again, a clear distinction between DCs and BAMs, BAMs being plastic cells that can upregulate CD11c during inflammation and can also express MHCII, as well as the distinction between DCs and monocyte-derived cells (MdCs) which invade the meninges, perivascular spaces and parenchyma during EAE and MS and also express CD11c and MHCII, was not established in these experiments. The relevance of properly identifying the CNS APC required for initiation of neuroinflammation is that DCs, BAMs and MdCs have different ontogenies, life spans, timed appearance in the CNS during inflammation, and may well have beneficial or detrimental functions during CNS diseases like MS. Therefore, therapies must be able to specifically target the right cell type.

1.4. The role of the immune system in brain pathologies

Since microglia are in direct contact with parenchymal neurons of the brain and spinal cord and other immune cells are considered to be excluded from the parenchyma in normal conditions, the role of microglia in brain pathologies has been studied extensively. Genetic associations and functional evidence implicates microglia in the pathogenesis of neurodegenerative diseases. However, whether the role of microglia is neurotoxic or neuroprotective may depend on the type of neurological disease and the timing during disease progression. The tilt toward harmful or beneficial outcomes is a highly regulated process and depends on the activating conditions and likely the cell-intrinsic age. Microglia express a wide range of sensing receptors (Hickman et al., 2013) and in response to different signals can change their morphology from a ramified to a spherical shape and move to sites of damage. Signals can be constitutively derived from normal neurons to maintain a calming, homeostatic state in microglia, or derived from infection, damaged cells or trauma and induce a range of reactive microglial states (phagocytic, pro-inflammatory) which can later progress to a more repairing state with elimination of the activating signals (Figure III).

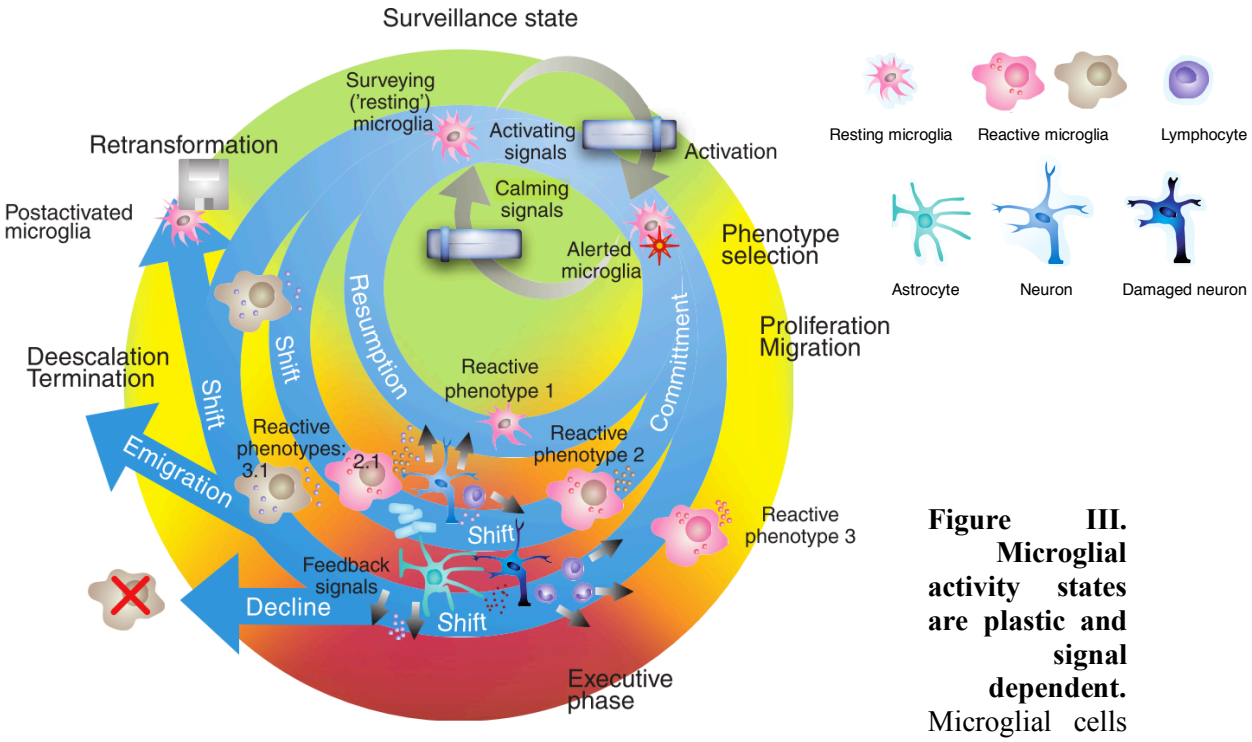

Figure III. Microglial activity states are plastic and signal dependent. Microglial cells in the surveillance (sentry) state—traditionally termed 'resting' state—constantly scan for signals that would indicate a potential threat to CNS homeostasis. The appearance of such 'activating' signals (in infection, trauma, cell impairment, hyperactive neurons) or the loss of constitutive 'calming' signals triggers a transition to an alerted state. Signals and their context are interpreted and converted to an initial response of 'activation'. Cells hence further commit to distinct reactive phenotypes, constituted by transcriptional profiles and phenotypic changes, and enter their executive phase (for example, release of cytokines and chemokines, phagocytic activity of damaged neurons and debris). Three examples are depicted (phenotypes 1, 2, 3), but the diversity could be larger. Throughout the subsequent period, the reactive behavior of microglia may change (reactive phenotypes 2.1, 3.1), largely controlled by a fading (or elimination) of the initial activating signals as well as influences from astrocytes and neurons, or invading immune cells (illustrated as feedback signals, grey arrows). Reactive phenotypes may thus shift, eventually leading to a more repair-orientated profile. While some cells may die (indicated by an 'X' over cell), others may revert to a 'resting' (surveying) state. Some cells may not retransform to a completely naive status and may remain as 'post-activated' microglia. These cells could keep subtle changes, for example, in transcriptional activity, that affect their sensitivity to constitutive (calming) signals or alter responses to subsequent stimulation. Post-activated microglia could thus have acquired some experience (indicated as memory in the figure by a floppy disk icon). Figure and legend adapted from (Hanisch and Kettenmann, 2007).

1.4.1. Neurodegenerative diseases and dementia

1.4.1.1 The aging brain

During aging, chronic inflammation in the body gradually and increases, a process termed “inflammaging”. On the other hand, immune response to infection gradually becomes less potent due to immune-senescence (Deleidi et al., 2015). The effects of aging on microglia are conceivably 2-fold: microglia may react to aging-related changes in their environment, and microglia may be directly affected by the aging process. In the aging brain, microglia change morphology from a highly ramified “resting” cell to a “dystrophic” cell characterized by de-ramification, the presence of shortened tortuous processes, and/or cytoplasmic fragmentation (Streit et al., 2004). The cause of the dystrophic state of microglia in aging may be due to chronic systemic inflammaging and senescence. However, it is consistently reported that the total number and density of microglia increases with age in various brain regions (Reu et al., 2017). Therefore, dystrophic microglia may not be senescent in their potential to replicate and may resemble activated microglia. The hallmarks of microglial aging may also sometimes be characterized as dysfunctional and even hyper-reactive responses.

Myelin debris has been demonstrated to accumulate in aging microglia, in which it forms insoluble, lipofuscin-like lysosomal inclusions and likely contributes to their increased density (Safaiyan et al., 2016). Population-based autopsy studies of the brains of aged people who had not been diagnosed with a neurological disease consistently report the presence of protein aggregates like amyloid plaques, neurofibrillary tangles, Lewy bodies, inclusions of TAR DNA-binding protein 43, as well as synaptic dystrophy, the loss of neurons and the loss of brain volume in most of the brains (Elobeid et al., 2016). It is unknown what causes such lesions and whether they are the precursors to neurodegeneration and disease or simply the products of brain aging and microglial dystrophy (Figure IV) (Wyss-Coray, 2016).

1.4.1.2. Alzheimer’s disease

Over 46 million people worldwide live with dementia today. Late onset AD is the most common cause of dementia in the elderly. The processes that characterize AD

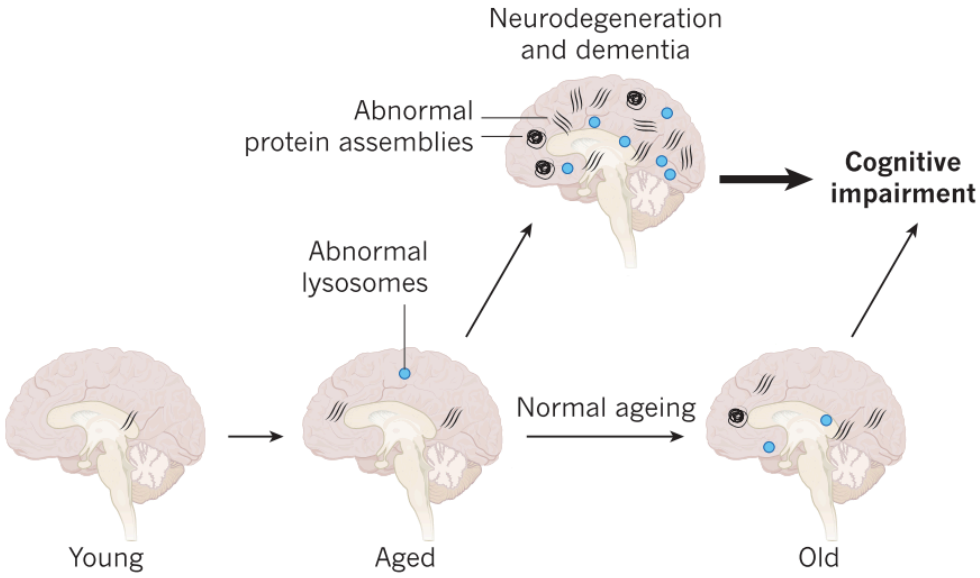

Figure IV. Aging and neurodegeneration. As the brain ages, abnormal protein assemblies and inclusion bodies take hold and abnormal lysosomes are observed more frequently. It is unclear whether these defects promote aging and neurodegeneration or whether they are innocent bystanders. Aged brains become highly prone to neurodegenerative diseases in which the same lesions amass as those that are found in old brains in smaller numbers. The relationship between such lesions and cognitive impairment is often blurred and normal aging and neurodegeneration and dementia can overlap. Figure adapted from (Wyss-Coray, 2016).

take place in most old brains; however, some people might have compensatory mechanisms that enable them to cope with these processes and to maintain normal cognition. Accordingly, it may be that AD phenotypes represent an exaggerated state of microglia dysfunction beyond that observed during normal aging (Wyss-Coray, 2016).

AD pathology is distinguished by the presence of both amyloid plaques and neurofibrillary tangles (NFTs). Extracellular plaques deposited in the brain parenchyma consist predominantly of Aβ peptides derived from the amyloid precursor protein (APP), which is an integral membrane protein expressed in many tissues and concentrated in the synapses of neurons in the brain. NFTs consist of intracellular deposits of aggregated, hyper-phosphorylated tau protein within neurons. Aβ plaques begin to form in the brain about 15–25 years prior to the onset of cognitive decline or the development of tau pathology (Ulrich et al., 2017), and can disrupt synaptic

transmission, induce oxidative stress and trigger cell death in vitro (Benilova et al., 2012).

The link between AD and the immune system gained a lot of interest when Genome-Wide Association Studies (GWAS) demonstrated strong genetic implications for microglial molecules and the immune system in general with AD. Most prominent was the identification of the R47H loss-of-function mutation in *TREM2* ("triggering receptor expressed on myeloid cells 2") as a major risk factor for AD (Guerreiro et al., 2013; Jonsson et al., 2013). *TREM2* is an innate immune receptor expressed exclusively by microglia within the parenchyma and thus provided the clearest link between microglial dysfunction and AD pathogenesis. However, whether this link is causal is still unclear, and whether microglia act as a friend or a foe in AD may depend on the time point during the disease progression and the location within the brain.

In a mouse model for AD, Aβ plaques formed rapidly within 24 hours and subsequently recruited activated microglia to the plaques within 1–2 days (Meyer-Luehmann et al., 2008). This dispelled previous notions that microglia may actually contribute to plaque formation. Microglia are activated by Aβ via various pathogen- or danger-associated molecular patterns (PAMPs, DAMPs) within the microglial sensome, including TRL-4 and its co-receptor CD14 (Lucin and Wyss-Coray, 2009; Reed-Geaghan et al., 2009). Microglia phagocytose Aβ well *in vitro*, however there was no clear consensus *in vivo* as to whether microglia possess the capacity to clear Aβ. When microglia were depleted from the brains of adult AD mice, there was no effect on Aβ dynamics, suggesting that aged microglia may not be actively phagocytosing and clearing plaques in the AD brain (Grathwohl et al., 2009). The only time that microglia were able to reduce plaque load was after adult microglia were depleted and replaced with juvenile microglia in organotypic hippocampal slice cultures (Hellwig et al., 2015). Perivascular macrophages and infiltrating monocyte derived macrophages take up and degrade Aβ more efficiently than adult microglia (Hawkes and McLaurin, 2009; Majumdar et al., 2008). However, parabiosis experiments showed that when wild-type mice are joined with GFP mice, GFP monocytes do not enter the brain under normal conditions or after CNS insult (Ajami et al., 2007).

While microglia may only play a minor role in amyloid clearance *in vivo*, they may contribute to secondary neurodegeneration via release of neurotoxic factors. However, recent studies have pointed towards a neuroprotective role for microglia during AD,

demonstrating that microglia act like garbage compactors, tightly surrounding Aβ plaques and making them less damaging to surrounding neurons (Condello et al., 2015). This barrier formation was abrogated in *TREM2*$^{-/-}$ AD mice (Yuan et al., 2016). While only about 0.5% of AD patients actually have a loss-of-function *TREM2* mutation, defective microglial barrier function may arise due to dystrophic senescence of microglia with age (Condello et al., 2017).

1.4.2. Neuroinflammation

While the cause of neurodegeneration in dementia and AD is still unclear, neuroinflammatory diseases are a direct result of strong inflammation within the CNS, either against a foreign pathogen or in an autoimmune reaction. In aging and AD there are subtle changes in microglial morphology, while in neuroinflammatory disease the entire immune landscape changes dramatically. CNS-resident immune cells become activated and the entire CNS is infiltrated by inflammatory leukocytes from the periphery (Galea et al., 2007). Microglia, DCs and BAMs, together are likely to be key to these processes, whether during initiation or propagation of neuroinflammation.

1.4.2.1. Multiple sclerosis

MS is one of today's most prevalent autoimmune diseases, affecting almost 10'000 patients in Switzerland (Pugliatti et al., 2006) and about 2.5 million worldwide. MS is a chronic inflammatory disorder of the CNS, i.e. the spinal cord and brain, resulting in demyelination, axonal degeneration and disability. The pathological hallmark of MS is lesions or plaques found in the white and grey matter of the CNS. Infiltrating inflammatory leukocytes cause demyelination and loss of oligodendrocytes (neuroglial cells which normally insulate axons and produce myelin) at these MS lesions (Dendrou et al., 2015). MS presents with a heterogeneous set of clinical features. Frequently observed signs are cognitive impairments like attention deficits, fatigue, visual disturbances such as reduced color vision and acuity as well as affection of motor functions manifesting as poor balance, limb incoordination or spasms (Compston and Coles, 2008).

EAE is currently the best model used to study MS and while it is an artificially induced autoimmune disease and does not capture fully the complexity of MS progression, it is still the gold standard (Schreiner et al., 2009). During EAE and likely MS as well, infiltration starts in the meninges and proceeds deeper into the parenchyma (Kivisäkk et al., 2009). While meningeal infiltration is antigen independent, parenchymal infiltration is antigen dependent (Lodygin et al., 2013) and has already been discussed in this thesis. During EAE, infiltrating auto-reactive T cells recruit inflammatory monocytes through production of the cytokine GM-CSF (Croxford et al., 2015b). Inflammatory monocytes differentiate into MdCs which may be a mixture of monocyte-derived DCs and macrophages, and it is MdCs which are thought to cause the destructive demyelination (Spath et al., 2017; Yamasaki et al., 2014).

As in aging and AD, the role of microglia during EAE and MS is still unclear. Microglia lose their homeostatic morphology in MS lesions (Zrzavy et al., 2017). For many years the distinction between MdCs and activated microglia in the inflammatory setting of EAE and MS has been challenging as their morphological and phenotypic features become merged due to activation within the inflammatory environment. Again, use of irradiation methods to deplete and transplant traceable bone-marrow derived cells and study radiation-resistance microglia proved misleading due to the artificial disruption of the BBB and contribution of monocyte-derived microglia to the microglial pool (Ajami et al., 2007). However, using genetic reporters to discriminate these cells and high-resolution imaging techniques, microglia were shown to be have myelin inclusions but were relatively inert during onset of EAE (Yamasaki et al., 2014).

Despite the technical drawbacks, most data point to a generally detrimental role of microglia in EAE and MS. Expression of the co-stimulatory molecule CD40 (Becher et al., 2001) or the cytokine IL-23-p40 (Becher et al., 2003) by microglia worsened EAE symptoms. Paralysis of microglia through genetic activation of the toxic ganciclovir derivative also worsened EAE symptoms (Heppner et al., 2005). Microglia may contribute to neurodegeneration during MS as the "calming" regulatory molecules CD200 and CD47 ("don't eat me signal") normally expressed by neurons are down-regulated within the center of chronic active MS lesions as well as the surrounding normal-appearing white matter (Koning et al., 2007).

Importantly, our current knowledge about how CNS-resident immune cells react during CNS pathologies has depended largely on ambiguous morphological changes and a few

select protein markers. Better tools and cell type-specific markers are required to clearly distinguish these cells from each other and from infiltrating inflammatory cells, and to compare the range of responses they have under different pathological conditions.

1.5. High parameter cytometry techniques

1.5.1. Fluorescence-based cytometry

Fluorescence-based cytometry (or flow cytometry) is a critical technique in the study of the immune system. A flow cytometer counts different types of cells in a liquid suspension that are passed rapidly in a stream within the flow cell, by their expression of specific surface or intracellular markers (receptors, cytokines, nucleic acids, genetic reporter proteins). The detection of these markers on cells is enabled by their labeling with antibodies that have been conjugated with unique fluorescent dyes (fluorophores or colors), and a series of lasers and photonic detectors within the cytometer. Since its inception in 1965 (Fulwyler, 1965) and its first use in the 1970s (Gray et al., 1975), the basic design of a flow cytometer has remained almost unchanged, highlighting the robust design of the technology (Robinson and Roederer, 2015). The epidemics of HIV/AIDS in the 1980s gave a dramatic impulse to flow cytometry, since it became clear that the quantification of the number of peripheral blood $CD4^+$ T cells was crucial to follow the course of the infection, and eventually for monitoring the therapy (Cossarizza et al., 2017). Since then, flow cytometry has established itself as the workhorse for high-throughput quantitative analysis of cells and other particles. Other aspects contributing to the success of flow cytometry include the speed at which cells are analyzed (allowing large numbers of cells to be measured), the high accuracy and resolution and the low operating costs per sample. Importantly, flow cytometry is regarded as a non-destructive technology, being able to viably sort cell populations for further subsequent analyses.

Flow cytometry also has some considerable limitations. While 18-color flow cytometry is now routinely used in labs, the immune system is far more complex than the number of individual fluorochromes available and our ability to detect and resolve them with respect to the overlap between their induvial emission spectra (a phenomenon termed spectral overlap). The number of commercially available fluorochromes has steadily

risen over the years. The optical setup (including laser, detector and filter configurations) able to detect them within the cytometer has recently advanced with the emergence of the Becton Dickinson FACSymphony flow cytometer which technically allows the measurement of up to 50 parameters. In practice, however, this high is number not achievable because at the moment the range of appropriate fluorescent dyes is limited.

1.5.2. Mass cytometry

1.5.2.1. The principle of mass cytometry

An alternative cytometry based technique has been developed that relies on antibodies labeled with non-radioactive heavy-metal isotopes instead of fluorophores, detecting the resulting signals using a time-of-flight (TOF) mass spectrometry detector (Bandura et al., 2009; Bendall et al., 2012; Ornatsky et al., 2010; Tanner et al., 2013). This method has been termed "mass cytometry" and became commercially known as the "CyTOF" (cytometry by time-of-flight), allowing the theoretical detection of more than 100 parameters per cell (Bendall et al., 2012; Tanner et al., 2013). Practically however, the limit is currently somewhere near 50, due to availability of isotopically pure metals. The technological advance of the metal-tagged antibody detection by TOF in CyTOF over the fluorescence-tagged antibody detection by optical detectors in flow cytometry is a giant leap in the field and is based on the circumvention of spectral overlap phenomenon with the use and detection of unique metal isotopes discretely separated by one atomic mass unit (amu) and having less than 1 part in 10^6 overlap (0.0001 %) in the adjacent mass channels (Tanner et al., 2013) (Figure V).

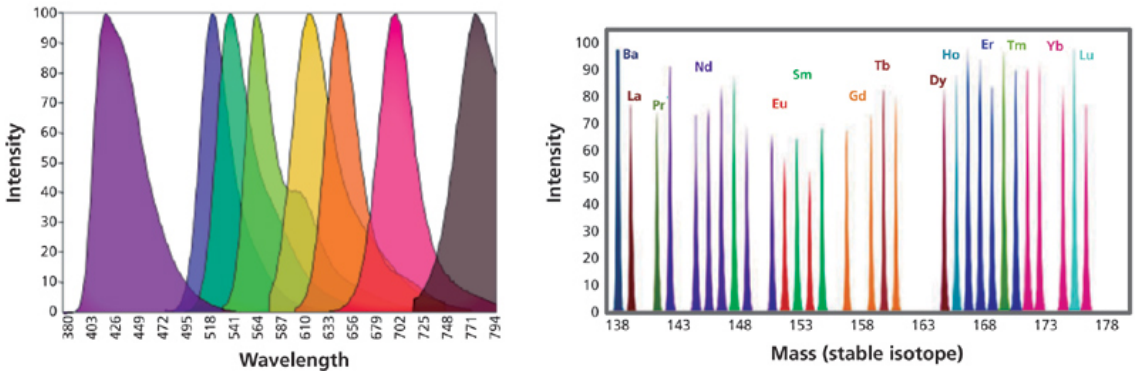

Figure V. Fluorophore emission and heavy-metal isotope spectra used in flow and mass cytometry, respectively. An eight-parameter flow cytometry experiment illustrating the spectral overlap between the fluorophores. Mass cytometry involves the collection of mass spectral data in distinct isotope channels with 1 atomic mass unit space between each channel. (Virani & Tanner, 2015)

The workflow and acquisition process in CyTOF is described in Figure VI. Cell suspensions stained with heavy-metal isotope tagged antibodies are injected into the mass cytometer where they reach a nebulizer which creates single-cell droplets from the cell suspension. These droplets are introduced into an inductively coupled plasma (ICP) (Houk et al., 1980). This ICP is high-temperature (7000°K at the surface to 55'000°K at the core), supported by a flowing argon stream, and vaporizes, atomizes and subsequently ionizes the cells (Tanner et al., 2013). The resulting ion cloud if then filtered through a quadrupole which allows only heavy-metal ions (which are not normally found in cells) to pass but blocks the low mass ions of biological elements commonly found in cells. Lastly, the ion cloud is divided into pushes and the metal isotopes are quantified by the TOF mass analyzer. The data is stored in the flow cytometry standard (*.fcs) file format which is compatible with standard flow cytometry data analysis software (like FlowJo).

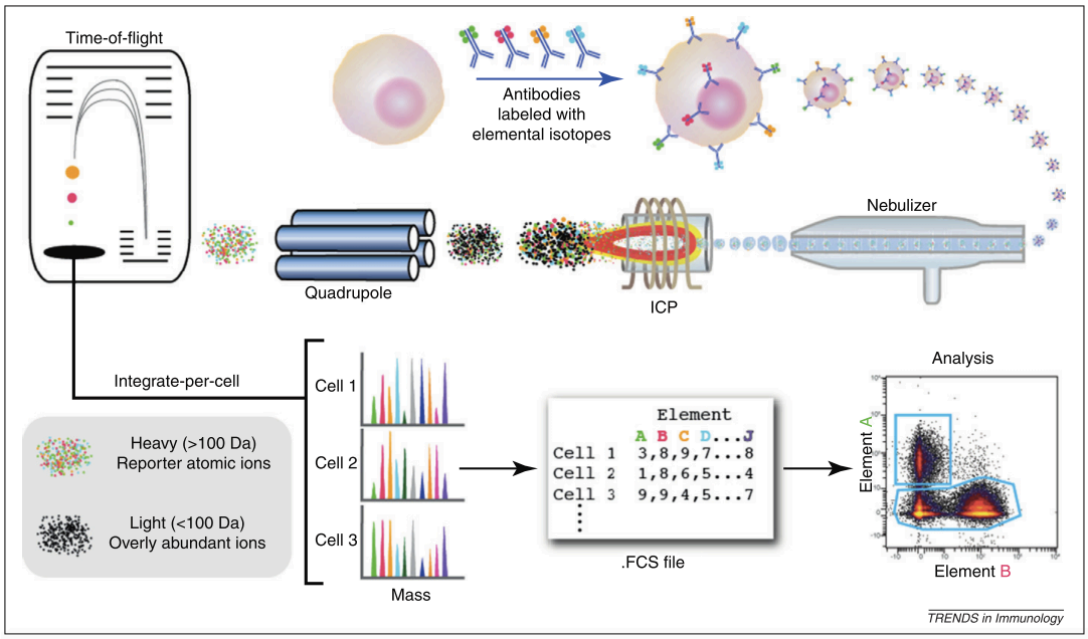

Figure VI. Schematic of ICP-mass spectrometry-based analysis of cellular markers. An antibody tagged with a specific mass isotope binds to the cellular epitope on the cell. The cell is introduced into the ICP by droplet nebulization. Each cell is atomized, ionized, overly abundant ions removed, and the elemental composition of remaining heavy elements (reporters) is determined. Signals corresponding to each elemental tag are then correlated with the presence of the respective marker and analyzed using conventional cytometry platforms. (Bendall et al., 2012)

1.5.2.2. Antibody conjugation with metal tags

An important part of CyTOF technology is the conjugation of antibodies with heavy-metal isotope tags. This is achieved by complexing the desired metal isotopes, as ions from a salt solution, into metal chelating polymers which are then covalently bound to the antibodies or directly to proteins within fixed and permeabilized cells. The elemental metals used have low natural abundance, thus exhibiting a very low background signal during acquisition. The range of elemental metals currently available in high enough purity and used in mass cytometry as shown in Figure VII. The mass range of the detector is currently 75 – 209 amu. The focus for panel antibody labeling is on the lanthanide (Ln) series of elements because of the large number of stable resolvable isotopes having similar chemistry that facilitates their incorporation into the same chelating polymer structure, as well as the peak of detector sensitivity within that mass range. Platinum (Pt) can be used to discriminate dead cells as it binds non-specifically to exposed proteins within membrane-compromised (dead) cells (Fienberg et al., 2012). Iridium (Ir) and rhodium (Rh) can be used as a cell ID markers (important

since there is no forward and side scatter) as they intercalate with DNA (Ornatsky et al., 2008). Palladium (Pd) can be used for mass-cell barcoding (MCB) of samples which allows for the pooling of samples (Zunder et al., 2015a). Staining and acquiring pooled samples prevents inter-staining variability and normalizes the signal drift that occurs during acquisition, respectively.

By attaching 3 to 4 polymers to one antibody, about 100 metal ions can be coupled to a single antibody (Ornatsky et al., 2010). Polymers are purchased attached to a linker that binds either reduced sulfide (-SH) groups on the Fc portion of the antibody or to amine groups within the cell. The choice of chelator depends on the binding affinity for the metal ion as well as its binding to regions of the antibody. Prominent polymer chelators at the moment are based on DTPA (diethylene triamine pentaacetic acid) (Majonis et al., 2010), a version of which forms the commercial MaxPar X8 polymer, and DOTA (1,4,7,10-tetraazacyclododecane-1,4,7,10-tetraacetic acid) (Lou et al., 2007), which are usually attached to a thiol-reactive maleimide linker. These polymers form high affinity complexes with Ln^{3+} ions. Partial reduction of antibodies results in breaking disulfide bonds on the Fc portion of antibodies, exposing -SH groups which then bind the linker on the metal loaded chelator. Full reduction of the

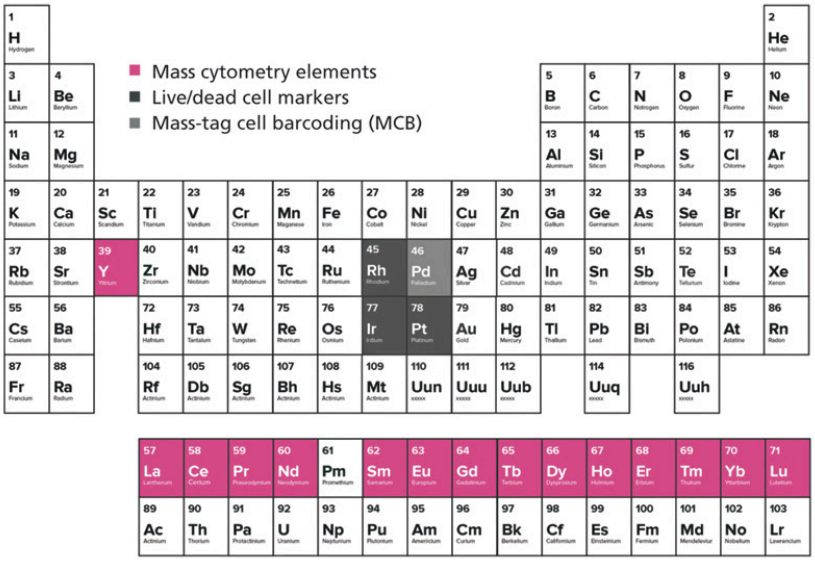

Figure VII. Heavy-metal isotopes currently available for mass cytometry. The stable isotopes of these 24 elements provide over 50 unique tags for use in mass cytometry. Sn (tin) has also shown promise for use in mass-tag cell barcoding with 10 available pure isotopes (personal correspondence with Christoph Schwärzler). Figure taken from Fluidigm.

antibody is undesirable as it would also expose -SH groups within the antigen-binding region of the antibody, thus disrupting its immune specificity.

ETDA-based chelators are better suited to Pd^{2+} ions (Majonis et al., 2011) and when linked to ITCB (isothiocyanobenzyl, also called p-SCN) (Zunder et al., 2015a) can directly bind to amine-reactive groups within the cytoplasm of fixed and permeabilized cells and is therefore useful for MCB. ITCB-EDTA-Pd has also be used to bind the human CD45 antibody for live cell barcoding (Mei et al., 2015), however, in our hands this did not work for mouse CD45. Other strategies are possible, including different combinations of metal-chelator-linker or even direct antibody labeling with metal, for example the use of platinum to directly label partially reduced antibodies (Mei et al., 2016) or the use of free metal salts like palladium or tin (Sn) to directly stain fixed or live cells (personal observations and correspondence with Christoph Schwärzler). Thus, there are currently great efforts being put into optimizing the metal conjugation procedure for various antibodies, metals and mass-cell barcoding strategies for fixed and live cells.

1.6. Algorithm-guided analysis of high parameter cytometry data

1.6.1. Limitations of manual data analysis

While both fluorescence-based flow cytometry as well as mass cytometry provide a technological platform to interrogate the immune system at a previously unprecedented level, scientific progress depends on our ability to analyze and comprehend the resulting data in a meaningful way. Historically, flow cytometric data was and still is being analyzed using a series of two-dimensional plots and manual "gating", i.e. drawing regions of interest (gates) on a plot and either examining that subset on a different bivariate plot or reporting a certain qualitative measure (cell subset is present or absent, or its relative proportion) or quantitative measure (signal intensity in a particular channel). While this approach is still adequate for many experimental settings, it suffers from several serious shortcomings. First, it is not easily scalable, as the number of two-dimensional plots increases exponentially with the number of measured parameters (i.e. an 18-parameter experiment would require a total of 153 two-dimensional plots to display every marker combination) and thus cannot be easily

comprehended anymore. Second, it has been shown by many multi-center studies such as the Human Immune Genome Project that manual gating is one of the largest variables in the outcome of a flow cytometry based experiment, and is thus not easily reproducible (Maecker et al., 2012). Third, every manual gating approach relies on prior knowledge of the researcher, thus introducing a bias towards “expected" results. Due to this focus, much of the potentially relevant and novel information within the dataset might not be recognized and end up being ignored.

1.6.2. Dimensionality reduction – visualizing a similarity landscape

A powerful tool to visualize multi-parameter cytometry data is nonlinear dimensionality reduction via t-stochastic neighbor embedding (t-SNE) (Amir et al., 2013; Van Der Maaten and Hinton, 2008). The difference between t-SNE and the commonly used dimensionality reduction algorithm, principle component analysis (PCA), is that PCA assumes linear relationships between the measured parameters, meaning that co-expression or co-variance of molecules is linearly correlated with important progressions in cellular identity or trajectories in data space. However, this is not the case for many biological datasets (Diggins et al., 2015). t-SNE visualizes high-dimensional similarities of cells in an easily understandable two- or three-dimensional scatter plot, the so-called t-SNE map. The proximity of cells in the t-SNE map reflects their distances in the high-dimensional space. Cells that are similar in their analyzed protein-expression pattern will be located closely together in the t-SNE map, thus enabling the visualization of different cellular subpopulations. However, this is only true to a certain extent: the more dissimilar the cells are, the less proportional to their dissimilarity the distance between them becomes. This is to prevent overcrowding of the center of the t-SNE map and preserves the local structure of the data while potentially exaggerating global structure (i.e. some different cells may appear to be more different than they really are) (Van Der Maaten and Hinton, 2008). Importantly, t-SNE has been shown to successfully identify small immune subpopulations (Amir et al., 2013) and is able to recognize high-dimensional associations of markers which might be missed when performing conventional, two-dimensional gating (Figure VIII).

Briefly, the computational steps underlying t-SNE are first the calculation of a pairwise similarity matrix for all data-points, based on their high-dimensional distances. Next, a

low-dimensionality similarity matrix is calculated based on initially random locations for each cell in the two (or three) t-SNE dimensions. In an iterative process, the algorithm then tries to minimize the difference between the high- and low-dimensional similarity matrices, thereby adjusting every cell´s position in the two-dimensional space (Van Der Maaten and Hinton, 2008). Recent improvements make use of the Barnes-Hut algorithm (van der Maaten, 2013) which uses a tree-like structure to reduce the number of pairwise similarities that actually have to be calculated. This now allows for a higher number of cells to be analyzed and shorter computation time. On the resulting t-SNE map, different immune subpopulations might visually appear as distinct clusters, however t-SNE does not per se assign single cells to defined clusters. This can be accomplished either by subsequent manual gating on the t-SNE map or by using automated clustering algorithms (Figure VIII, b).

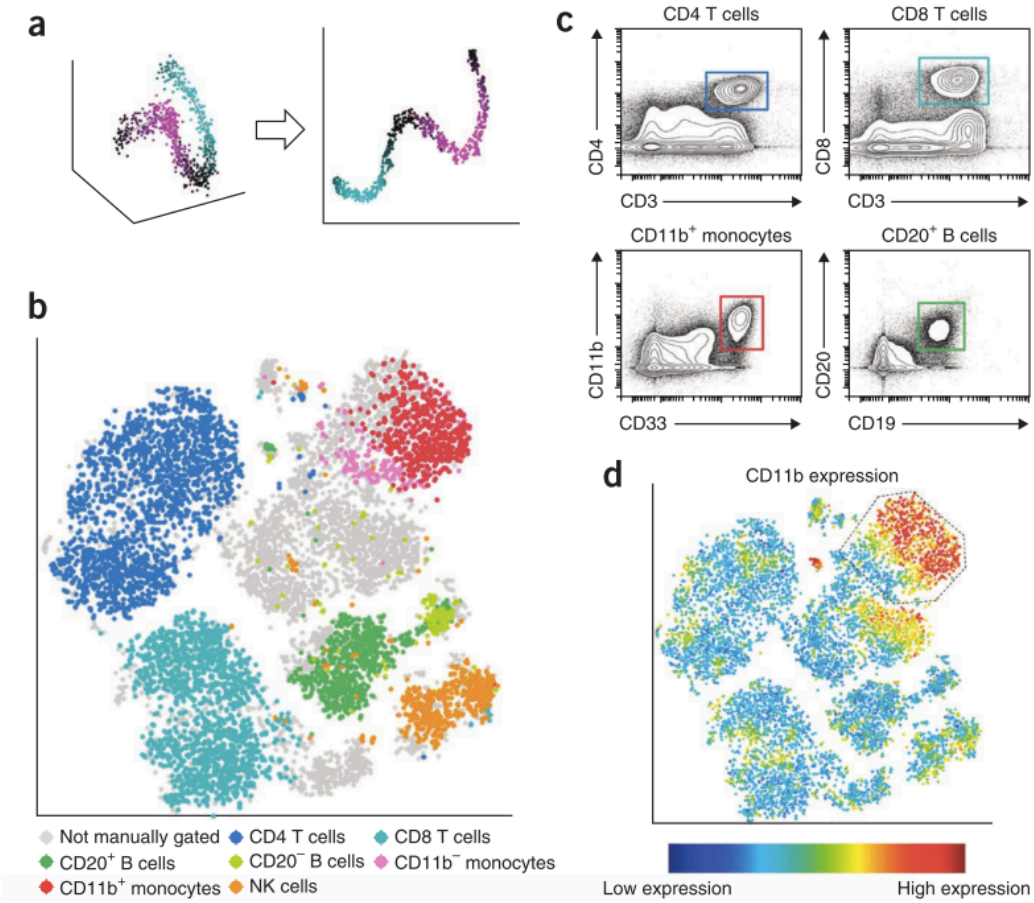

Figure VIII. viSNE map of healthy human bone marrow. (a) In a synthetic toy example, (1,000 points randomly distributed with normally distributed noise around a polynomial of the third degree) viSNE projects a one-dimensional curve embedded in three dimensions (left) onto two dimensions (right). The color gradient shows that points that are in close proximity in three dimensions remain in close proximity in two dimensions. (b) Application of viSNE to a healthy human bone marrow sample, stained with 13 markers and measured by mass cytometry, automatically separates cells into spatially distinct subsets based on the combination of markers that they express. Each point in the viSNE map represents an individual cell and its color represents its immune cell subset as designated by independent expert manual gating (manual gates are defined at the bottom). Gray points were not classified by manual gating. The axes are in arbitrary units. (c) Biaxial plots represent the same data shown in b, and show the gates drawn manually by expert operators. The colors of the squares match the colors in b. The actual manual gating used here is more complex and uses a series of biaxial plots to gate each population. Note, that unlike in b, no single biaxial plot spatially separates all subsets. (d) The same viSNE map shown in b is colored according to intensity of CD11b expression. Many of the cells within the dotted line gate were not classified as monocytes by manual gating (gray cells, b). Figure and legend taken from (Amir et al., 2013).

1.6.3. Environments for cytometry data analysis

Various implementations of t-SNE exist. viSNE is the implementation developed in Dana Pe'ers' lab and distributed as a part of CYT, an interactive visualization tool based

on MATLAB that is free for academic use and contains a graphical user interface (Amir et al., 2013). Cytobank, an online platform for cytometry analysis, has viSNE as an integrated tool among other tools. t-SNE has also been directly implemented in various programming languages (R, Python, C++, Matlab) which are freely available for download. R is highly suited to cytometry data analysis and, within R Studio, has a graphical interface for visualizing plot outputs. Bioconductor (www.bioconductor.org) (Gentleman et al., 2004) is an open source repository that contains packages for R that deal with various aspects of cytometry data handling. Additionally, Github (www.github.com) contains software published by developers with instructions for implementation in R (or other languages).

1.6.4. Clustering – defining borders in the similarity landscape

Clustering algorithms directly assign cells to distinct clusters which can then be overlaid onto a t-SNE map or minimum spanning tree (or onto any other plots that visualize the cells). There are many different clustering algorithms which vary in the way that they calculate similarity between cells which can translate to efficiency at finding rare populations and in the duration of the runtime. For a comprehensive comparison, see (Saeys et al., 2016; Weber and Robinson, 2016).

1.6.4.1. SPADE

SPADE (Spanning-tree Progression Analysis of Density-normalized Events) (Qiu et al., 2011) was one of the first algorithms to be used in immunology publications. SPADE depicts cell populations in a branched tree structure and consists of connected nodes that represent clusters of cells, thereby also providing information about the relationship between cell types. SPADE includes a density-dependent down-sampling (ensuring inclusion of rare cell types with few similar neighbors) followed by hierarchical, agglomerative clustering (grouping cells into a user-defined number of clusters), construction of a minimum spanning tree (MST) with edges connecting the nodes, iterations to connect all nodes to the tree and lastly, for all cells in the initial dataset SPADE determines the closest neighbor in the down-sampled data and assigns the cell to the corresponding cluster. Since SPADE includes steps involving random decisions, it is of a nondeterministic nature. As a consequence, several runs of SPADE

will result in differently organized trees.

1.6.4.2. FlowSOM

In this thesis, we made use of the FlowSOM algorithm (flow cytometry data analysis using self- organizing maps) (Van Gassen et al., 2015) as it defines population clusters efficiently and with the fewest mismatches, and is computationally light and fast compared to other algorithms (Weber and Robinson, 2016). FlowSOM is based on the principle of self-organizing maps (SOMs) which is an unsupervised technique for clustering and dimensionality reduction (Kohonen, 1990). The workflow is outlined in Figure IX. After optional preprocessing steps, a SOM is built from the input data without sub-sampling. SOMs are a type of artificial neural network, consisting of a grid of 100 nodes, in which each node represents a point in the original multi-dimensional input space. New points are added and classified with the node that is the closest neighbor. The grid is trained in such a way that nearby nodes resemble each other more than nodes that are further away by repeatedly picking a point from the dataset, finding the node nearest to it and updating all the nodes in the neighborhood of that node. As the next step, the SOM is visualized as a MST (similar to SPADE). Lastly, a metaclustering step is performed, employing consensus hierarchical clustering where the number of metaclusters is determined by the user-defined *k*-value.

1.6.4.3. PhenoGraph

PhenoGraph (Levine et al., 2015) models the high-dimensional space using a k-NNG (k Nearest Neighbor Graph), in which each cell is depicted as a node that is connected to its neighbors by edges. In this graph, phenotypically similar clusters of cells will be represented as sets of highly interconnected nodes. These can be seen as "neighborhoods" or "communities" of cells, and can be partitioned in high-dimensional space using similar community-detection algorithms used for the analysis of social networks. While PhenoGraph performs well, its runtimes are up to 10 times longer than FlowSOM.

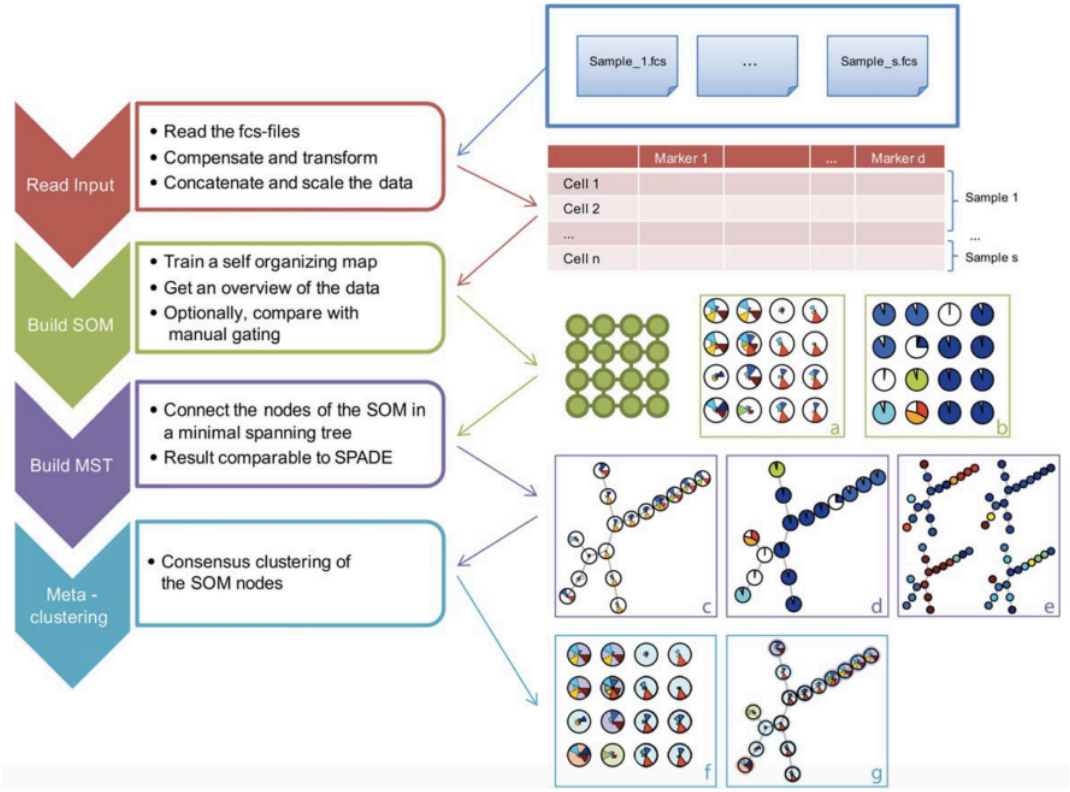

Figure IX. Overview of the four steps of the FlowSOM algorithm. (i) The fcs-files are read, optionally compensated, transformed, concatenated and scaled, resulting in a matrix with a row for every cell, describing the measured marker values. (ii) A self-organizing map is trained on the matrix. The result is a grid of nodes, corresponding to cell clusters. Visualizations can be made showing the mean marker values of each node in star charts (a) or the concordance with a manual gating in pie charts (b). (iii) A minimal spanning tree is built, on which the same information can be visualized (c,d). We can also show mean marker values for specifically chosen markers, resulting in figures very similar to SPADE trees (e). (iv) A meta-clustering of the nodes is calculated, corresponding to an automatic gating procedure. This is indicated by the background color of the nodes, and can be both visualized in the grid (f) or the minimal spanning tree (g). Figure and legend adapted from (Van Gassen et al. 2015).

1.6.4.4. X-shift

X-shift (Samusik et al., 2016) exists in a standalone Java application (VorteX clustering environment) with an easy-to-use graphical interface (the command-line version is also available). Very briefly, X-shift employs weighted k-NN density estimation, detection of local density maxima which form region centroids, connection of centroids via a graph, and cluster merging. The clusters can then be displayed on a variety of different visualizations within VorteX. Although X-shift runtimes are longer than FlowSOM runtimes, X-shift is the most successful algorithm to date at accurately finding rare populations (Weber and Robinson, 2016).

1.6.5. Force-directed graphs – measuring similarity and integrating data sets

While t-SNE groups cells based on their similarity in the high-dimensional space, the distances between cells are less accurate the more dissimilar they are and therefore not necessarily directly proportional to their similarity (Van Der Maaten and Hinton, 2008). To accurately show the hidden structure within the data, the similarity distances can be represented by edges that are controlled by a force-directed graph algorithm (Jacomy et al., 2014; Spitzer et al., 2015). While SPADE visualizes cell clusters in a MST with nodes that are also interconnected by edges, the MST used by SPADE is susceptible to overfitting the data and is not robust to local variation (Zunder et al., 2015b). Force-directed approaches are based on a set of "forces" that guide data organization. Nodes (in this case, groups of cells) that are similar are connected by edges with a length proportional to their similarity. These nodes are then spatialized into a graph: initially, all nodes repel one another as if they were the same poles of magnets, but edges pull similar nodes together, acting like springs.

Scaffold (single-cell analysis by fixed force- and landmark-directed) maps use force-directed graphs in combination with CLARA (clustering for large applications) clustering of the nodes (Spitzer et al., 2017; Spitzer et al., 2015). Scaffold also includes known manually gated populations as landmark nodes on the graph, around which unsupervised nodes are grouped, allowing for easier interpretation of the cell populations (Figure X). Landmark nodes are fixed in position to form a reference map. What makes Scaffold very useful is that it allows the mapping of independent datasets onto a reference map. For example, this can facilitate the integration of CyTOF and FACS data from different experiments, or the mapping of a systemic immune response in different organs compared to a reference map from the bone-marrow, for example. Furthermore, Statistical Scaffold (Spitzer et al., 2017) measures the changes between a reference map and an interrogated map and colors the nodes by statistical significance.

The VorteX application also includes a single-cell force-directed graph layout for visualizing X-shift clustered data which can also be used as a reference map, allowing direct comparison of datasets (Samusik et al., 2016). A comparison of a Scaffold and X-shift map are shown in Figure XI.

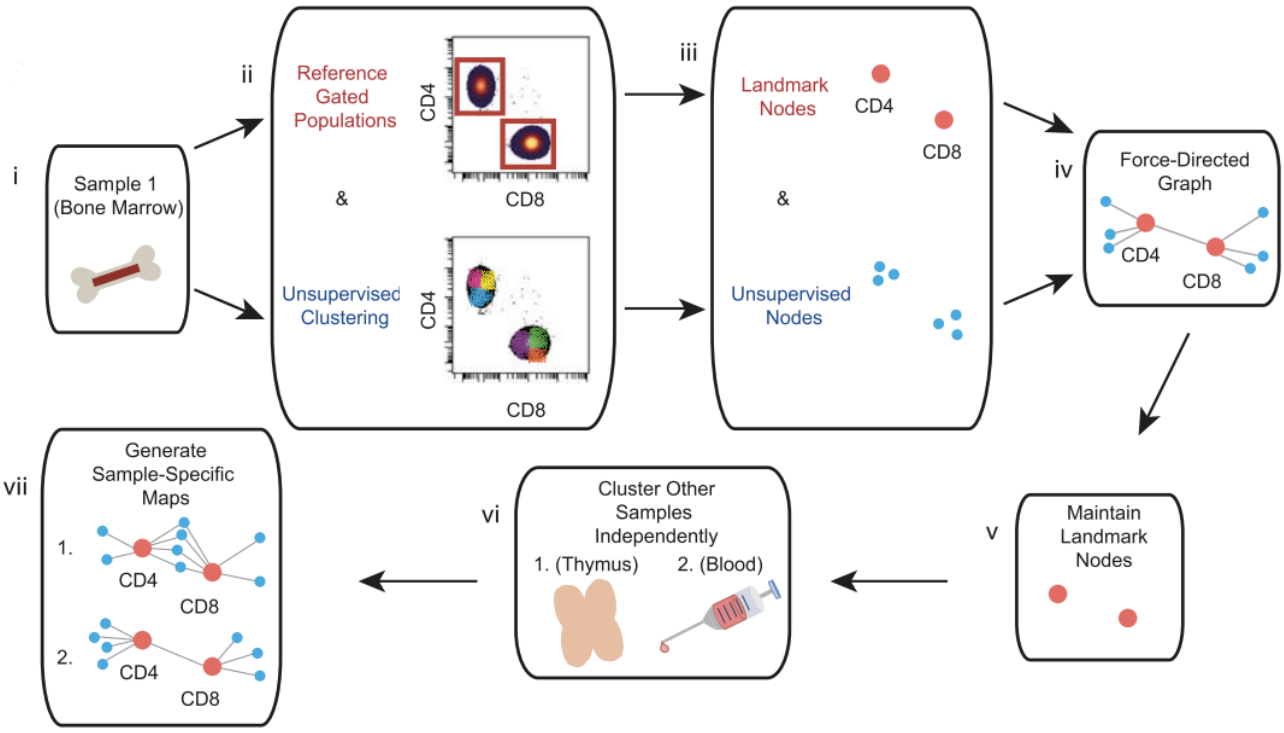

Figure X. Schematic of the Scaffold map algorithm. (i) Bone marrow from C57BL/6 mice was chosen as the reference sample. (ii) Leukocytes are grouped according to prior knowledge to define landmark cell populations as reference points on the map. The same leukocytes are subjected to unsupervised clustering with CLARA to provide an objective view of the tissue composition and organization. An example is provided using $CD4^+$ and $CD8^+$ T cells. (iii, iv) Both landmark populations (red nodes) and unsupervised clusters (blue nodes) are used to generate a force-directed graph in which similar nodes are located close together proportional to the similarity of their protein expression. Thus, similar nodes fall in proximity to one another while disparate nodes segregate apart from one another. Size of unsupervised clusters denotes the relative number of cells in that node. (v) Landmark populations from the bone marrow are fixed in place into a reference map for subsequent maps to provide points of reference for rapid human interpretation. (vi) Additional samples are each subjected to unsupervised clustering via the CLARA clustering algorithm. (vii) The resulting clusters for each sample were overlaid onto the original landmark nodes to generate tissue-specific Scaffold maps. Figure and legend adapted from (Spitzer et al., 2015).

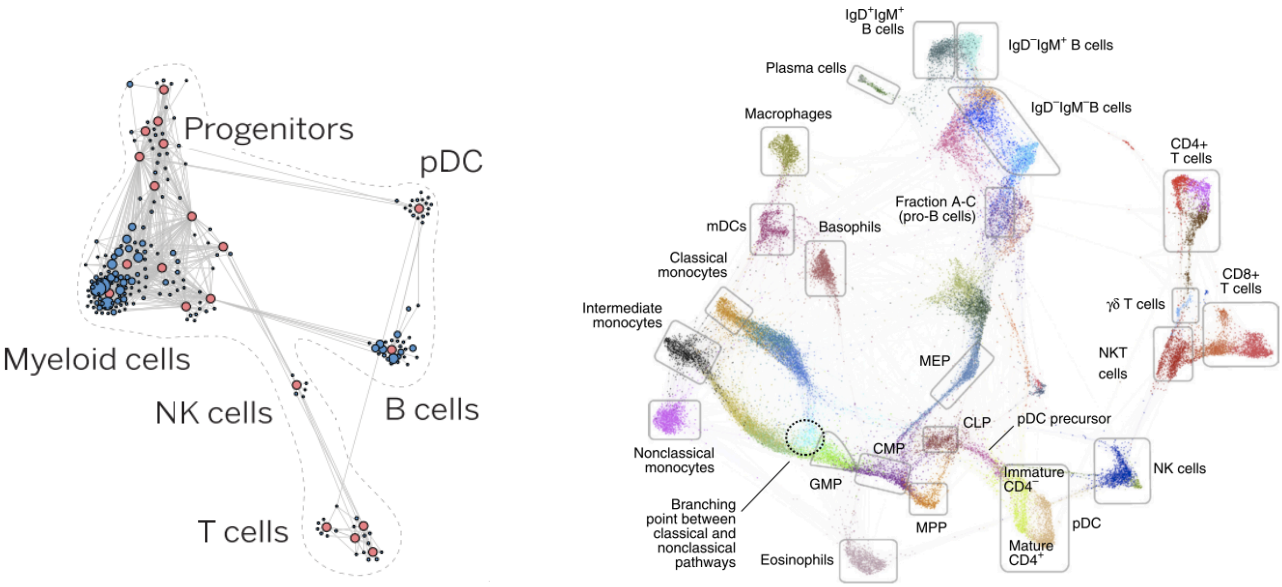

Figure XI. A comparison between force-directed graph layouts. (left) A Scaffold map of C57BL/6 bone marrow showing landmark nodes (red) and nodes clustered by CLARA (blue) (Spitzer et al., 2015). (right) A single-cell force-directed graph of showing C57BL/6 bone marrow overlaid cells clustered with X-shift (color coded for 48 clusters, k = 20) (Samusik et al., 2016). Panels used for staining the bone marrow differed.

1.6.6. Other algorithms for modeling immunology systems

One-SENSE (One-dimensional Soli-Expression by Nonlinear Stochastic Embedding) (Cheng et al., 2016), is a useful algorithm for displaying features of cells where measured parameters are grouped into predefined categories and each dimension (plot axis) has biological meaning that can be easily annotated with binned heat plots.

A developmental trajectory can be modeled using Wanderlust (Amir, 2014; Bendall et al., 2014), and a branching trajectory using Wishbone (Setty et al., 2016). However, Wanderlust assumes an unbranching trajectory and Wishbone assumes a bifurcating one. If the presence of a branch within a progressive dataset is unknown, TreeTop (Macnair et al., 2017) can be used to test this hypothesis.

The question following visualization and clustering of datasets usually involves finding the distinctive cell population that stratifies two sets of samples. Citrus provides an unsupervised and automated process that combines computational identification of cellular subpopulations with various association models to reveal stratifying clusters and cellular responses that are best predictive, or best correlated with the experimental

endpoint (Bruggner et al., 2014). CellCnn (Arvaniti and Claassen, 2017) performs a similar function to Citrus but is better suited to finding rare predictive cell types.
Finally, once cell populations of interest within high-dimensional data sets have been identified, further functional experiments to determine their role in a particular context may be desired. In order to be able to isolate a cell type, markers that can identify it in low dimensions and are therefore suitable for FACS sorting are necessary. Marker Enrichment Modeling (MEM) (Diggins et al., 2017) can be used to extract the most distinguishing markers within the panel as it describes cells by quantifying contextual feature enrichment and reporting a human- and machine-readable text label.

1.6.7. Practical considerations for automated data analysis

The first practical aspect when starting to analyze high-dimensional data sets in an automated manner is to perform appropriate quality control (QC) and data pre-processing.

1.6.7.1. Data normalization and compensation for spillover

While proper QC of both the instrument and acquired data should always be part of a standard cytometry analysis workflow, it becomes even more relevant with increasingly complex experiments. QC must include validation of the instrument used: and for fluorescence-based cytometry the assessment of signal stability over time as well as potential artifacts arising from improper compensation (reviewed in (Perfetto et al., 2006)), and for mass cytometry the inclusion of EQ Four Element Beads with the sample during acquisition allows to the subsequent normalization of the data for the inevitable signal drift over long periods of acquisition time (Finck et al., 2013). Currently, compensation is not widely used for mass cytometry data as the spillover from certain channels is minor. This spillover is caused mainly by isotopic impurities in the metals used to label the antibodies, metal oxide formation (in the Mass (M) + 16 channels) and mass cytometer properties (in the M ± 1 channels). However, recent attempts have begun to establish methods to correct for these artifacts (Chevrier et al., 2017a).

1.6.7.2. Data transformation

In addition to QC with respect to instrument and acquisition, automated analysis of high-dimensional data asks for dedicated pre-processing steps, especially data transformation. Epitope abundances measured by cytometry often follow normal distributions on a logarithmic scale (so called log-normal distribution) with the variance of different cell populations depending on their intensity. Therefore, obtaining a suitable representation of the data across its entire intensity range is crucial for visualization and particularly for automated analysis. To do so, different transformation methods can be employed (compared and reviewed in (Trotter, 2007) and (Finak et al., 2010)). In the context of the aforementioned algorithms, the data is frequently transformed using either an inverse hyperbolic (arcsinh) or logicle transformation (Herzenberg et al., 2006; Parks et al., 2006). This leads to a suitable representation of the data for values around zero, as well as for values on the upper end of the range. Functions to perform such data transformations are commonly integrated into the respective analysis tools (R packages, CYT via Matlab, Cytobank).

1.6.7.3. Percentile normalization

Another pre-processing step, which can be employed in order to improve automated data analysis, is per channel percentile normalization of the data which normalizes for the varying staining intensities of different markers and allows for a uniform range of expression values (from 0 to 1). This makes heatmaps and expression values overlaid on t-SNE maps more readable and comparable between markers.

2. Aims of the study – mapping the CNS immune atlas

The major aim of this study was to overcomes previous localization- and morphology-dependent limitations in distinguishing different CNS-resident and -infiltrating immune cells and compared their range of reactive states during CNS pathology. For this purpose, we established highly multiplexed panels of protein surface markers for mass and flow cytometry.

Our first aim was to fully characterize and map the steady state CNS immune landscape using mass cytometry and algorithm-guided data analysis. In order to be confident of our cell identification, we needed to validate our cell assignment. We aimed to do this through cell-specific response to different stimuli, the tracking of blood-derived leukocytes and labelling microglia and BAMs by genetic reporter and fate-map systems. We were particularly interested in new subsets of BAMs that we revealed through this analysis, and further aimed to localize them within specific compartments of the CNS by immunohistochemistry. Once our immune map of the steady state CNS was complete, our final aim was to interrogate the changes that occur during different forms of CNS pathology: aging and murine models of Alzheimer's disease (APP/PS1) and Multiple Sclerosis (EAE), highlighting the similarities and differences between them.

3. Results

3.1. CNS-Associated Immune Cell Populations in the Adult Steady State Mapped by Mass Cytometry

We employed an integrated set of strategies to enable comprehensive mapping of the immune cell populations within the murine CNS, as shown in Figure 1A. To capture the full complexity of cellular phenotypes we designed a 43-heavy metal isotope-tagged surface antibody panel for mass cytometry (Table S1). Mass cytometry data was further complemented by 22-color fluorescence cytometry and the location of specific cell populations within the CNS was analyzed by IHC.

We first interrogated the steady state CNS in 8-week-old C57BL/6 mice. To give an overview of all immune populations present, mass cytometry data was visualized in a t-SNE map and cells categorized by FlowSOM-guided clustering (Hartmann et al., 2016) (Figure 1B, C and Figure S1A). This approach revealed an unprecedented complexity of leukocytes within the normal CNS: microglia and other macrophage-like cells, several types of monocytes (Ly6C^{hi} and Ly6C^{low} monocytes, and MdCs), as well as classical DCs (cDCs), plasmacytoid DCs (pDCs), B cells (CD24^{+} and CD24^{-}, see Figure S1A), T cells, NK cells, NK T cells, innate lymphoid cells (ILCs), eosinophils and mast cells. Manual gating of the mass cytometry data confirmed the identity of these cell populations (Figure S1B). Microglia (CD45^{low}CD11b^{low}F4/80^{+}CD64^{+}MeTK^{+}Cx3CR1^{hi}Siglec-H^{+}CD88^{low}) were the most abundant immune cells in the steady state CNS (Figure 1D). Interestingly, we were able to identify a separate population of cells with a closely related protein expression pattern (CD45$^{low/+}$CD11b^{low}F4/80^{hi}CD64^{hi}MeTK^{+}Cx3CR1^{+}CD88^{hi}); however, these cells were lacked typical microglial Siglec-H expression, and instead expressed CD206 and CD38 (Figure 1C and S1A).

Using IHC, Goldmann and colleagues recently described a population of embryonically derived macrophages with a microglia-like phenotype, but occupying distinct locations, namely the border regions of the CNS in contrast to the parenchyma where only microglia reside (Goldmann et al., 2016). We hypothesized that the non-microglia macrophage-like cells identified in our unbiased analysis were in fact BAMs. These BAMs are virtually indistinguishable from microglia using conventional (CD45/CD11b) gating strategies (Figure S1B).

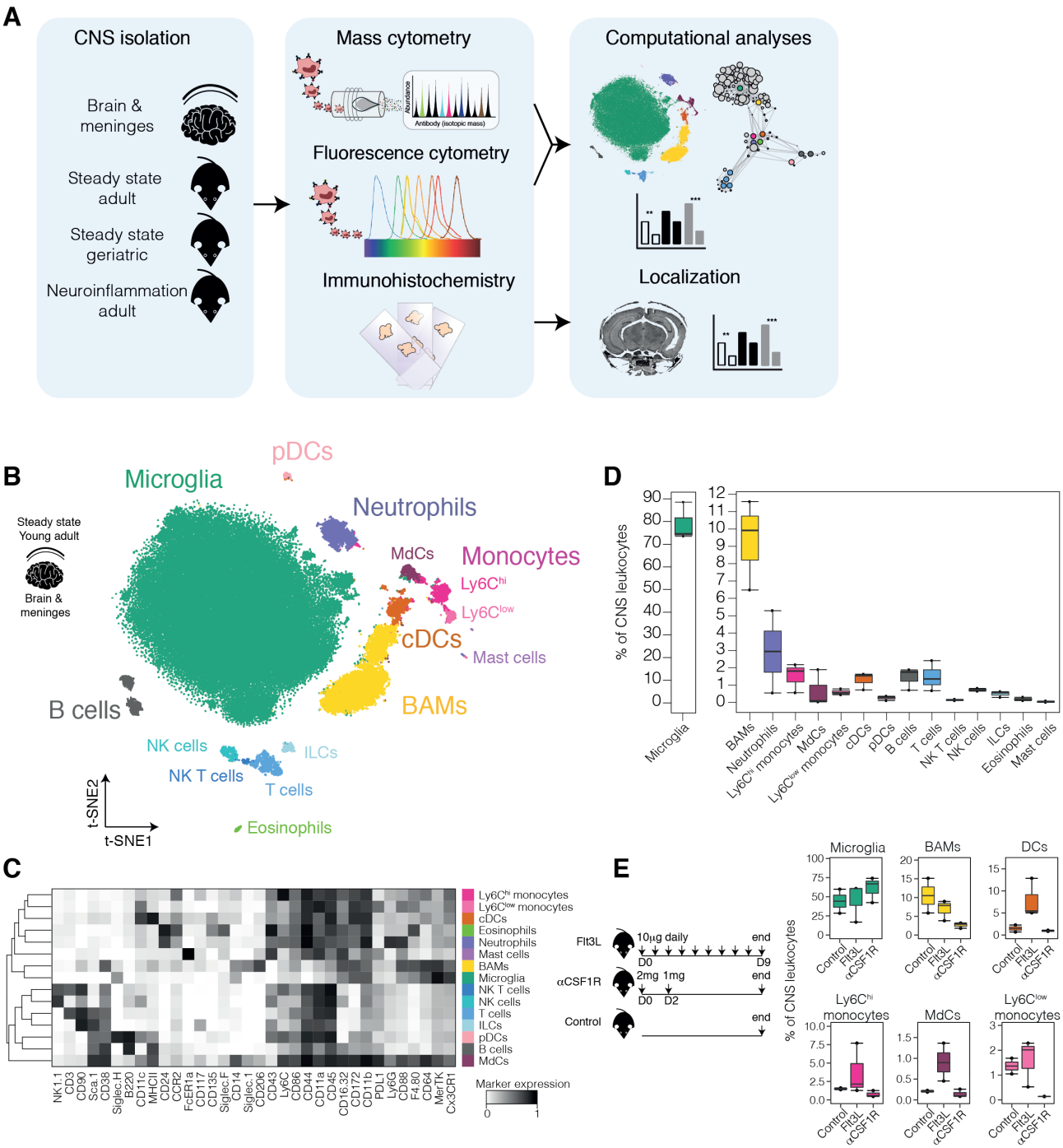

Figure 1. Identification of CNS-Associated Leukocytes in the Steady-State by Mass Cytometry. (A) Schematic representation of the experimental approach. (B) t-SNE map displaying 100,000 randomly sampled cells from the CNS of steady-state 2-month-old C57BL/6 mice analyzed by mass cytometry. Colors correspond to FlowSOM-guided clustering of cell populations (n = 3, representative of 6 independent experiments). (C) Median marker expression values for each population. (D) Frequencies of steady-state CNS leukocytes. (E) Experimental schematic (left) and frequencies (right) of myeloid populations within total CNS leukocytes after indicated treatments (n = 3). See also Figure S1, S2 and Table S1. Error bars represent range.

To confirm this and the identities of the other cell populations present, we first used functional assays that exploit characteristic cell type-restricted responses to different stimuli. We treated mice with either an anti-CSF1R antibody to deplete tissue-resident macrophages and Ly6C^{low} monocytes, but not microglia (which are likely protected by the BBB) or Ly6C^{hi} monocytes (Hoeffel et al., 2015), or with the growth factor Flt3L, which specifically expands DCs (Maraskovsky et al., 1996) (Anandasabapathy et al., 2011). Indeed, anti-CSF1R treatment depleted the cells we identified as BAMs and Ly6C^{low} monocytes, but had no effect on other cell types (Figure 1E). The depletion of BAMs further confirms their location within the border regions of the CNS where the vasculature has different barrier properties to the BBB of the parenchymal vasculature (Engelhardt et al., 2017). Flt3L treatment in turn increased the frequency of DCs, as well as Ly6C^{hi} monocytes and MdCs (after 9 days of treatment the bone-marrow monocyte progenitors are also targeted), while having no effect on microglial, BAM, or Ly6C^{low} monocyte populations (Figure 1E), thus functionally confirming our algorithm-guided population identification.

To determine whether the leukocytes we detected in the CNS were within the tissue itself or within the lumen of vessels or capillaries, we intra-venously injected fluorescently (PE)-labeled anti-CD45 antibodies (Anderson et al., 2014). Over 98% of control blood leukocytes were labeled with anti-CD45-PE, while only 5% of CNS leukocytes were labeled (Figure S2A-C); thus 95% of all CNS leukocytes identified are *bona fide* extra-vascular CNS-resident cells. Neutrophils constituted the third largest leukocyte population in the CNS, 81.8 ± 3.0% being unlabeled and therefore tissue-resident (Figure S2D and E). Tissue sections revealed neutrophils predominantly within the dura mater (Figure S2F), as well as the pia mater and the ependyma (data not shown) of the steady state CNS. Together, our analysis of the steady state CNS reveals multiple immune cell populations residing within CNS compartments, including a subset of microglia-like BAMs.

3.2. BAMs are CNS-Resident Macrophages Distinct from Microglia

We used our mass cytometry data to design a 22-color antibody panel for fluorescence cytometry (Table S1) which identified all the major leukocytes in the CNS. This allowed us to use genetic reporter and fate-mapping experiments aimed at determining

the relationship between BAMs, microglia and CNS DCs. To compare the mass- and fluorescence cytometry datasets and their ability to identify the same cell populations, we employed force-directed analysis to generate a Scaffold map (Spitzer et al., 2015): we first modeled a reference map of CNS leukocytes from our mass cytometry data, using manually gated populations as landmark nodes (in colors), and the initial 100 FlowSOM nodes (before metaclustering) as unsupervised nodes (in gray) (Figure 2A). Mapping the flow cytometry data onto this mass cytometry-based reference map showed that cells within unsupervised nodes that grouped around the landmark nodes had the expected expression profiles and were present at similar frequencies to those in the original reference map (Figure 2B and 2C).

We then examined cells from the CNS of *Sall-1*^{GFP} reporter mice (Buttgereit et al., 2016). Only microglia from these mice expressed the GFP reporter, and not BAMs or cDCs (Figure 2D and 2E and as a clustered t-SNE in S3A). Thus, in addition to the phenotypic distinctions between BAMs and microglia revealed by mass-cytometry, we confirmed Sall1 as a key transcription factor, which can be used to distinguish these closely-related cell populations.

Microglia and the majority of BAMs are long-lived (Goldmann et al., 2016) while DCs are bone-marrow derived and short-lived (Merad and Manz, 2009). To assess the longevity of our identified populations, we used *Cx3cr1*^{CreER} *Rosa26*-RFP inducible fate-map mice where tamoxifen induces irreversible expression of red fluorescent protein (RFP) in CX3CR1^{+} cells (Yona et al., 2013). Short-lived labeled cells will be replaced from unlabeled bone marrow progenitors, while long-lived or self-renewing cells will remain RFP^{+}. Here, 5 weeks after tamoxifen treatment of adult *Cx3cr1*^{CreER} *Rosa26*-RFP mice, less than 5% of monocytes were RFP^{+}, as expected (Figure S3B), while almost 80% of microglia, 50% of BAMs, and less than 10% of DCs were RFP^{+} (Figure 2F and 2G). Most BAMs retain the RFP label, as a result of the earlier tamoxifen treatment, whereas most DCs lose RFP expression. Hence, we conclude that CX3CR1^{+} BAMs are replaced more slowly than CX3CR1^{+} DCs. This differential longevity confirms that the high-dimensional map produced here corresponds to the predicted ontogeny of CNS leukocytes.

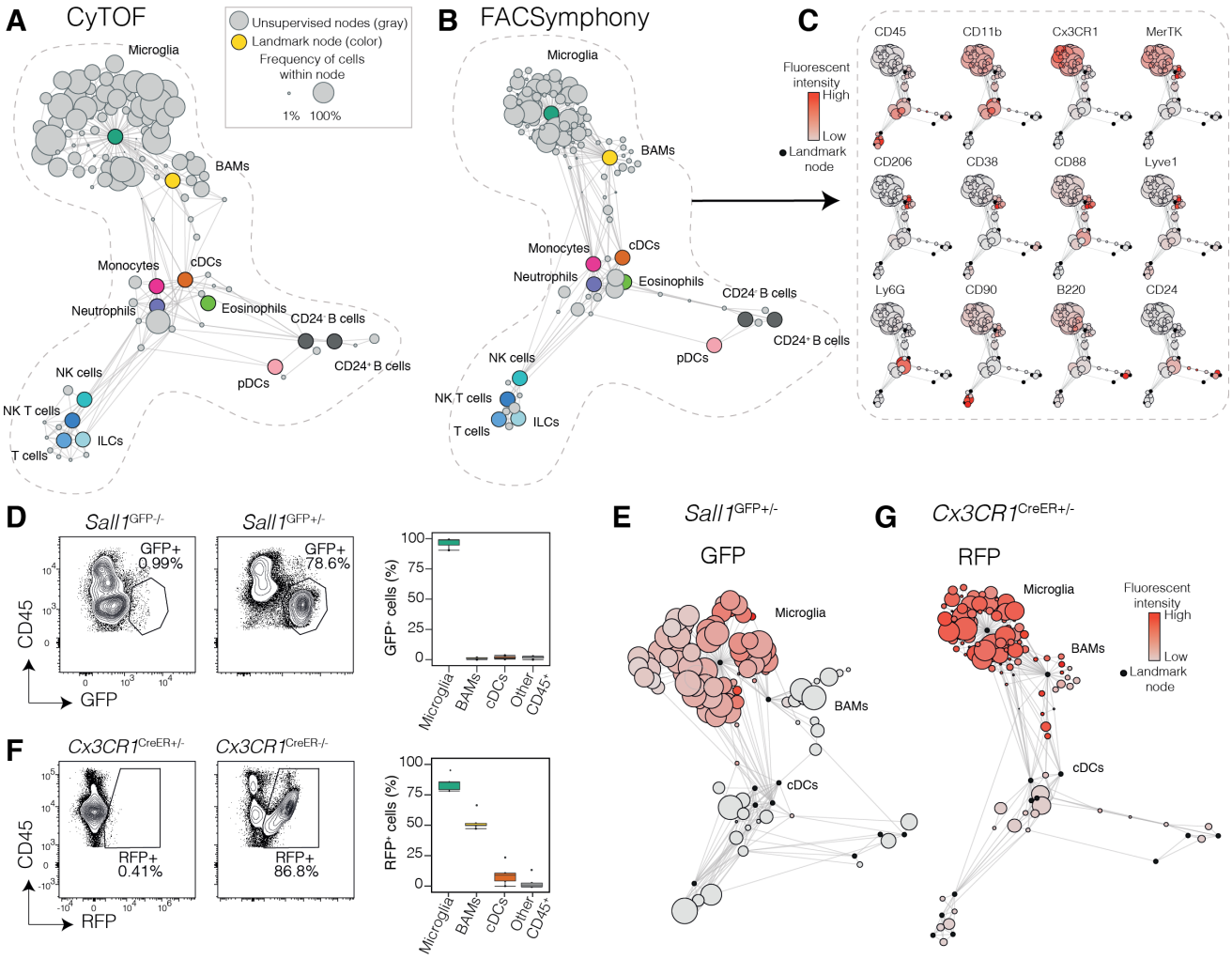

Figure 2. Identification of Microglia and BAMs by Genetic Targeting. (A) A Scaffold reference map of the steady-state adult CNS leukocyte landscape constructed from mass cytometry data displaying 100 unsupervised FlowSOM nodes and manually-gated landmark nodes. (B) Fluorescence cytometry data of steady-state adult CNS leukocytes mapped onto the reference map created in (A). (C) Representative fluorescent marker expression in the Scaffold map. (D) CD45$^+$ CNS leukocytes (left) and frequency of GFP$^+$ cells (right) in *Sall1*$^{GFP+/-}$ reporter mice (n = 3, representative of two independent experiments). (E) GFP expression overlaid onto the *Sall1*$^{GFP+/-}$ Scaffold map. (F) CD45$^+$ CNS leukocytes (left) and frequency of RFP$^+$ cells (right) in *Cx3cr1*^{CreER} *Rosa26*-RFP mice 5 weeks after tamoxifen treatment. (n = 5, showing 4 pooled experiments). (G) RFP expression overlaid onto the *Cx3cr1*^{CreER} *Rosa26*-RFP Scaffold map. See also Figure S3. Error bars represent range.

3.3. Enrichment of BAM Subsets in Distinct CNS Compartments

Now that we could reliably discriminate BAMs from microglia and DCs we conducted an in-depth BAM phenotype analysis. This revealed expression of the macrophage-associated markers MerTK, CD64 and F4/80, as well as CD16/32 (Figure 3A), and absence of the DC, monocyte and microglia markers CD11c, Ly6C

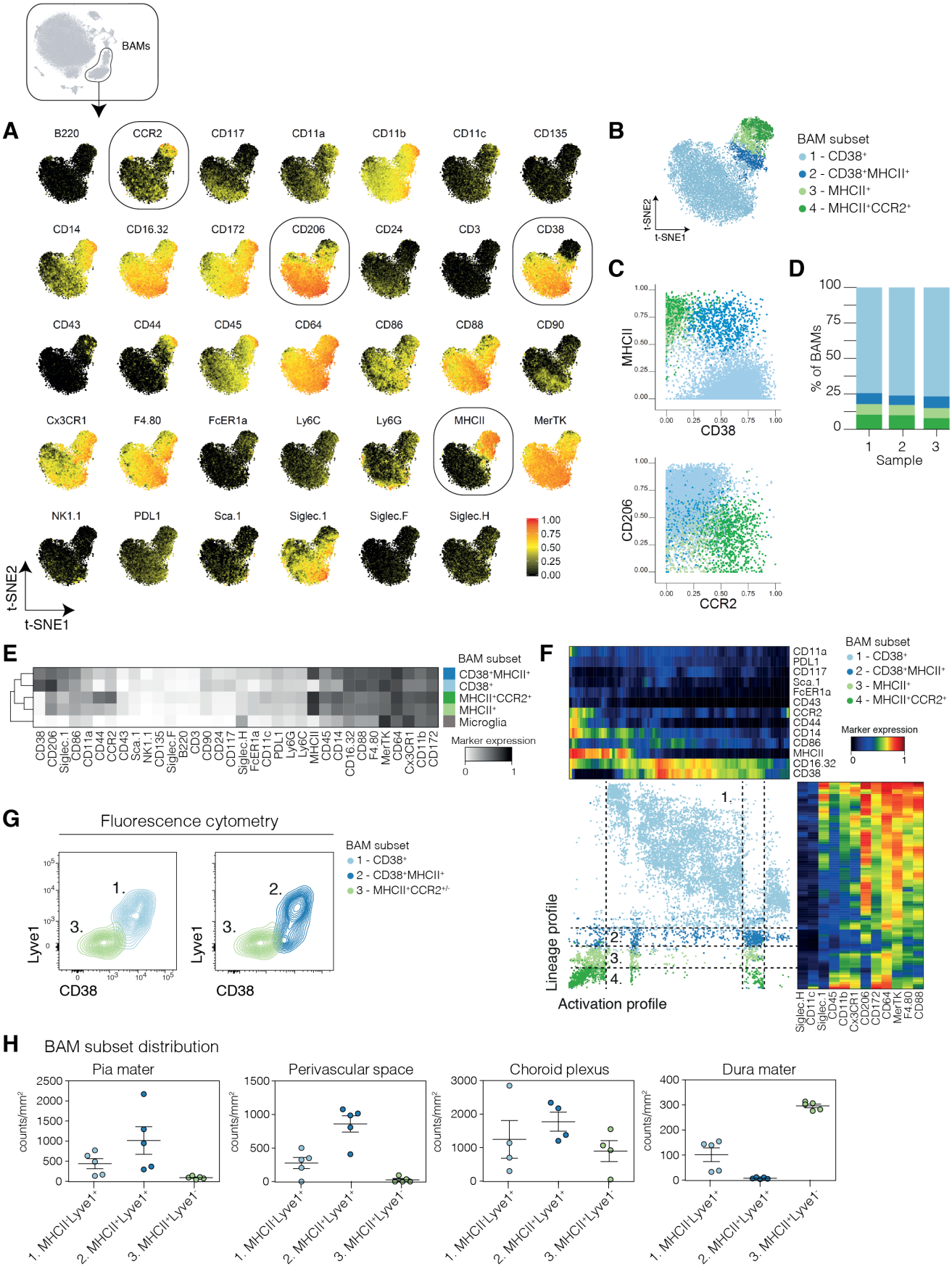
BAMs
A
B220
CCR2
CD117
CD11a
CD11b
CD11c
CD135
CD14
CD16.32
CD172
CD206
CD24
CD3
CD38
CD43
CD44
CD45
CD64
CD86
CD88
CD90
Cx3CR1
F4.80
FcER1a
Ly6C
Ly6G
MHCII
MerTK
NK1.1
PDL1
Sca.1
Siglec.1
Siglec.F
Siglec.H
1.00
0.75
0.50
0.25
0.00
t-SNE2
t-SNE1
B
BAM subset
1 - CD38+
2 - CD38+MHCII+
3 - MHCII+
4 - MHCII+CCR2+
C
MHCII
CD38
CD206
CCR2
D
% of BAMs
Sample
E
BAM subset
CD38+MHCII+
CD38+
MHCII+CCR2+
MHCII+
Microglia
Marker expression
F
BAM subset
Marker expression
Lineage profile
Activation profile
G
Fluorescence cytometry
Lyve1
CD38
H
BAM subset distribution
Pia mater
Perivascular space
Choroid plexus
Dura mater
counts/mm2
1. MHCII-Lyve1+
2. MHCII+Lyve1+
3. MHCII+Lyve1-

Figure 3. In-depth Characterization of the Phenotype and Localization of CNS BAMs.
(A) CNS BAMs were plotted onto a separate t-SNE. Outlined plots represent four distinguishing markers of BAM subsets. (B) BAMs clustered into four subsets based on the entire panel of markers. (C) Expression of CD38, MHCII, CCR2 and CD206 by the four BAM subsets (colored). (D) Relative frequencies of the four BAM subsets across 3 mice (n = 3, representative of 4 independent experiments). (E) Median expression of mass cytometry markers on each BAM subset and microglia. (F) One-SENSE analysis of BAMs along lineage and activation profiles. (G) Fluorescence cytometry data depicting expression of Lyve1, CD38 and MHCII in three BAM subsets. (H) Density of BAM subset occurrence within each region of interest (ROI) (n ≥ 5 mice, ROI ≥ 4 per mouse). See also Figure S4. Error bars represent the median ± SEM.

and Siglec-H, respectively. We identified four BAM subsets based on differential expression of CD38, MHCII and CCR2: subset 1 ($CD38^{+}MHCII^{-}CCR2^{-}$), subset 2 ($CD38^{+}MHCII^{+}CCR2^{-}$), subset 3 ($CD38^{-}MHCII^{+}CCR2^{-}$), and subset 4 ($CD38^{-}MHCII^{+}CCR2^{+}$) (Figure 3B and 3C). The median expression values of each marker in the different BAM subsets are compared in a heatmap (Figure 3D). The majority of BAMs (75.7 ± 1.2%) were located within subset 1, while subsets 2, 3 and 4 comprised 7.6 ± 0.8%, 7.2 ± 0.2% and 9.4 ± 1.2% of total BAMs, respectively (Figure 3E). Clusters 3 and 4 are very similar and because they essentially differ only in the amount of CCR2 expression. To understand the full heterogeneity and distinct high-dimensional phenotypes of the four BAM subsets at the single-cell level, we employed categorical One-SENSE analysis (Cheng et al., 2016), where the *y*-axis represents the lineage profile, the *x*-axis represents an activation marker profile (Figure 3F), and co-regulation of marker expression is also shown, e.g. CD206 expression is high on subset 1 but decreases as the activation markers MHCII and CD44 increase towards subsets 2, 3 and 4 while high expression of other macrophage markers like CD64 are maintained. We then used confocal microscopy to ask whether these subsets are enriched in specific compartments of the CNS. The available anti-mouse CD38 performs poorly in IHC, however using fluorescence cytometry we found that Lyve-1 and CD38 expression closely overlap (Figure 3G and S4A) and therefore that Lyve-1 was a suitable surrogate for CD38 on BAMs. Since lymphatic vessels also express Lyve-1 and are present in the dura mater (Louveau et al., 2015), we also stained for collagen IV, which is expressed on vessels but not BAMs. Combining Lyve1 or MHCII with the macrophage marker Iba-1, we located BAMs within the pia mater, perivascular space, choroid plexus and dura mater and showed that they express CD206, as previously shown (Figure S4B). By histology, we identified three BAM subsets in these regions using differential Lyve1

and MHCII expression (Figure S4C). The initial CyTOF-identified subsets 3 and 4 are merged here. Of note, Lyve-1^{+}MHCII^{+} (subset 2) BAMs were enriched in the pia mater and perivascular space, whereas the dura mater harbored relatively more single-positive MHCII^{+} BAMs (subsets 3 and 4) and few Lyve-1^{+}MHCII^{+} BAMs (Figure 3H). The choroid plexus contained a similar frequency of each of the three BAM subsets. Single-positive Lyve1^{+} BAMs (subset 1) were present in all locations. Interestingly, only MHCII^{+} BAMs, enriched in the choroid plexus and dura mater, expressed CCR2^{+} (Figure 3B) (subset 4), consistent with their proposed high turnover rate from CCR2^{+} bone marrow cells (Goldmann et al., 2016). These phenotypic variations of BAMs across the CNS may reflect functional differences and could be shaped by cues from their specific local microenvironments.

3.4. Heterogeneous Subsets of DCs Exist in the CNS

Besides BAMs, DCs also localize in the CNS border regions and are considered to be the prime APCs at these sites (Anandasabapathy et al., 2011; Greter et al., 2005). In other tissues, DCs exist as functionally and phenotypically distinct subsets but little is known of the DCs associated with the CNS. We used our mass cytometry data to perform an in-depth phenotypic characterization of CNS-associated DCs (Figure 4A). We identified three main DC subsets corresponding to cDC1s, cDC2s and pDCs (Figure 4B), differentiated by their expression of CD11b (or CD172) and CD24 (Figure 4C). In addition, Ly6C, B220 or Siglec-H confirmed the pDC identity of subset 6. The cDC2 population was heterogeneous and could be further separated into CD24^{+}CD206^{+} cDC2 (subset 1), CD24^{-}CD64$^{+/low}$CD206$^{-/low}$ cDC2 (subset 2), CD135^{hi} cDC2 (subset 3) and PDL1^{+} cDC2 (subset 4); while cDC1s (subset 5) were CD11b^{low}CD172^{low}CD24^{+}CD135^{hi}CD117^{+} (Figure 4D). As in most other organs (Guilliams et al., 2016), cDC2s were relatively more abundant than cDC1s (Figure 4E). The lineage markers and activation profiles of these subsets were again fully revealed using categorical One-SENE (Figure 4F). We localized CD11c^{+}MHCII^{+} DCs of the CNS by confocal microscopy only in the choroid plexus, pia mater and dura mater, and not in the perivascular space (Figure 4G), suggesting that these DC-enriched compartments may serve as entry sites for MHC-dependent T cells.

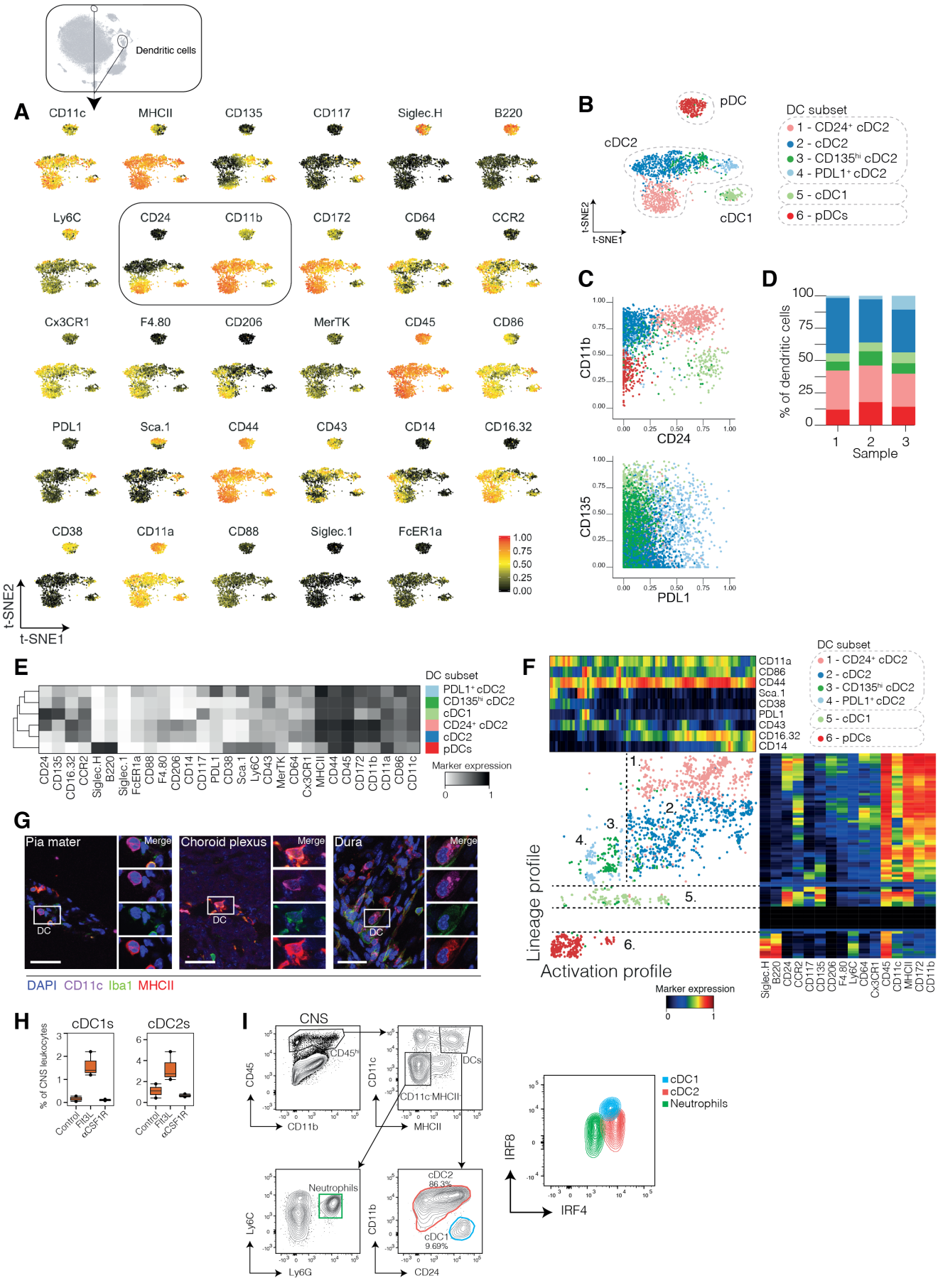
Dendritic cells
A
CD11c
MHCII
CD135
CD117
Siglec.H
B220
Ly6C
CD24
CD11b
CD172
CD64
CCR2
Cx3CR1
F4.80
CD206
MerTK
CD45
CD86
PDL1
Sca.1
CD44
CD43
CD14
CD16.32
CD38
CD11a
CD88
Siglec.1
FcER1a
1.00
0.75
0.50
0.25
0.00
t-SNE2
t-SNE1
B
pDC
cDC2
cDC1
t-SNE2
t-SNE1
DC subset
1 - CD24+ cDC2
2 - cDC2
3 - CD135hi cDC2
4 - PDL1+ cDC2
5 - cDC1
6 - pDCs
C
CD11b
CD24
CD135
PDL1
D
% of dendritic cells
Sample
E
DC subset
PDL1+ cDC2
CD135hi cDC2
cDC1
CD24+ cDC2
cDC2
pDCs
Marker expression
CD24
CD135
CD16.32
CCR2
Siglec.H
B220
Siglec.1
FcER1a
CD88
F4.80
CD206
CD14
CD117
PDL1
CD38
Sca.1
Ly6C
CD43
MerTK
CD64
Cx3CR1
MHCII
CD44
CD45
CD172
CD11b
CD11a
CD86
CD11c
F
CD11a
CD86
CD44
Sca.1
CD38
PDL1
CD43
CD16.32
CD14
DC subset
1 - CD24+ cDC2
2 - cDC2
3 - CD135hi cDC2
4 - PDL1+ cDC2
5 - cDC1
6 - pDCs
1.
2.
3.
4.
5.
6.
Lineage profile
Activation profile
Marker expression
Siglec.H
B220
CD24
CCR2
CD117
CD135
CD206
F4.80
Ly6C
CD64
Cx3CR1
CD45
CD11c
MHCII
CD172
CD11b
G
Pia mater
Choroid plexus
Dura
Merge
DC
DAPI CD11c Iba1 MHCII
H
cDC1s
cDC2s
% of CNS leukocytes
Control
Flt3L
αCSF1R
I
CNS
CD45hi
CD45
CD11b
CD11c
MHCII
DCs
CD11c+MHCII-
Neutrophils
cDC2
86.3%
cDC1
9.69%
Ly6C
Ly6G
CD11b
CD24
IRF8
IRF4
cDC1
cDC2
Neutrophils

Figure 4. Dendritic Cell Heterogeneity in the Steady-State CNS. (A) CNS DCs were plotted onto a separate t-SNE. Selected plots represent four chosen distinguishing markers. (B) DCs clustered into three major subsets based on the entire panel of markers. (C) Expression of distinguishing markers by the DC subsets. (D) Relative abundance of the DC subsets within total CNS DCs across 3 mice (n = 3, representative of at least 3 experiments). (E) Median expression of mass cytometry panel markers on each DC subset. (F) One-SENSE analysis of DCs by their lineage and activation profiles. (G) Representative fluorescence immunohistochemistry images of DCs in the pia mater, choroid plexus and dura mater ($n \geq 2$ mice, ≥ 3 sections per mouse). (H) cDC1 and cDC2 response to the indicated stimuli. (I) IRF4 and IRF8 expression by cDC1s and cDC2s.

Since we have shown that CNS cDC2s exist with some heterogeneity in their surface phenotype, we sought to confirm their inherent identity compared to cDC1s. Both cDC2s and cDC1s expanded to a similar extent with Flt3L treatment (Figure 4H) and moreover cDC1s were IRF8^{hi}IRF4^{int} and cDC2s were IRF8^{-}IRF4^{hi} (Figure 4I), as previously predicted (Guilliams et al., 2016). The apparent heterogeneity of cDC2s has also been noted at other organs such as the lung (Schlitzer et al., 2013a) and heart (Clemente-Casares et al., 2017).

3.5. Aging and AD Change the CNS Myeloid Cell Landscape

Aging has profound effects on the entire CNS landscape. We therefore asked how the immune cell populations in the CNS changed in aged mice by comparing geriatric mice aged 1.5 years with younger adult mice aged 2 months. We first noted a dramatic increase in the frequency of T cells from 1.5 ± 0.9% in adult mice to 11.1 ± 4.2% in geriatric mice, while NK T cells and pDCs were significantly less frequent in geriatric mice (Figures 5A and 5B). We also observed an increased frequency of CD38^{+}MHCII^{+}CCR2^{-} and CD38^{-}MHCII^{+}CCR2^{-} BAMs and a corresponding decrease in CD38^{+}MHCII^{-}CCR2^{-} and CD38^{-}MHCII^{+}CCR2^{+} BAMs in geriatric mice (Figure 5C); alongside, the frequency of CD24^{+} cDC2s decreased, while CD135^{+} cDC2s were more abundant in geriatric mice (Figure 5D).

Strikingly, we found a phenotypic signature in a subset of microglia in geriatric mice which expressed high levels of CD11c and CD14 (Figure 5E). Aging is a major risk factor for neurodegenerative diseases, and changes in microglial morphology precede pathology in Alzheimer's patients (Perry and Holmes, 2014; Streit et al., 2009). We

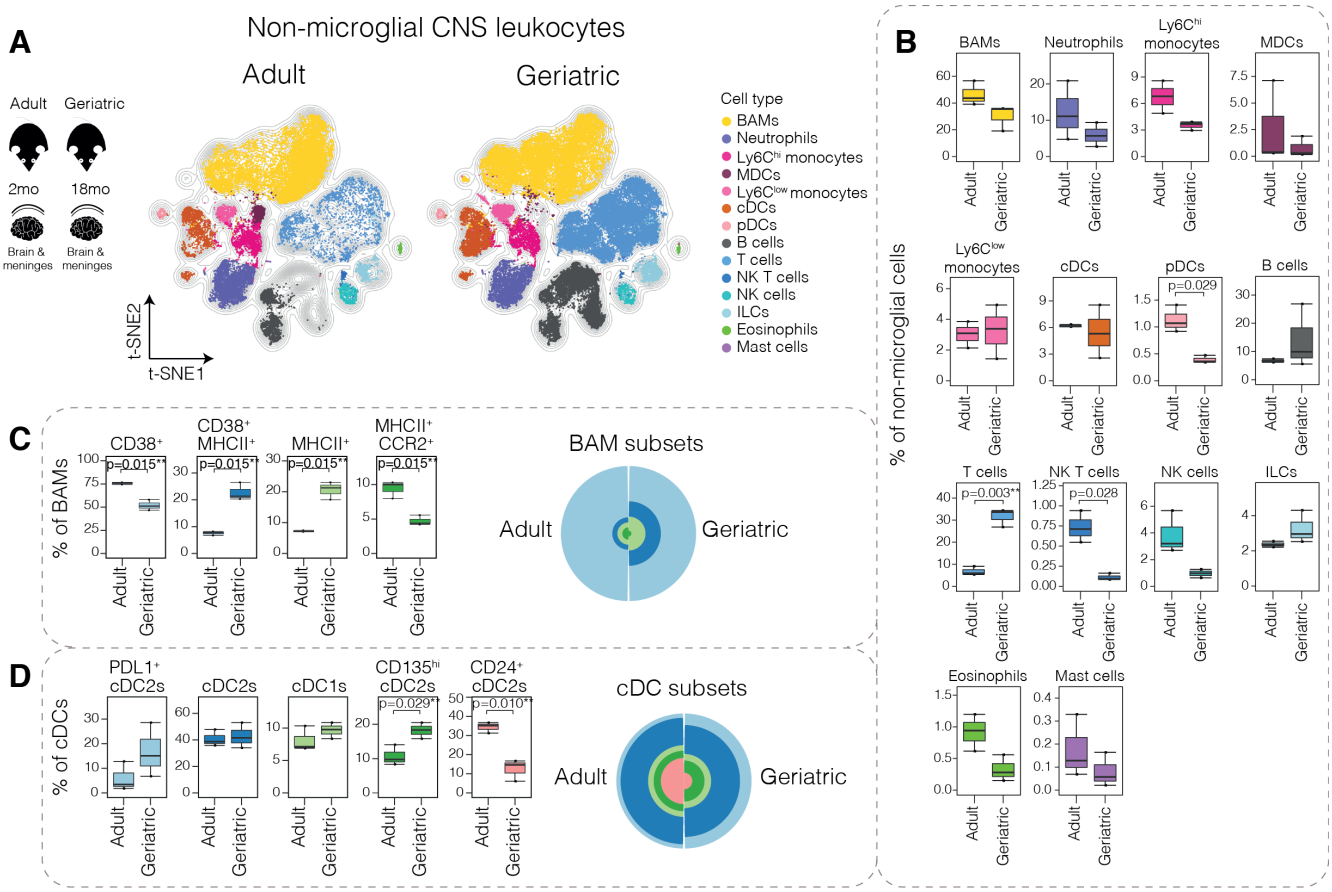
A
Non-microglial CNS leukocytes
Adult
Geriatric
2mo
18mo
Brain & meninges
Brain & meninges
t-SNE2
t-SNE1
Cell type
BAMs
Neutrophils
Ly6C^hi monocytes
MDCs
Ly6C^low monocytes
cDCs
pDCs
B cells
T cells
NK T cells
NK cells
ILCs
Eosinophils
Mast cells
B
% of non-microglial cells
BAMs
Neutrophils
Ly6C^hi monocytes
MDCs
Ly6C^low monocytes
cDCs
pDCs
p=0.029
B cells
T cells
p=0.003**
NK T cells
p=0.028
NK cells
ILCs
Eosinophils
Mast cells
Adult
Geriatric
C
% of BAMs
CD38+
CD38+ MHCII+
MHCII+
MHCII+ CCR2+
p=0.015**
BAM subsets
Adult
Geriatric
D
% of cDCs
PDL1+ cDC2s
cDC2s
cDC1s
CD135hi cDC2s
CD24+ cDC2s
p=0.029**
p=0.010**
cDC subsets
Adult
Geriatric
E
Microglia
Adult
Geriatric
2mo
18mo
t-SNE2
t-SNE1
CD14
CD11c
F
Microglia
WT
APP/PS1
4mo
4mo
Normal microglia
Age/AD associated microglia
G
% of all microglia
Adult
Geriatric
Whole brain
WT
APP/PS1
WT
APP/PS1
Cortex
Cerebellum
H
corrected p-value < 0.05
n.s.
Normal microglia
Age associated microglia
Median expression
CD14
CD86
PDL1
Siglec.H
CD11c
Siglec.1
CD44
CD88
CD90
CD11b
CD16.32
CD45
MHCII
CD206
Cx3CR1
CD117
F4.80
MerTK
CD64
CD11a
CD172
FcER1a
CD24
CD38
CD135
CCR2
Sca.1
CD43

Figure 5. Aging Alters the CNS Immune Landscape. (A) Non-microglial CNS leukocytes from adult (2-month-old) and geriatric (1.5-year-old) C57BL/6 mice analyzed by mass cytometry. Frequencies of (B) non-microglial CNS leukocytes, (C) BAM and (D) cDC subset distributions in adult and geriatric mice. (E) Normal and reactive microglia differentiated by CD14 and CD11c expression in adult and geriatric mice (n = 3). (F) Normal and reactive microglia in 4-month-old WT and APP/PS1 mice (n = 2-4, experiment repeated twice). (G) Frequencies of age- or AD-associated microglia in adult vs. geriatric C57BL/6 mice, or the cortex (plaque-harboring) and cerebellum (internal control) of WT vs. APP/PS1 mice, respectively. (H) Median expression of myeloid markers in the mass cytometry panel between normal and age-associated microglia in C57BL/6 adult and geriatric mice (corrected p-value < 0.5 if significant). ** = p-value significant with a Benjamini-Hochberg (BH) false discovery rate (FDR) < 5%. Error bars represent range except in (H) where error bars represent the median ± SEM. n.s. = not significant. See also Figure S5.

therefore asked whether the age-related changes in leukocyte populations and the age-associated microglial phenotype in particular were present in a murine model of Alzheimer's disease. We compared the plaque-harboring cortex with the non-plaque-harboring cerebellum (internal control) of 4-month-old APP/PS1 mice (Radde et al., 2006a; Vom Berg et al., 2012), and age-matched WT littermates (external control). We found that, as in much older geriatric mice, the frequency of T cells was increased in the plaque-harboring cortex of AD-prone mice (Figure S3A); while, in contrast to geriatric mice, the subset distribution of BAMs was unaltered in AD-prone mice (Figure S3B), suggesting it to be a phenomenon observed during normal aging.

Of note, we also detected a phenotypic signature in a subset of microglia in AD-prone mice that resembled microglia in geriatric mice in the expression of CD11c and CD14, and which was absent in WT littermate controls (Figure 5F). Approximately 11.9 ± 6.5% of microglia had this signature in geriatric mice, compared to virtually zero in young adult mice, and approximately 13.2 ± 1.7% in the plaque-bearing cortex of AD-prone mice, while these cells were almost undetectable in the unaffected cerebellum and in WT littermate cortex or cerebellum (Figure 5G and S3C). A similar subset of microglia was also found by Keren-Shaul and colleagues by sc-RNAseq in 5XFAD mice (Keren-Shaul et al., 2017). We located these $CD11c^+$ microglia around Aβ plaques in APP/PS1 mice (Figure S3D). The full reactive signature of these microglia shows that, in addition to increased phagocytosis-associated markers CD11c and CD14, there was an accompanying increase in activation markers CD86 and CD44 and the inhibitory ligand PDL1 (Figure 5H). MHCII expression increased slightly while expression of microglial inhibitory-checkpoint markers CX3CR1, MerTK and Siglec-

H decreased. This phenotypic change within the small age- and AD-associated subset represents a switch from a homeostatic microglial program to a 'reactive' signature that displays an activated, phagocytic profile (Hanisch and Kettenmann, 2007; Krasemann et al., 2017).

3.6. CNS Invasion and Resident Myeloid Cell Activation During Autoimmune Neuroinflammation

We induced EAE in adult C57BL/6 mice and compared the cellular composition of the CNS at the peak of disease with steady state control mice (Figure 6A and Figure S6A). Analyzing the frequencies (Figure 6B and S6C) and cell numbers (Figure S6C) of CNS leukocytes, we found that the majority of infiltrating cells were MdCs, closely followed by T cells.

Microglia were highly reactive during EAE and exhibited a markedly different phenotypic signature than in the steady state, as evidenced by their change in localization on the t-SNE map (Figure 6A). The microglial identity of these highly reactive cells during EAE was confirmed in *Sall1*^{GFP} reporter mice (Figure 6C and Figure S6D). We then conducted an in-depth analysis of the phenotypic changes in microglia in response to EAE inflammation: once again expression of microglial inhibitory-checkpoint markers CX3CR1, MerTK and Siglec-H was reduced, and expression of markers CD44, CD86, PDL1 and CD11c increased, as similarly observed in geriatric mice. However, in contrast to age- and AD-associated microglia, CD14 expression decreased during EAE and a dramatic increase in MHCII and Sca-1 was observed (Figure 6D, 6E and S6E). The conversion from the homeostatic microglial signature to the highly reactive state signature was also evident when comparing lineage and activation profiles using categorical One-SENSE (Figure 6F). Here and in the t-SNE map (Figure 6A and S6E) there are very few EAE microglia that are located in the same area as steady-state microglia. With a dramatic shift in both the lineage and activation profiles, and in contrast to a small subset of reactive microglia in aging and neurodegenerative disease, the entire microglial population becomes homogeneously reactive during EAE.

BAMs, MdCs, and DCs share a number of lineage markers. Interrogating their profiles more closely we found MdCs, monocytes and cDCs to be more similar to

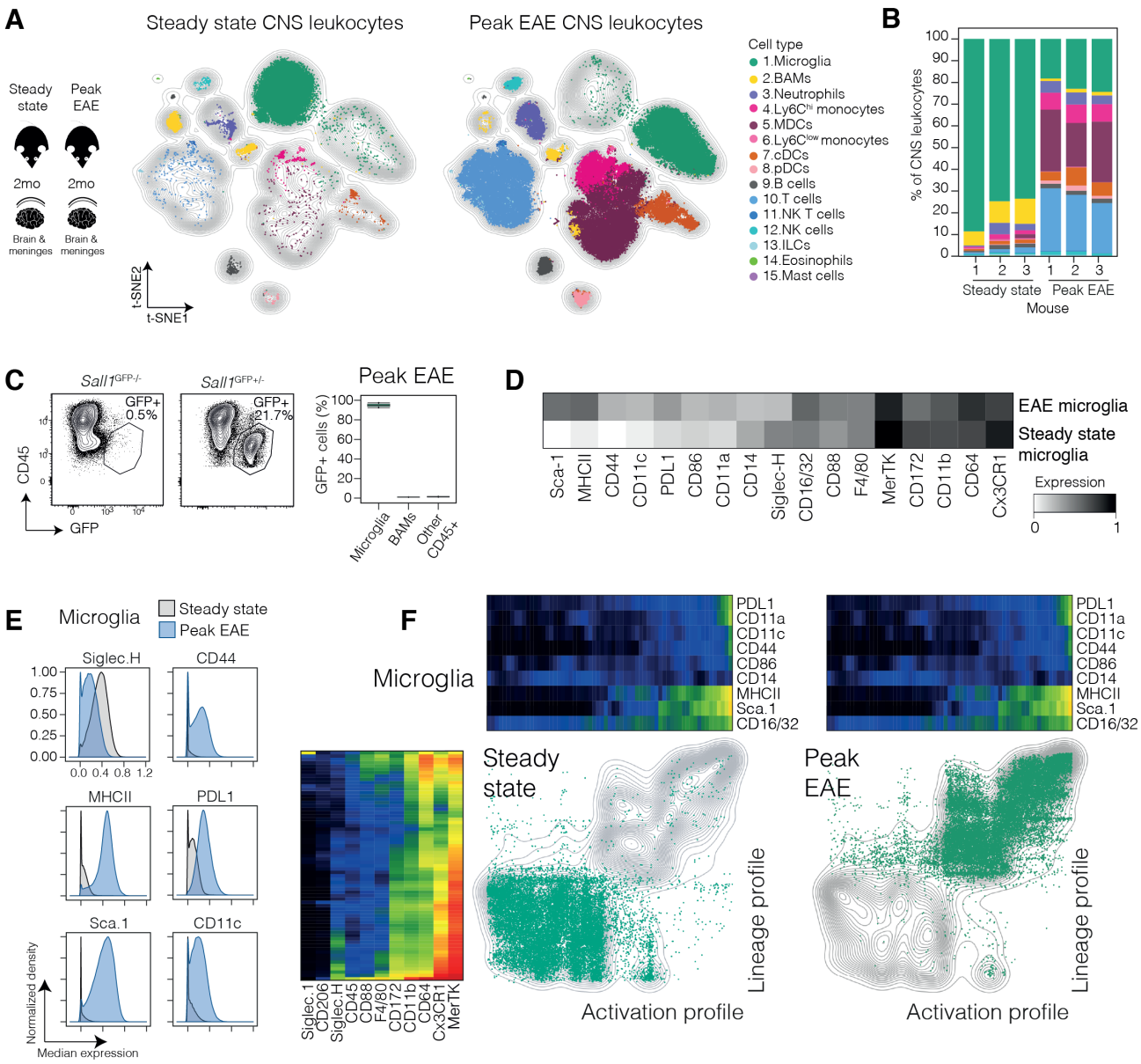

Figure 6. Neuroinflammation Results in CNS Invasion and Complete Microglial Reactivity. EAE was induced in adult (2-month-old) C57BL/6 mice and CNS cells were analyzed by mass cytometry at the peak of disease, and in control steady-state mice. (A) Clustered leukocytes on a t-SNE map generated from the combined steady-state and EAE data (100,000 cells) (B) Frequencies of leukocytes within total CNS leukocytes in steady-state and peak EAE (n = 3, representative of 5 independent experiments). (C) CD45$^+$ CNS leukocytes (left) from *Sall1*$^{GFP+/-}$ reporter and control mice at peak EAE, with quantification (right) of GFP$^+$ cells (n = 3, representative of two independent experiments). (D) Median expression profiles of steady-state and peak EAE microglia. (E) Representative histograms showing highly up-regulated makers between steady-state and peak EAE microglia. (F) One-SENSE analysis comparing the lineage and activation profiles of steady-state and peak EAE microglia. See also Figure S6.

each other while BAMs and pDCs were distinctly separated on the t-SNE map (Figure S7A). We used *Cx3cr1*^{CreER} *Rosa26*-RFP EAE mice to validate that BAMs and MdCs were indeed identified correctly. At peak EAE, as in steady state, only microglia and BAMs were RFP^{+} (Figure 7A and S7B). However, the number of total and RFP^{+} BAMs decreased during EAE relative to steady state and BAMs became outnumbered by infiltrating MdCs (Figure 7B and S6C). As with microglia, the BAM phenotype was entirely altered in EAE (Figure 7C): inflammation led to increased expression of MHCII and the activation markers CD44 and Sca-1, as well as PDL1, CD117 and CD11c (Figure 7D).

Ly6C^{hi} monocytes invade the CNS parenchyma and differentiate into inflammatory and pathogenic MdCs during EAE (Codarri et al., 2013; Croxford et al., 2015a; Yamasaki et al., 2014). Ly6C^{hi} monocytes did not yet undergo inflammation-induced phenotypic changes (Figure S7A), while MdCs were highly activated, expressing Sca-1, MHCII, PDL1, CD11a, CD86, CD38, CD14 and CD16/32 and a macrophage-like lineage profile (Figure 7E). This has previously rendered them hard to distinguish from microglia and BAMs. We also distinguished cDC subsets and pDCs and show their lineage and activation profiles during peak EAE (Figure 7F).

Finally, we defined a myeloid panel of 12 markers within our mass cytometry data to clearly discern reactive microglia, BAMs, MdCs and cDCs even in the inflamed CNS (Figure 7G). Together, our analysis shows that CNS-resident myeloid cells become highly activated during neuroinflammation but can still be distinguished from macrophage-like invading MdCs, confirming the utility of our high-dimensional myeloid immune atlas as a valuable resource for marker combinations allowing mapping of cellular subsets in downstream analysis.

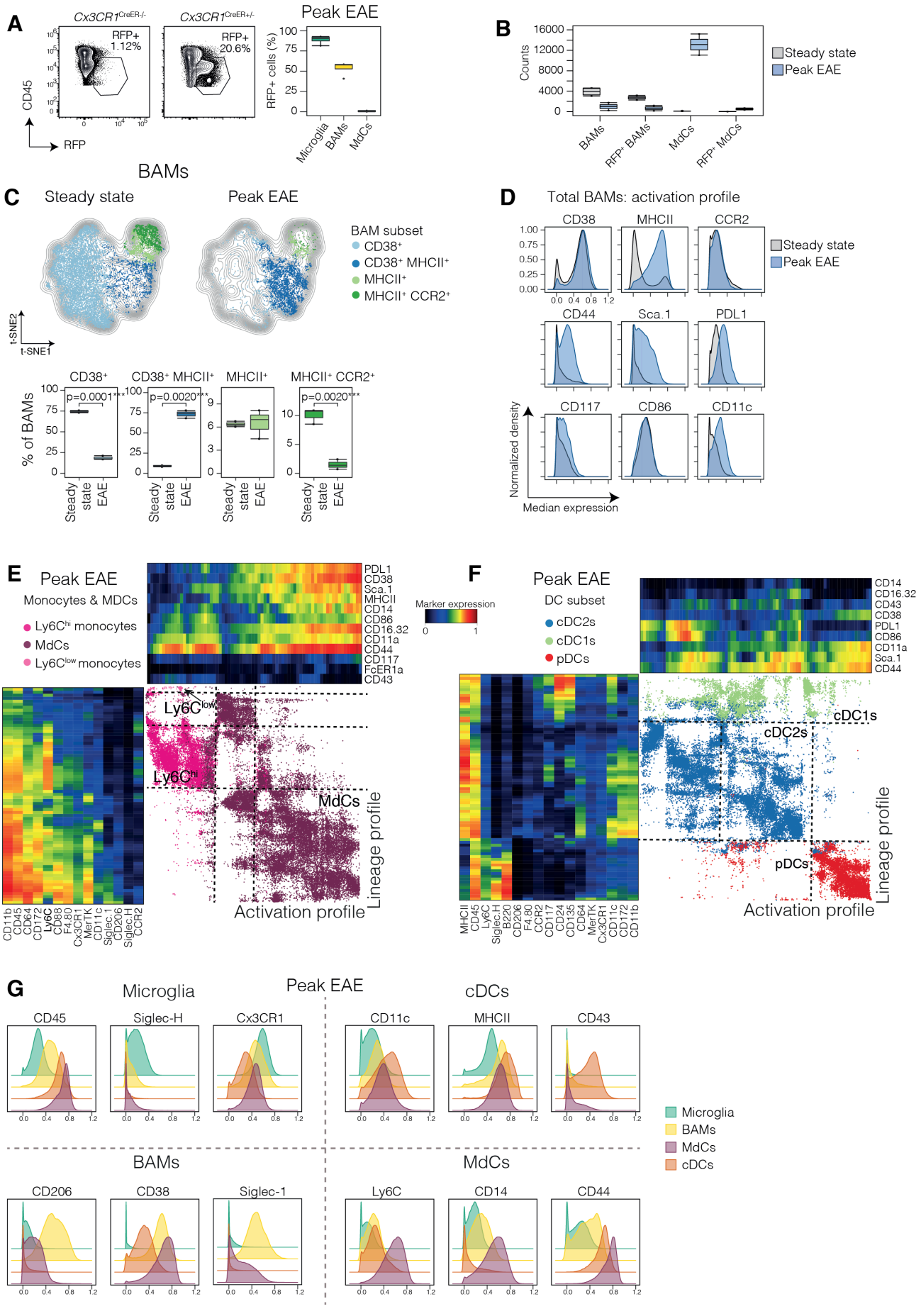
A
Cx3CR1CreER-/-
Cx3CR1CreER+/-
RFP+ 1.12%
RFP+ 20.6%
CD45
RFP
Peak EAE
RFP+ cells (%)
Microglia
BAMs
MdCs
BAMs
B
Counts
Steady state
Peak EAE
BAMs
RFP+ BAMs
MdCs
RFP+ MdCs
C
Steady state
Peak EAE
BAM subset
CD38+
CD38+ MHCII+
MHCII+
MHCII+ CCR2+
t-SNE2
t-SNE1
% of BAMs
p=0.0001***
p=0.0020***
p=0.0020***
Steady state
EAE
D
Total BAMs: activation profile
CD38
MHCII
CCR2
CD44
Sca.1
PDL1
CD117
CD86
CD11c
Steady state
Peak EAE
Normalized density
Median expression
E
Peak EAE
Monocytes & MDCs
Ly6Chi monocytes
MdCs
Ly6Clow monocytes
PDL1
CD38
Sca.1
MHCII
CD14
CD86
CD16.32
CD11a
CD44
CD117
FcER1a
CD43
Marker expression
Ly6Clow
Ly6Chi
MdCs
Activation profile
Lineage profile
CD11b
CD45
CD64
CD172
Ly6C
CD88
F4.80
Cx3CR1
MerTK
CD11c
Siglec.1
CD206
Siglec.H
CCR2
F
Peak EAE
DC subset
cDC2s
cDC1s
pDCs
CD14
CD16.32
CD43
CD38
PDL1
CD86
CD11a
Sca.1
CD44
cDC1s
cDC2s
pDCs
Activation profile
Lineage profile
MHCII
CD45
Ly6C
Siglec.H
B220
CD206
F4.80
CCR2
CD117
CD24
CD135
CD64
MerTK
Cx3CR1
CD11c
CD172
CD11b
G
Microglia
Peak EAE
cDCs
CD45
Siglec-H
Cx3CR1
CD11c
MHCII
CD43
BAMs
MdCs
CD206
CD38
Siglec-1
Ly6C
CD14
CD44
Microglia
BAMs
MdCs
cDCs

Figure 7. BAMs Lose their Heterogeneity during Neuroinflammation but are Still Distinguishable from MdCs and DCs. (A) $CD45^+$ CNS leukocytes (left) from *Cx3cr1*^{CreER} *Rosa26*-RFP and control mice at peak EAE, with quantification (right) of RFP^+ cells (n = 2, representative of two independent experiments). (B) Total numbers of BAMs, RFP^+ BAMs and MdCs in steady-state and peak EAE *Cx3cr1*^{CreER} *Rosa26*-RFP mice. (C) BAM subset tSNE analysis by mass cytometry between steady-state and peak EAE mice. (D) Highly up-regulated makers between steady-state and peak EAE total BAMs. (E) One-SENSE analysis of lineage and activation profiles of $Ly6C^{hi}$ monocytes, MdCs and $Ly6C^{low}$ monocytes, and (F) DCs during peak EAE. (G) Expression levels of distinguishing markers between microglia, BAMs, MdCs and cDCs during peak EAE. *** = p-value significant with a BH FDR < 1%. Error bars represent range. See also Figure S7.

4. Discussion

We have systematically and unambiguously characterized the entire leukocyte landscape within the mammalian CNS under a range of conditions. While lymphocyte populations can be readily identified via expression of unique canonical antigens, and recent reports have begun to characterize them in the steady-state CNS (Korin et al., 2017), CNS myeloid cells have proven highly challenging to study. The CNS myeloid compartment is the largest CNS-resident immune cell pool and has been implicated in multiple aspects of CNS health and disease, including MS, AD, dementia and Parkinson's disease, as well as psychiatric diseases and behavioral disorders like schizophrenia, autism and depression (Herz et al., 2017; Kettenmann et al., 2013). Using high-dimensional cytometry in combination with neural-network based algorithms, we identified microglia, BAMs, DCs, monocytes, neutrophils, eosinophils and mast cells as separate populations by extensive surface protein phenotyping. These data were corroborated by functional, genetic and fate-mapping approaches. Meningeal neutrophils were the third most abundant cell type within the steady state CNS. Since neutrophils are usually associated with inflammation, this was unexpected, but tissue-resident neutrophils have been reported in the decidua, an immune barrier at the maternal-fetal interface and may be patrolling the steady state CNS or have a homeostatic role there (Amsalem et al., 2014; Shechter et al., 2013a).

Being able to interrogate all the identified populations in the high-dimensional space led us to uncover four previously-uncharacterized BAM subsets, distinguished by differential expression of CD38/Lyve1, MHCII, and CCR2. These patterns of expression are also likely to have direct functional implications: CD38 functions in calcium signaling and is involved in FcγR-mediated phagocytosis (Kang et al., 2012) as well as immunosuppression (Chevrier et al., 2017b), while Lyve1 expression has also been found on embryonically derived cardiac macrophages which are crucial in cardiac repair (Epelman et al., 2014; Stevens et al., 2016). Analogous to CNS BAM subsets, resident macrophages in the testes, which has also limited immune surveillance, exist as a mixed population of embryonically-seeded $CD64^{hi}MHCII^{-}$ and bone marrow-derived $CD64^{low}MHCII^{+}$ cells, both expressing an immunosuppressive gene signature (Mossadegh-Keller et al., 2017). It will be interesting to discover whether the same applies to BAM subsets in the CNS where immune suppression in the steady state is also critical. Interestingly, the testicular $CD64^{hi}MHCII^{-}$ macrophages

expressed relatively higher levels of IL-10, and lower levels of IL-1β than the CD64^{low}MHII^{+} macrophages (Mossadegh-Keller et al., 2017), suggesting that the latter play a more active role in inflammatory responses. Similar findings were reported in cardiac-resident macrophages (Epelman et al., 2014). Since BAM subsets can also be separated based on MHCII expression, MHCII^{+} BAMs may also have more potent immune-stimulatory functions compared to MHCII^{-} BAMs.

Using the markers CD38, or its surrogate Lyve1, and MHCII, we showed that while no BAM subset was exclusive to a particular CNS compartment, Lyve1^{+}MHCII^{+} BAMs were enriched in the pia mater, perivascular space and choroid plexus. The dura mater distinctly lacked Lyve1^{+}MHCII^{+} BAMs and harbored predominantly Lyve1^{-}MHCII^{+} BAMs. As with most tissue-resident macrophages, including microglia (Gomez Perdiguero et al., 2015), BAMs of the pia mater, perivascular space and choroid plexus are seeded during embryogenesis either from the yolk-sac and/or the fetal liver (Goldmann et al., 2016), while the ontogeny of dural BAMs has not been described. By mass cytometry analysis we found that CD38^{-}(Lyve1^{-})MHCII^{+} BAMs can also express CCR2, and which are located in the dura and choroid plexus. Therefore, dural and/or choroid plexus BAMs should also be MHCII^{+}CCR2^{+}. For the choroid plexus BAMs, this is in line with their gradual replacement with CCR2^{+} monocytes and may also apply to dural BAMs, likely representing a fresh hematopoietic myeloid cell to replace the dying BAMs which accumulate there.

The stability of BAMs was previously (Goldmann et al., 2016) determined by imaging YFP^{+}Iba1^{+} BAMs in a *Cx3CR1*^{CreER} *Rosa26*-YFP fate-map system within their local compartments, however only 40% of pial BAMs were YFP^{+} compared to 80-90% of perivascular and choroid plexus BAMs (which decreased with time in the choroid plexus). Our data demonstrate that single positive CD38/Lyve1^{+} BAMs make up approximately 30% of pial BAMs, and that this profile can occur with low to absent CX3CR1 protein expression levels while other, MHCII^{+} BAM subsets expressed high levels of CX3CR1 are likely targeted better in this system. This may explain the lower targeting of pial BAMs in the *Cx3CR1*^{CreER} *Rosa26*-YFP fate-map system. Therefore, in order to fully target pial BAMs the *Cx3CR1*^{CreER} *Rosa26* fate-map system is likely to be inadequate. A targeting system utilizing the CD38 or CD206 promoters may prove to be more useful in tracking and manipulating the majority of BAM subsets, including pial BAMs. This is important particularly because the pia mater is reported to facilitate

entry of effector T cells during EAE via interaction with pial BAMs (Schläger et al., 2016), however the distinction between macrophages and DCs in this study was not clear. The function of the phenotypically different dural BAMs in CNS homeostasis and disease likely also differs from pial, perivascular and choroid plexus BAMs as the dura is not in physical contact with the brain and encloses a lymphatic system within its sinuses. The differential surface proteome of BAM subsets and their enrichment within specific CNS compartments may be related to their different roles in these microenvironments. Importantly, by defining a detailed surface protein profile of BAMs and their subsets, it will now be possible to purify these cells for detailed study. It will be interesting to discover their gene signatures and functions within the different CNS compartments, and to determine whether they are shaped by their particular microenvironment or whether fate is dictated by ontogeny.

Besides BAMs, we were also able to discern multiple subsets of DCs, including cDC1, cDC2 and pDC subsets within the steady-state CNS. A clear distinction between DCs and BAMs has not been easy in the past and has led to claims regarding superior APC capacities of both DCs (Greter et al., 2005) and BAMs (Schläger et al., 2016). With our resource, it is now possible to unambiguously discern BAMs from DCs using specific markers, and therefore to target them in functional studies. Adding to the complexity of assigning APC function within the CNS, DC subsets have distinct pattern recognition receptor signatures and are thought to induce specific adaptive immune responses (Schlitzer et al., 2015). Future studies will be needed to determine whether/which of the identified CNS DC subsets sample CNS antigens and migrate to the draining cervical lymph nodes to activate naïve T cells; this is relevant both during CNS infections and in neurodegeneration, where pathogenic protein aggregates accumulate within the CNS parenchyma and meninges (Kalaria et al., 1996). The immune-stimulatory functions of pDCs, cDC1s and cDC2s within peripheral organs may not apply to the CNS, where presumably immune suppression rather than activation is critical to avoid disruption of brain function. Interestingly, it was recently reported that in the human fetus, where immune activation would be critically harmful, cDC1s and cDC2s perform normal migratory and antigen sampling functions but promote Treg induction and actively inhibit T helper cell activation through tolerogenic mechanisms (McGovern et al., 2017). Whether a similar role can be assigned to CNS DCs during homeostasis remains to be determined.

We extended our analysis to pathologic processes of aging and neurodegenerative disease. Aging, characterized by some degree of inflammation (Deleidi et al., 2015), had a dramatic impact on CNS-resident phagocytes. Importantly, we identified a specific subset of microglia associated with aging which had a reactive phenotype characterized by up-regulation of phagocytic and activation/inhibition markers, and with down-regulation of microglial inhibitory-checkpoint markers. In a model of Alzheimer's disease, microglia with the same signature were observed even in relatively young mice; thus, microglial changes observed during aging and AD-like pathology in APP/PS1 mice may not represent a cell intrinsic program, but rather a specific response to cues from the local microenvironment. These cues may to some extent be similar in geriatric and APP/PS1 mice, for example age-related myelin fragmentation (Safaiyan et al., 2016), age- and AD-related protein accumulation (David, 2012) and neurodegeneration (Wyss-Coray, 2016) as well as increased inflammatory mediators (Deleidi et al., 2015; Heppner et al., 2015).

A recent report using single cell RNA sequencing of microglia in the 5XFAD mouse model for AD and in the $SOD1^{G93A}$ mouse model for amyotrophic lateral sclerosis (ALS) showed that similar disease-associated microglia appear with disease progression and up-regulate genes involved in lipid metabolism and phagocytosis, including *Itgax* (CD11c, confirmed in our data) (Keren-Shaul et al., 2017). However, regulation of mRNA and the encoded protein can differ dramatically and sc-RNAseq will, depending on the analysis depth, only detect abundant transcripts (Peterson et al., 2017). In support of this notion, many of the proteins we and others use to describe the CNS immune landscape did not overlap with the public sc-RNAseq data (http://www.ncbi.nlm.nih.gov/geo/query/acc.cgi?acc=GSE98969) (Keren-Shaul et al., 2017). Thus, our analysis uniquely provides surface protein markers, which can be targeted with commercially available mAbs, enabling cell isolation for further studies.

Furthermore, this disease-associated microglial signature was shown to be regulated by the TREM2-APOE pathway across different CNS pathologies, including in APP/PS1 and $SOD1^{G93A}$ mice, and is initiated by phagocytosis of degenerating apoptotic neurons (Krasemann et al., 2017). These studies made us of genetic and morphological analyses to identify these disease-associated microglia.

We also deeply characterized the aggressively inflamed EAE CNS in which the leukocyte composition is changed due to the influx of inflammatory leukocytes, termed

infiltrating or invading cells. A recent report (Korin et al., 2017) suggested that all cells that are not $CD45^{low}$ myeloid cells in the steady state are CNS-infiltrates. However, this study does not take into account that leukocytes in the steady state CNS are not truly parenchymal infiltrating cells as CNS infiltration is accompanied by inflammation. Furthermore, they proposed CD44 as a distinguishing marker for CNS-infiltrating cells during inflammation, whereas we found CD44 to be clearly expressed by CNS-resident leukocytes and is further up-regulated by microglia and BAMs during EAE, and by age- and AD- associated microglia. Hence, CD44 is a poor marker for invading vs. resident cells as a result of the inflammatory changes.

During EAE, CNS-infiltrating monocytes and their pathogenic progeny, MdCs, could not previously be distinguished from reactive microglia and other resident phagocytes as conventional approaches cannot resolve their largely-overlapping phenotypes. We were able to discriminate subsets of infiltrating and resident myeloid cells during EAE, and uncovered a massive influx of infiltrating T cells, monocytes and MdCs in the EAE brain. These MdCs displayed a homogenous macrophage-like phenotype, consistent with their proposed role in myelin degradation and phagocytosis during EAE (Spath et al., 2017; Yamasaki et al., 2014). In contrast to high numbers of MdCs and cDCs, total cell numbers of BAMs decreased during EAE, in agreement with report describing that tissue-resident macrophage numbers decline with the influx of peripheral inflammatory monocytes, but later self-renew once the inflammation is resolved (Davies et al., 2013). At peak disease, BAMs almost exclusively expressed an inflammation-associated signature, characterized by co-expression of CD38 and MHCII, and lack of CCR2. This BAM signature was also seen in geriatric mice, but to a lesser extent. Future studies addressing the plasticity of BAM subsets will determined whether this loss of heterogeneity and expression of a universal $CD38^{+}MHCII^{+}$ phenotype during inflammation is due to individual subset changes or outnumbering by proliferating $CD38^{+}MHCII^{+}$ BAMs already present at steady state.

In EAE, microglia became skewed towards a highly reactive phenotype, with a reduction in microglial inhibitory-checkpoint marker expression. The reactive phenotype seen during EAE bore similarities to the AAM signature in aging and APP/PS1 mice, and may in part represent a universal disease-associated microglial signature, as recently proposed (Krasemann et al., 2017; Zrzavy et al., 2017). However, EAE microglia also differed from the phenotype seen in aging and AD-prone mice: for

example, EAE microglia dramatically up-regulated expression of MHCII and Sca-1, both IFNγ-responsive genes, which may reflect an increased potential for activating T cells. Strikingly, the entire microglia population in the brain parenchyma during EAE homogeneously change to display a highly reactive phenotype, compared to a small subpopulation of microglia which responds to aging and amyloidosis. This is likely due to the cytokines and other inflammatory mediators delivered to the CNS by invading leukocytes and suggests that inflammatory lesions in EAE affect microglia across the brain parenchyma even if accumulating lesions are distant in the spinal cord. In fact, activation of microglia in so-called "normal-appearing white matter" in the cortex of MS patients has been well documented (Vercellino et al., 2017). In contrast, during aging and amyloidosis, the vast majority of microglia do not respond and/or contribute to the pathogenesis, supporting the notion that age-associated changes do not lead to the massive immune cell influx into the CNS as seen in diseases such as EAE and MS.

Taken together, our atlas identified novel subsets of BAMs, steady-state and reactive microglia, and CNS DC subsets. We confirmed the identities of each population by reporter- and fate-mapping, ontogeny and responsiveness to growth factors. Using our steady-state map to interrogate the same leukocytes during pathology, we defined robust signatures for BAMs and microglia during aging, neurodegeneration and neuroinflammation. This atlas can now be used to target and isolate CNS leukocyte subsets with cell-surface protein markers in steady state and their specific disease-associated forms across pathologic conditions, thus enabling further studies into the role of these important cells in maintaining CNS homeostasis and in the initiation or resolution of CNS disease.

5. Supplementary tables and figures

5.1. Table S1. Antibody Panels used to Interrogate the CNS Immune Landscape by Mass and Flow Cytometry, and Immunohistochemistry.

Antigen	Description	Cell type	CyTOF	FACS	IHC
Lineage markers					
CD45	TCR and BCR signal transduction	Pan immune	✔	✔	
B220	Co-stimulation	B cells, pDCs	✔	✔	
CD3	T cell co-receptor	T cells	✔	✔	
NK1.1	Cytotoxicity	NK cells	✔	✔	
CD172	Don't eat me signal	Myeloid cells, stem cells, neurons	✔		
CD90	Cell adhesion and communication	T cells, ILCs, NK cells, stem cells, neurons	✔	✔	
Ter119	Glycophorin A-associated protein	Erythrocytes	✔		
MerTK	Multifunctional	Macrophages	✔	✔	
CD11c	Cell-cell contact	DCs	✔	✔	✔
Iba-1	Calcium binding protein	Macrophages			✔
Collagen IV	Binds collagen in basal lamina	Endothelial cells			✔
vWF	Von Willebrand Factor	Endothelial cells			✔
Fc & complement receptors					
FcER1a	High affinity IgE receptor	Mast cells, basophils, monocytes, DCs	✔		
CD64	High affinity IgG receptor	Macrophages, monocytes	✔	✔	
CD16/32	Low affinity IgG receptors	Myeloid cells, NK cells	✔		
CD88	Complement receptor 5	Granulocytes, monocytes, macrophages	✔	✔	
CD11b	Complement receptor 3	Myeloid cells, NK cells	✔	✔	
Siglecs					
Siglec-F	Putative adhesion function	Eosinophils, alveolar macrophages	✔		
Siglec-H	Reduces type 1 IFN response	Microglia, pDCs	✔	(✔)	
Siglec-1	Cell adhesion	Macrophages	✔		
Immune modulation					
MHCII	Antigen presentation	Antigen presenting cells	✔	✔	✔
CD86	Co-stimulatory ligand	Antigen presenting cells	✔		
PD-L1	Co-inhibitory ligand	Multiple cell types	✔		
Sca-1	Activation marker	Hematopoietic progenitors, lymphocytes, activated cells	✔		
CD14	LPS co-receptor	Macrophages	✔		
CD38	Cell adhesion, calcium signalling	Macrophages, lymphocytes, neurons	✔	✔	
CD11a	Cell adhesion and co-stimulation	Multiple cell types	✔		
CD206	Pattern recognition receptor	Macrophages, dendritic cells	✔	✔	✔
Adhesion & movement					
F4/80	Cell adhesion	Macrophages, monocytes	✔	✔	
CD24	Cell adhesion	B cells, granulocytes,DCs	✔	✔	
Lyve-1	Binds endothelial cells	Lymphatic vessels, macrophages	✔	✔	
Ly6G	Migration	Neutrophils, subset of eosinophils	✔	✔	✔
CD43	Locomotion, anti-adhesive	Monocytes, dendritic cells, granulocytes	✔		
Cx3CR1	Adhesion and migration	Macrophages, moncytes, lymphocytes	✔	✔	
CCR2	Monocyte chemotaxis	Monocytes, macrophages, immature B cells	✔		
Lyve-1	Adhesion	Macrophages, lymphatic endothelial cells		✔	✔
CD44	Adhesion, migration, homing	Most cell types	✔	✔	
Survival factors					
CD135	Survival, proliferation, differentiation	Hematopoietic progenitors, dendritic cells	✔		
CD117	Survival, proliferation, differentiation	Hematopoietic progenitors, mast cells, ILCs, DCs	✔		

5.2. Figure S1. Identification of CNS Resident Leukocytes, Related to Figure 1.

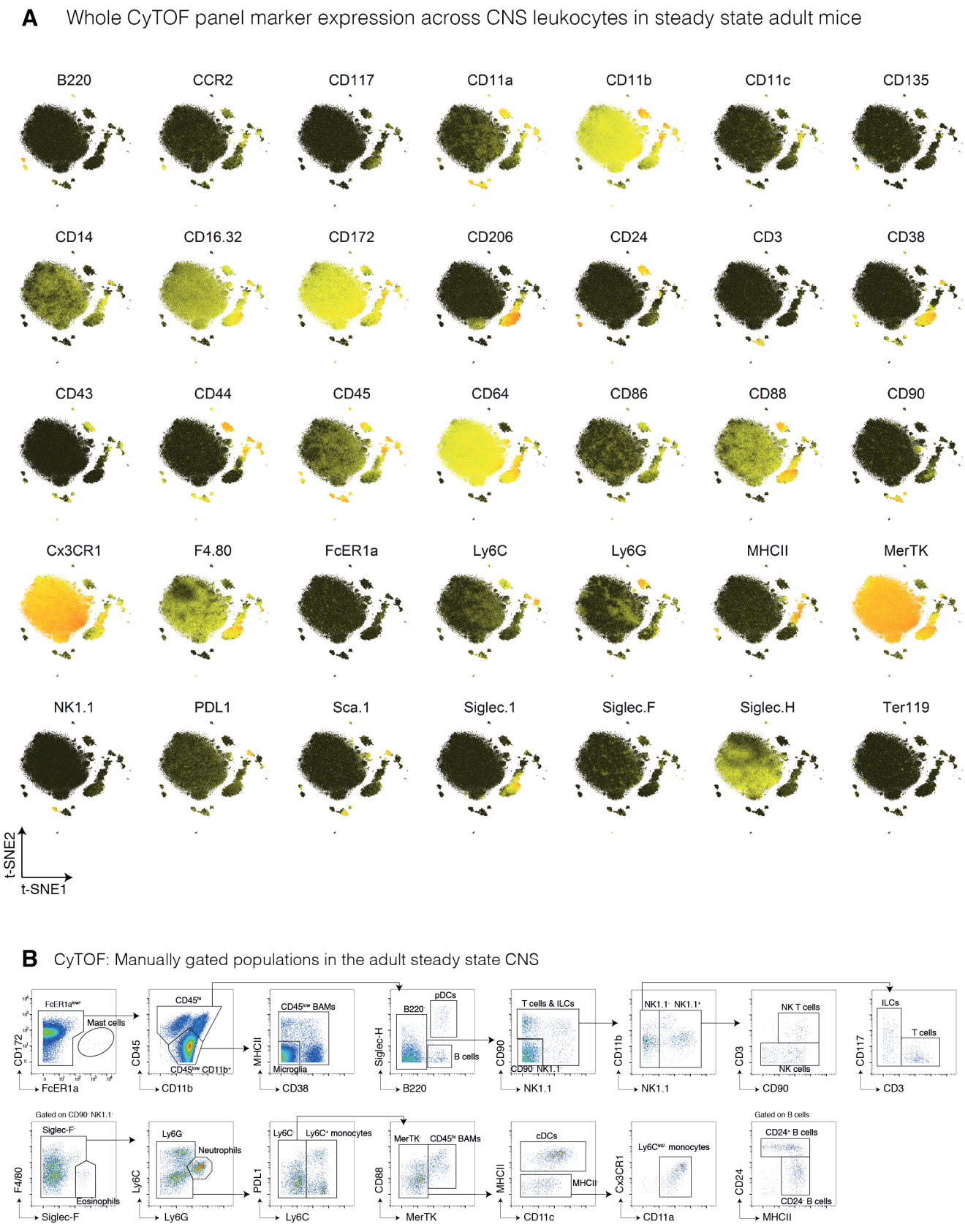

Figure S1. Identification of CNS Resident Leukocytes, Related to Figure 1. (A) Mass cytometry panel markers overlaid onto the t-SNE from Figure 1(A) of steady-state adult CNS leukocytes. (B) Manual gating of mass cytometry data on major leukocyte populations.

5.3. Figure S2. Tracking blood leukocytes in the CNS, Related to Figure 1.

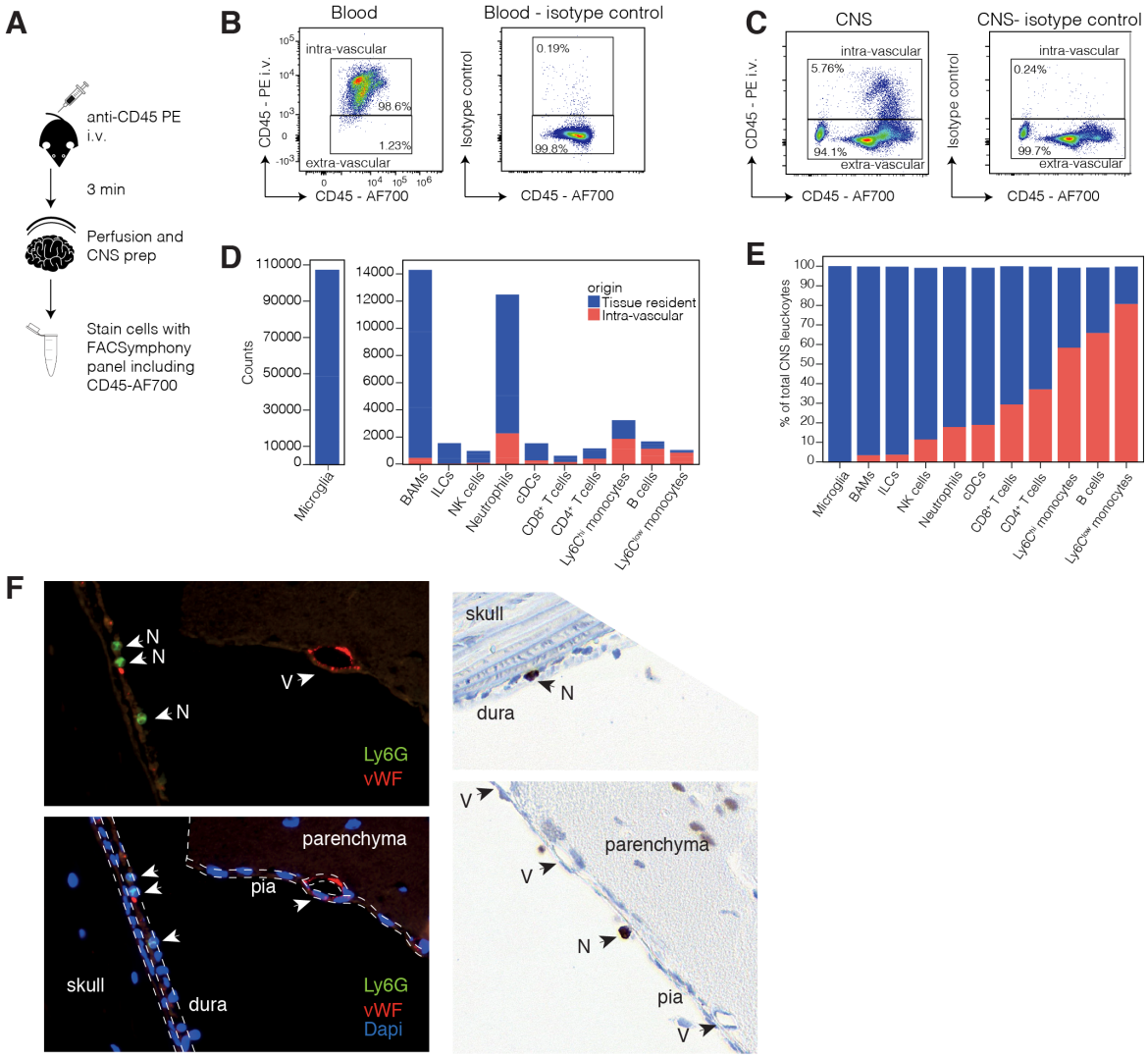

Figure S2. Tracking blood leukocytes in the CNS, Related to Figure 1. (A) Intravascular leukocyte tracking by administering anti-CD45-PE i.v. with sacrifice and perfusion after 3 minutes, CNS isolation and single cell staining with fluorescence cytometry mAbs which included a second anti-CD45 in AF700. (B) Peripheral blood and (C) CNS leukocytes after anti-CD45-PE or isotype administration. Quantification of labeled intra-vascular cells (red) and unlabeled tissue-resident cells (purple) by total numbers (D) and frequencies (E) (n = 3, representative of 3 independent experiments). (F) Localization of CNS-resident neutrophils in the dura and pia mater in 4 µm sections of decalcified skulls with intact CNS (green = Ly6G, red = vWF (Von Willebrand Factor vessel marker), blue = DAPI) and DAB staining (brown = Ly6G).

5.4. Figure S3. Identification of Microglia and BAMs by Genetic Targeting, Related to Figure 2.

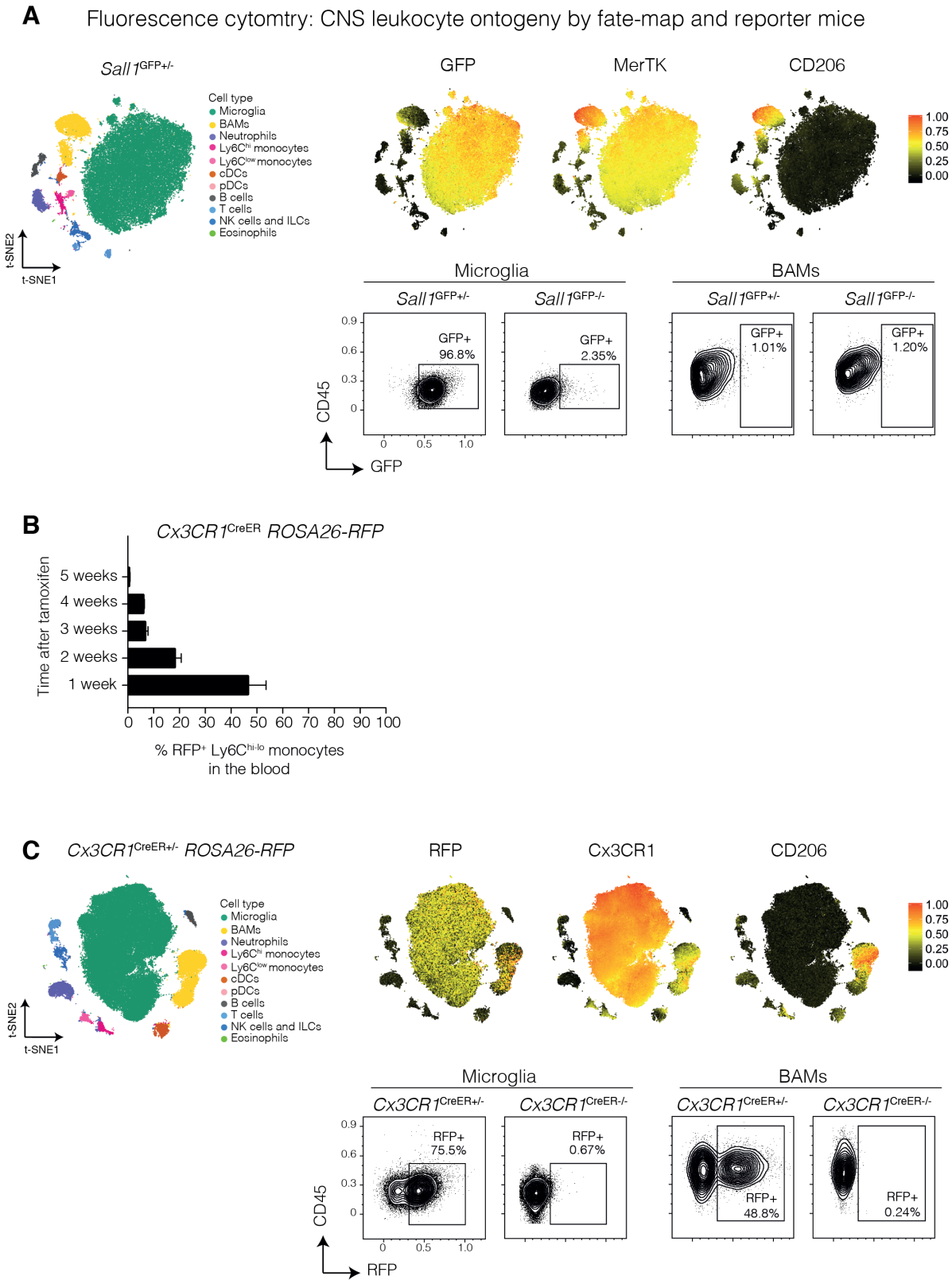

Figure S3. Identification of Microglia and BAMs by Genetic Targeting, Related to Figure 2. (A, top panel) t-SNE map and clustering of the steady-state adult CNS in *Sall1*$^{GFP+/-}$ mice using 22-color fluorescence cytometry (left); GFP, MerTK and CD206 expression overlaid onto the t-SNE map (right). (Bottom panel) Representative gating for GFP^{+} microglia and BAMs. (B) Frequency of RFP^{+} Ly6C^{hi-lo} monocytes in the blood following tamoxifen administration on day 0 and day 2 in *Cx3cr1*^{CreER} *Rosa26*-RFP mice. (C, top panel) t-SNE map and clustering of the steady-state adult CNS in *Cx3cr1*^{CreER} *Rosa26*-RFP mice, 5 weeks after tamoxifen administration, using 22-color fluorescence cytometry (left); GFP, MerTK and CD206 expression overlaid onto the t-SNE map (right). (Bottom panel) Representative gating for RFP^{+} microglia and BAMs.

5.5. Figure S4. Localizing BAM subsets within CNS compartments, Related to Figure 3.

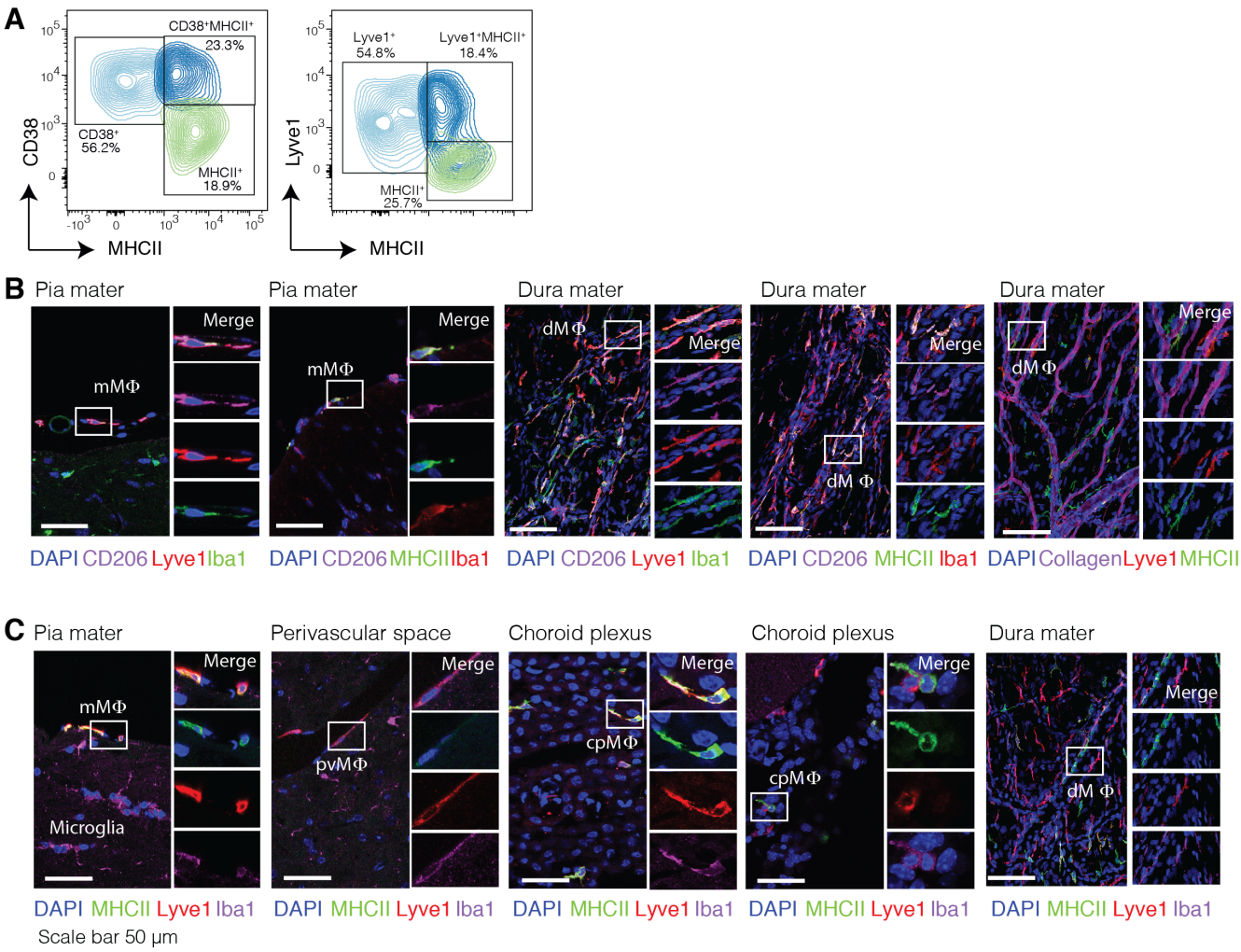

Figure S4. Localizing BAM subsets within CNS compartments, Related to Figure 3. (A) Frequencies of BAM subsets determined by using CD38 or Lyve1. (B) Representative images showing co-labeling of MHCII and Lyve1 with CD206 and in relation to collagen^{+} vasculature in the indicated regions of the CNS. (C) Representative images showing Lyve1^{+}, Lyve1^{+}MHCII^{+} and MHCII^{+} BAM subsets in the indicated regions of the CNS. mMϕ = meningeal macrophage; pvMϕ = perivascular macrophage; cpMϕ = choroid plexus macrophage; dMϕ = dural macrophage.

5.6. Figure S5. In-depth Characterization of the CNS Leukocytes in a Mouse Model for Alzheimer's Disease, Related to Figure 5.

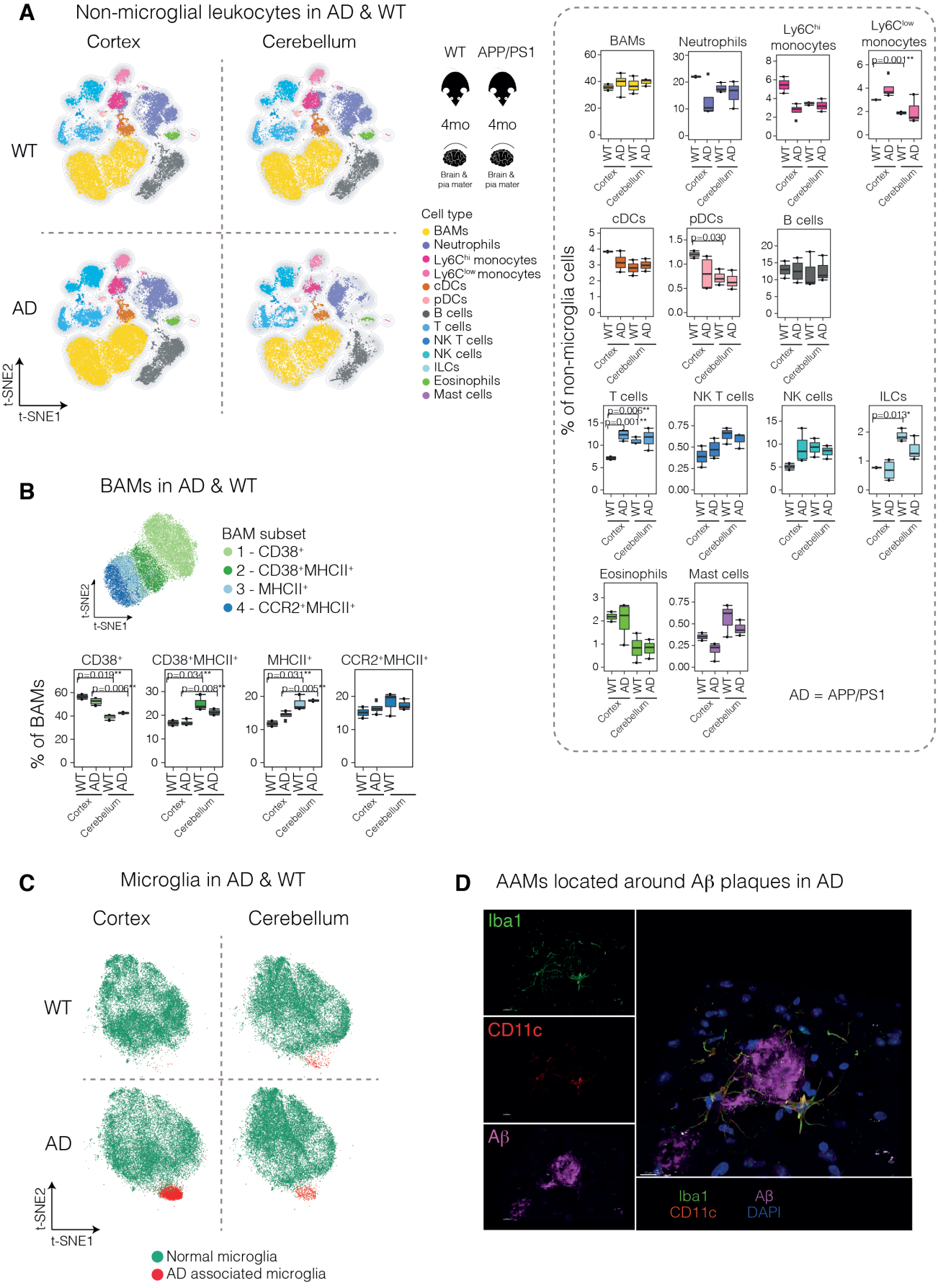

Figure S5. In-depth Characterization of the CNS Leukocytes in a Mouse Model for Alzheimer's Disease, Related to Figure 5. (A, left) Complete analysis of non-microglial CNS leukocytes between 4-month-old WT and APP/PS1 mice (cortex and cerebellum combined) depicted in the t-SNE map with clustered cell populations and (right) their frequencies compared between the WT and APP/PS1 cortex and cerebellum. (B) BAM subset frequencies between WT and APP/PS1 cortex and cerebellum. (C) Differential t-SNE map of AD-associated and normal microglia between WT and APP/PS1 cortex and cerebellum. (D) AD-associated microglia located around Aβ plaques in APP/PS1 mice.

5.7. Figure S6. EAE-induced CNS Invasion by Peripheral Leukocytes and Reactivity of Microglia, Related to Figure 6.

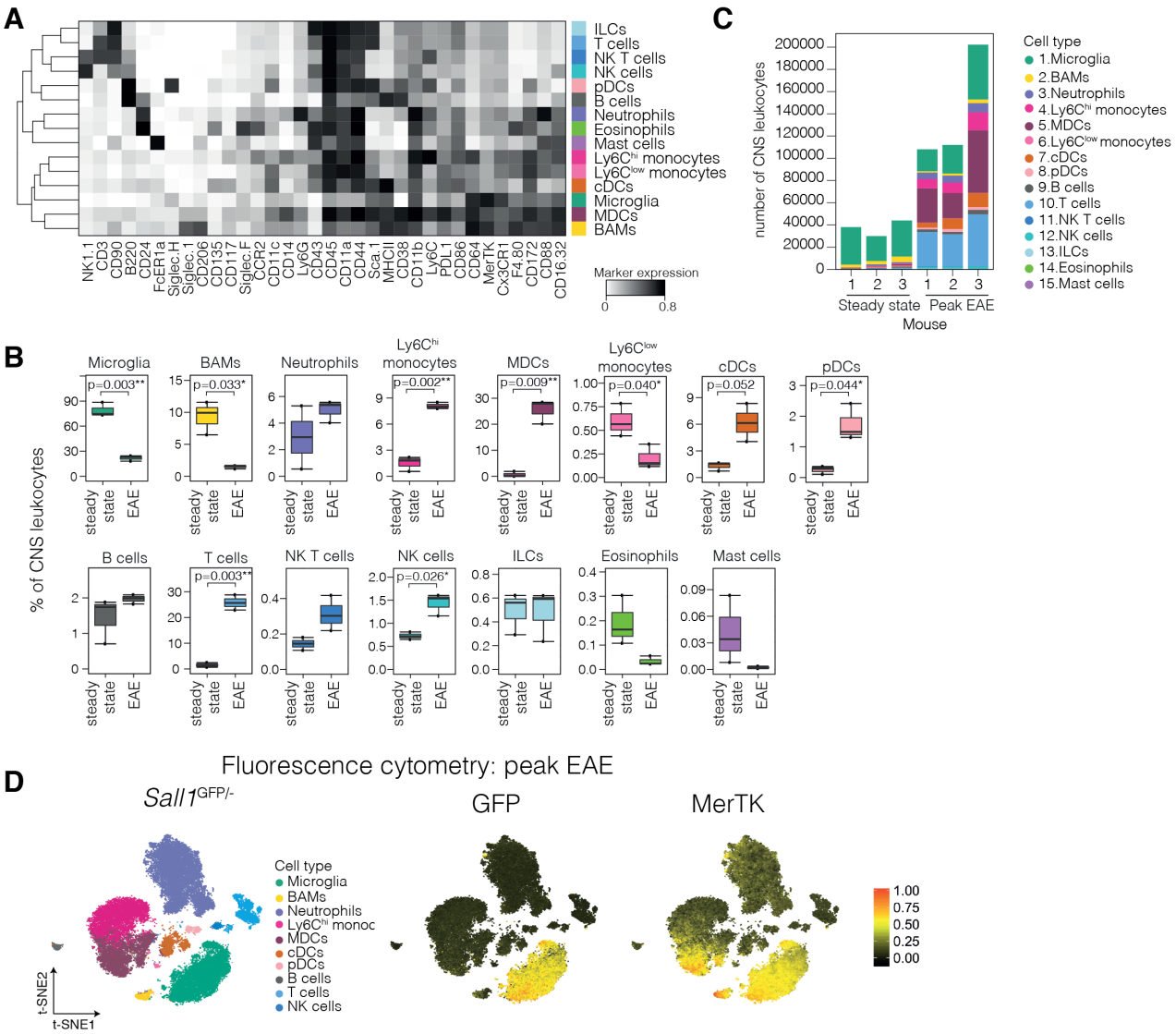

Figure S6. EAE-induced CNS Invasion by Peripheral Leukocytes and Reactivity of Microglia, Related to Figure 6. (A) Median marker expression profile of CNS leukocytes of adult C57BL/6 mice at peak EAE. (B) Cell frequency and (C) number comparison of steady-state CNS-resident and peak EAE invading leukocytes. (D, left) t-SNE of all CNS leukocytes in *Sall1*$^{GFP+/-}$ mice at peak EAE, measured by fluorescence cytometry. (right) GFP and MerTK expression overlaid onto the t-SNE map. (E, see following page) Myeloid cell marker expression by steady-state resting microglia and peak EAE activated microglia on a t-SNE map generated using the combined microglia dataset.

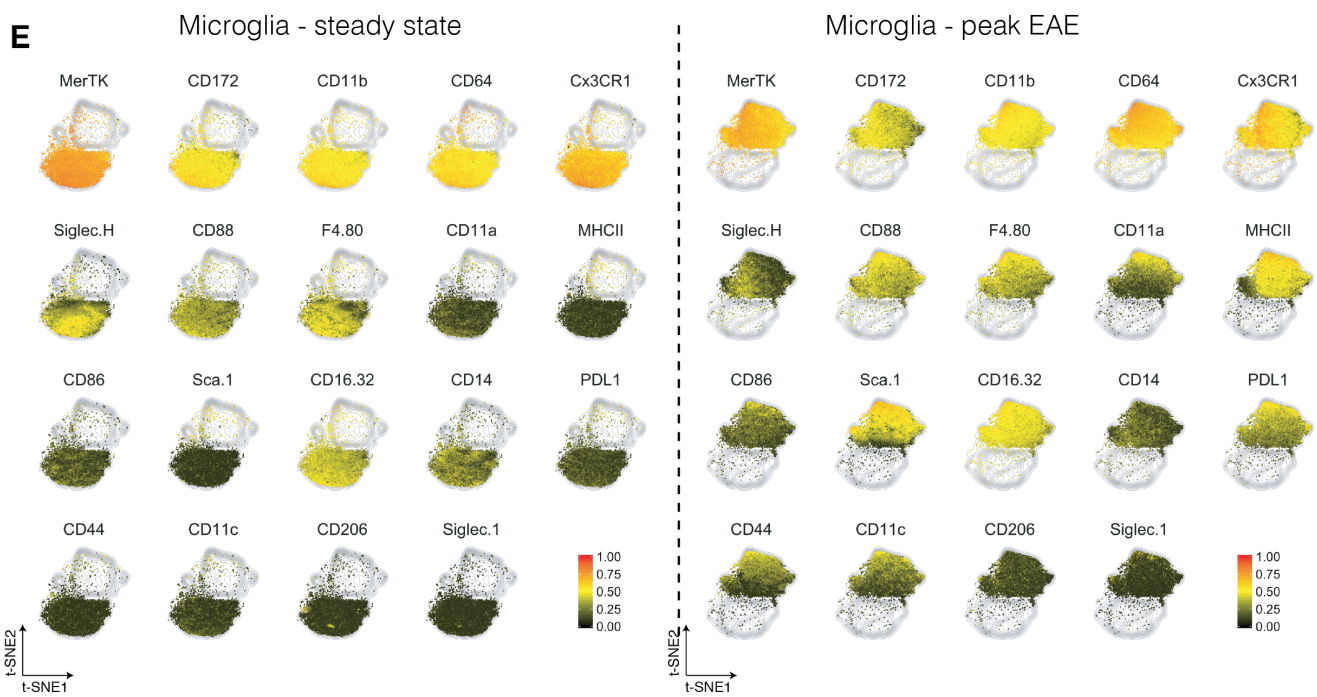
E
Microglia - steady state
Microglia - peak EAE
MerTK
CD172
CD11b
CD64
Cx3CR1
Siglec.H
CD88
F4.80
CD11a
MHCII
CD86
Sca.1
CD16.32
CD14
PDL1
CD44
CD11c
CD206
Siglec.1
1.00
0.75
0.50
0.25
0.00
t-SNE2
t-SNE1

5.8. Figure S7. Differentiating Invading Monocytes from BAMs and DCs during EAE, Related to Figure 7.

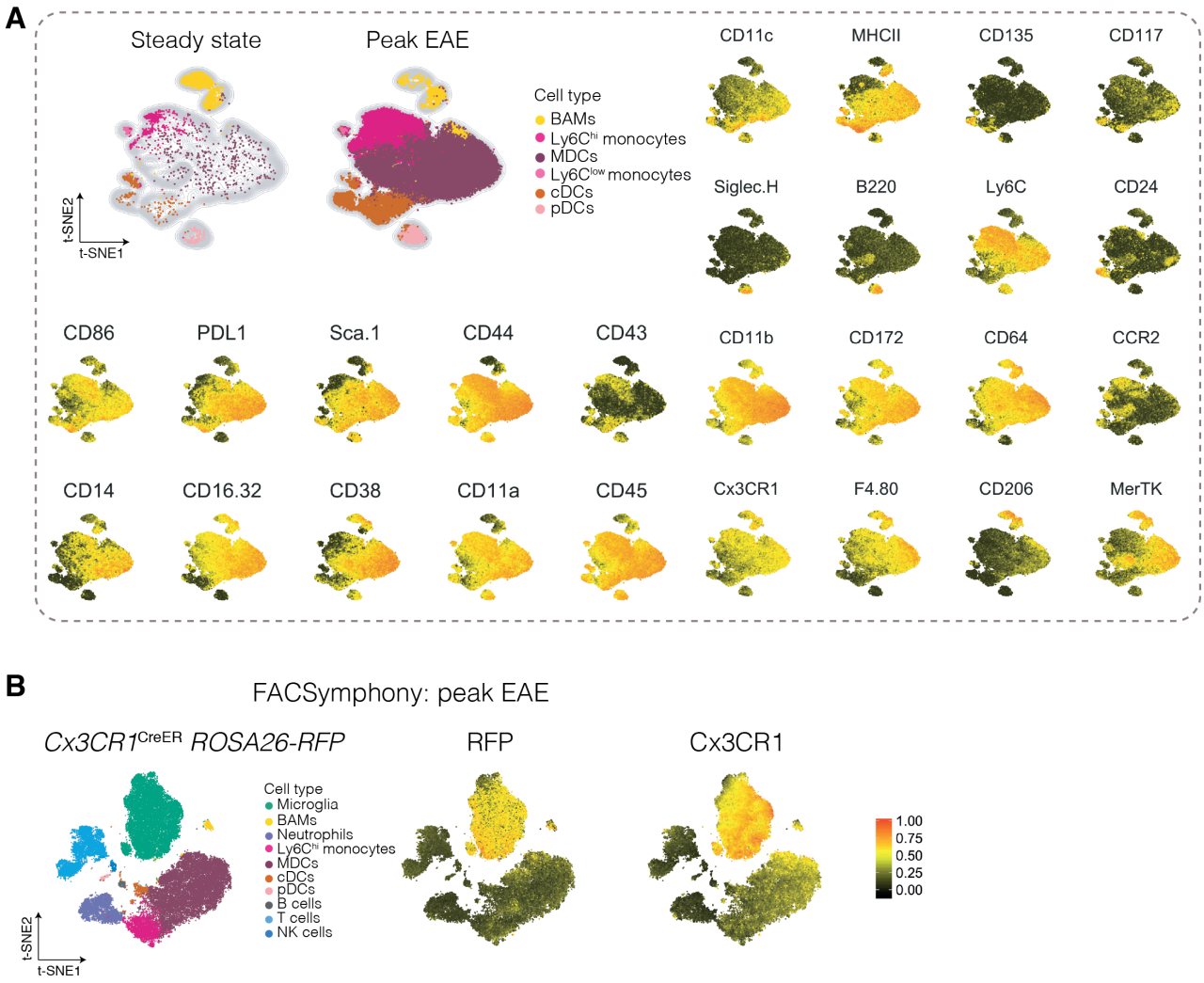

Figure S7. Differentiating Invading Monocytes from BAMs and DCs during EAE, Related to Figure 7. (A) t-SNE depiction and marker expression showing distinction of non-microglial myeloid cell clusters from steady-state and peak EAE CNS. (B, left) t-SNE of all CNS leukocytes in *Cx3cr1*^{CreER} *Rosa26*-RFP mice at peak EAE, measured by fluorescence cytometry. EAE was induced 5 weeks after tamoxifen administration. (right) RFP and CX3CR1 expression overlaid onto the t-SNE map. ** = p-value significant with a BH FDR < 5%. Error bars represent range.

6. Methods

6.1. Experimental procedures

6.1.1. Mice

C57BL/6 (wild-type) mice were purchased from Janvier Laboraories and were taken to adulthood at 8 weeks of age or to geriatric age at 1.5 years of age and tissues were harvested together. *Sall-1*^{GFP} reporter mice were described previously (Yuri et al., 2009). *Cx3cr1*^{CreER} *Rosa26*-RFP fatemap mice were kindly provided by S. Jung (Weizmann Institute of Science) (Yona et al., 2013). Heterozygous APP/PS1 mice which overexpress the familial AD mutant form of human APP (the Swedish mutation, K670N/M671L) and PS1 (M146L/L286V) transgenes under the transcriptional control of the neuron-specific mouse Thy-1 promoter (Radde et al., 2006b), and littermate controls, aged 4 months were kindly provided by F. Heppner (Charité–Universitätsmedizin Berlin). All animal experiments performed in this study were approved by the Cantonal Veterinary Office Zurich.

6.1.2. *In vivo* treatments and EAE induction

Anti-CSF1R (clone AFS98) (Sudo et al., 1995) was administered by intraperitoneal (i.p.) injection on day 0 (2 mg) and day 2 (1 mg), diluted in PBS, and mice were euthanized on day 9. A 10 μg dose of Flt3L was administered i.p. daily for 9 days, after which mice were euthanized. Tamoxifen (Sigma) was dissolved in ethanol and corn oil to 25 mg/ml and administered in 200 μl doses via oral gavage (5 mg/dose) to *Cx3cr1*^{CreER} *Rosa26*-RFP mice every second day for 8-10 days. After 5 weeks mice were either euthanized or immunized for EAE induction: *Cx3cr1*^{CreER} *Rosa26*-RFP mice (5 weeks after tamoxifen administration) or C57BL/6 mice (aged 8 weeks) were injected with MOG_{35-55} peptide emulsified in Complete Freund's Adjuvant sub-cutaneously (s.c.) and Pertussis toxin (List Biological Laboratories) i.p., and scored, as previously described (Mrdjen et al., 2017). Peak of disease was defined when mice reached a score of 3-4 at approximately 14 days after immunization.

6.1.3. Tissue harvesting and cell preparation

Mice were sacrificed by injection of pentobarbital (50 µl at 300 mg/ml) i.p. and transcardiac perfusion was performed with PBS and heparin (5 u/ml). The CNS was harvested and the dura mater was removed from the skull and included in the sample. The complete CNS samples (including meninges and choroid plexus) were processed into single cells as previously described (Mrdjen et al., 2017): briefly, the CNS was cut into small pieces in an eppendorf tube and incubated with digestion buffer (RPMI supplemented with 2% FBS, 2 mM HEPES, 0.4 mg/ml Collagenase D and 2 mg/ml DNAse) for 30 minutes at 37°C, shaking. Enzymatic digestion was stopped with EDTA (5 mM), the sample was homogenized with a syringe and the homogenate was filtered through a 70 µm cell strainer. This was followed by gradient centrifugation with 30% Percoll (GE Healthcare Life Sciences) in PBS (v/v) (23'500 x *g* for 30 minutes at 4°C without brakes), removal of myelin with a suction pump and filtration to generate a single-cell suspension. The samples were then ready for staining with mass- or fluorescence cytometry antibodies.

6.1.4. Mass cytometry

Mass cytometry antibodies were either labeled in-house using antibody-labeling kits and protocols purchased from Fluidigm. Antibodies were individually titrated and optimized as into the final panel prior to use, ensuring that each parameter was informative. We used 5 palladium metal isotopes for live cell barcoding of samples with CD45 (Mei et al., 2015), while keeping CD45-147Sm as a common channel to clearly identify cells expressing varying degrees of CD45, such as microglia, as previously described (Mrdjen et al., 2017). Briefly, individual samples from steady-state adult, steady-state geriatric and peak EAE adult C57BL/6 mice were incubated with respective CD45-Pd + CD45-147 Sm antibodies in PBS for 30 minutes at 37°C after which they were washed twice with FACS buffer (PBS supplemented with 0.5% BSA), then combined into composite samples. In another experiment, the forebrain and hindbrain were taken from 4-month-old APP/PS1 or littermate control mice, barcoded separately, and combined into composite samples. We used one barcoding CD45-Pd per group in combination with CD45-147 Sm in order to avoid epitope saturation and maintain signal intensity, and were therefore able to barcode 5 samples from separate

groups per composite sample. This was followed by incubation of the composite samples with the cocktail of primary panel antibodies (Table S1) for 30 minutes at 37°C, washing with FACS buffer and then incubating with secondary antibodies for 20 minutes at 4°C. After washing, samples were incubated with intercalating solution (Iridium (Sigma) in MaxPar Fix/Perm buffer (Fluidigm)) overnight at 4°C. Prior to acquisition, the samples were washed twice with FACS buffer and once with MilliQ water. Barcoded composite samples were acquired on a Helios mass cytometer (Fluidigm). Quality control and tuning processes on the Helios were performed on a daily basis before acquisition. Data from different days and across acquisition time was normalized by adding five-element beads to the sample immediately before acquisition and using the Matlab-based normalization software, as described previously (Finck et al., 2013).

6.1.5. Fluorescence cytometry

Samples were incubated with primary antibodies in PBS for 30 min at 4°C, washed with PBS and incubated with secondary antibodies for 20 min at 4°C. After washing, cells were fixed and permeabilized with 100µL BD Cytofix/Cytoperm™ (containing 4.2% Formaldehyde) for 20 min at 4°C, and washed with Perm buffer (PBS with 0.1% saponin) before intracellular labeling which was performed for CD3, CD4 and CD8 in Perm buffer for 30 min at 4°C, with final washing in Perm buffer. Samples were resuspended in PBS and analyzed by flow cytometry with a FACSymphony™ cell analyzer. Before acquisition, PMT voltages were adjusted manually in order to reduce fluorescence spillover, and single-stain controls were acquired for compensation matrix calculation.

6.1.6. Tracking intra-vascular cells in the CNS

In order to label intra-vascular cells within the steady state CNS we injected PE conjugated anti-CD45 (7.5 µg in PBS) i.v. into adult C57BL/6 mice and euthanized them after 3 minutes, performed transcardiac perfusion and harvested the CNS, as previously described (Anderson et al., 2014). Single cell suspensions were then stained with fluorescence cytometry antibodies.

6.1.7. Immunohistochemistry for BAMs

C57BL/6 mice were transcardially perfused with PBS and heparin (5u/ml) followed by 2-4% (wt/vol) paraformaldehyde (PFA) in 0.1 M phosphate buffer (pH 7.4). The CNS, excluding the dura mater, was further fixed for 6-12 hours at 4°C and rinsed with PBS followed by cryoprotection with 30% (wt/vol) sucrose in PBS. Samples were embedded in OCT (Medite). Cryo-sectioning was performed with a thickness of 12-30µm using a Hyrax C60 cryostat (Zeiss). The dura mater was fixed for 2-4 hours at 4°C followed by removal from the skull, direct placing onto superfrost plus slides (Thermo Scientific) and storage at -20°C. For quantification of BAM subsets, the choroid plexus was removed from the CNS after fixation and also directly placed onto slides. CNS tissue sections, dura mater and choroid plexus mounts were permeabilized by incubation in blocking solution (PBS supplemented with 0.2% Triton-X 100 and 5% normal goat serum) for 1 hour at room temperature. Sections and tissues on slides were labeled primary antibodies either at 4°C over night or at room temperature for 2 hours, and free-floating sections for 24-72 hours at 4°C in staining solution (PBS supplemented with 0.1% Triton-X 100 and 2% normal goat serum): anti-Iba1 (1:500), anti-MHCII (1:200), anti-Lyve1 (1:200), anti-CD206 (1:100) and anti-CD11c (1:40). After washing, samples were incubated either at 4°C overnight or for 1-2 hours at room temperature with the respective secondary antibodies (anti-rabbit, anti-rat, streptavidin, etc., 1:500-700). Washing was repeated and sections were mounted with 1 drop of IS mounting medium with DAPI (Dianova) or SlowFade Gold antifade reagent with DAPI (Invitrogen). Fluorescence photomicrographs were acquired on a Vectra3 (Perkin Elmer) fluorescence microscope using a x20 objective lens. Filters for AF488, AF546, AF647, AF 660 and DAPI were used for imaging tissues to facilitate subsequent unmixing of all colors according to their respective spectra.

6.1.8. Immunohistochemistry for neutrophils

Mice were transcardially perfused using 4% (wt/vol) PFA. The fur was removed and heads (including the skull and brain) were transferred into USEDECALC solution for 6 days (MEDITE Cancer Diagnostics, USA) and decalcified using ultrasonic decalcifying automate USE 33 (Medite® GmbH, Switzerland). Specimens were subsequently sectioned into 3 µm slices and embedded in paraffin for further

histological processing. Antigen retrieval was performed on sections by microwave heating at 98°C for 15 min (microMED T/T Mega, Hacker-Milestone) in citrate buffer (0.01M citric acid, pH6).

For brightfield immunostaining, endogenous peroxidases were neutralized by incubation in PBS supplemented with 3% H_2O_2, and non-specific binding blocked using PBS supplemented with 10% FCS. Tissue sections were incubated with anti-Ly6G (1:1000). Bound primary antibody was visualized with biotin-labeled anti–rat antibody and streptavidin-peroxidase staining method using polymerized 3,3′-diaminobenzidine (all reagents from Dako; Haemalaun counterstaining of nuclei).

For immunofluorescence staining, non-specific binding was also blocked using PBS supplemented with 10% FCS. Sections were subsequently incubated with anti-Ly6G (1:500) and with rabbit anti-vWF antibody (1:1000). Bound antibodies were visualized with AF555–labeled donkey anti–rabbit (1:200) and Cy3-labeled goat anti–rat (1:200) secondary antibodies. Nuclei were stained with DAPI (1:5000). All antibodies were diluted in DAKO Real™ Antibody Diluent.

6.2. Quantification and statistical analysis

6.2.1. Pre-processing of mass and flow cytometry data

For mass cytometry data live cells were exported by manual gating on Event_length, DNA (191Ir and 193Ir), and live cells (195Pt) using FlowJo software (Tree Star), as previously described (Mrdjen et al., 2017). Next, cells were assigned to their initial samples using Boolean gating in FlowJo. Background subtracted .fcs files were exported from FlowJo, imported into the R environment and transformed using an inverse hyperbolic sine (arcsinh) function with a cofactor of 5 (Bendall et al., 2011). For flow cytometry data, after compensation correction in FlowJo, live, single, background subtracted and compensated cells were exported by manual gating. Samples were not barcoded so debarcoding was not necessary. The appropriate transformation cofactors were determined by uploading the files into Cytobank (www.cytobank.org) (Kotecha et al., 2010) and using the Scales feature; thereafter transformation was carried out in Matlab and transformed files were imported into the R environment for further pre-processing and analysis. To equalize the contribution of each marker in subsequent automated data analysis steps of mass and flow cytometry

data, we performed percentile normalization (Levine et al., 2015), normalizing all data to the 99.9^{th} – 99.99^{th} percentile of the merged sample in each experiment, depending on the number of outliers present. This preserves inter-sample variability in maximum expression values, which might be biologically relevant, and normalizes inter-marker maximum expression values, while maintaining original staining indices.

6.2.2. Automated population identification in high- dimensional data analysis

Pre-processing of the raw data was followed by dimensionality reduction and visualization by t-Distributed Stochastic Neighbor Embedding (t-SNE) (Amir et al., 2013; Mair et al., 2016; Van Der Maaten and Hinton, 2008) with parameters as listed in the figure legends, clustering with FlowSOM into initial 100 nodes (Van Gassen et al., 2015; Weber and Robinson, 2016), followed by expert-guided manual metaclustering using the t-SNE with overlaid marker expression values and a heatmap of median expression values of the initial automated 100 FlowSOM nodes (Hartmann et al., 2016). In some cases, major cell populations were separated for further clustering into subsets. When comparing different groups, for example steady state and EAE samples, the t-SNE and clustering analyses were performed on the combined data sets. Force- and landmark- directed maps were generated with a modified version of the Scaffold application (Spitzer et al., 2015), and landmark populations that were manually gated in FlowJo and exported. We used the 100 initial FlowSOM nodes as unsupervised Scaffold clusters instead of the built-in clustering algorithm of the Scaffold application. This allowed the validation of expert-guided manual metaclustering by the grouping of FlowSOM nodes around manually-gated landmark nodes in the Scaffold map. Categorical ONE-Sense analysis was performed in the R environment by generating a one-dimensional t-SNE axis using lineage or activation markers, and a progressive lineage or activation heatmap along each axis, which were then arranged side-by-side. Statistics were calculated using Student's t-test and the Benjamini-Hochberg post-test for false discovery rates (FDR). Stars were assigned according to the FDR: * = significant (i.e. p-value < 0.5) with a FDR of 10%, ** = significant with a FDR of 5% and *** = significant with a FDR of 1%.

6.2.3. Quantification of cells from immunohistochemistry

Semi-automated cell detection and quantification of BAM subsets was performed using the implemented Inform Software (Perkin Elmer). A minimum of 5 sections per compartment (dura mater, pia mater, perivascular space, choroid plexus), per mouse were analyzed and a minimum of 4 regions of interest per section. Images used for analyses were taken on the SP8 upright (Leica) with a 20× emulsion objective at 1024 × 1024 pixels in *xy*. A pinhole size of 60 µm was used. Images were taken in frames with a line average of 16. DAPI and AF546 were detected in one sequence and AF488 and AF647 were detected in a second sequence. Alternatively, images were taken sequentially with a SP5 Leica confocal laser scanning microscope (Leica) equipped with argon and helium lasers and the 40× (oil immersion, NA1.25) objective. Images were processed and merged by Imaris Imaging software (Bitplane).

7. Acknowledgements

First and foremost, I would like to thank Burkhard Becher for having me in the lab, providing me with many great opportunities in research topics, new methodologies, valuable collaborations and a thriving scientific environment to work in. I also thank him for giving me the freedom and trust to explore these opportunities, enduring my sometimes stubborn determination and guiding my progress with insight but without micro management. I have really learnt a lot during this time here, scientifically and personally, and value it immensely.

I am also grateful to my Ph.D. committee members Bernd Bodenmiller, Christian Münz and Ari Waisman, who gave me useful comments and support during our annual committee meetings.

I thank all our collaborators who provided data, advice and critical feedback for the manuscript resulting from this project, including Felix J. Hartmann, Bettina Schreiner, Sebastian Utz, Brian Leung, Iva Lelios, Frank L. Heppner, Jonathan Kipnis, Doron Merkler, and Melanie Greter. I would also like to thank Anto Pavlović who worked with me during his Masters thesis project and was an outstanding student.

Additionally, I thank Florian Mair for teaching me many things about flow cytometry, mouse work, discussing many immunology related topics with me when I first arrived in the lab, and also for transferring to me my first project in the Becher lab. Thank you to Ines for heling me organize all the permits and documents during my time in Zurich. Thank you to my friends inside the lab for providing much needed fun times and silliness.

I specially want to thank my family who always support me from anywhere in the world and from the beginning provided me with a strong foundation to pursue the things I love, even if they take me far away. Finally, I thank Felix for his enduring love and ability to make me smile no matter what.

8. References

Absinta, M., Ha, S.K., Nair, G., Sati, P., Luciano, N.J., Palisoc, M., Louveau, A., Zaghloul, K.A., Pittaluga, S., Kipnis, J.*, et al.* (2017). Human and nonhuman primate meninges harbor lymphatic vessels that can be visualized noninvasively by MRI. Elife *6*.

Aguzzi, A., Barres, B.A., and Bennett, M.L. (2013). Microglia: scapegoat, saboteur, or something else? Science *339*, 156-161.

Ajami, B., Bennett, J.L., Krieger, C., Tetzlaff, W., and Rossi, F.M. (2007). Local self-renewal can sustain CNS microglia maintenance and function throughout adult life. Nature Neuroscience *10*, 1538-1543.

Amir, E.-a.D. (2014). THESIS: viSNE and Wanderlust, two algorithms for the visualization and analysis of high-dimensional single-cell data. In Biological Sciences (Columbia University).

Amir, E.-a.D., Davis, K.L., Tadmor, M.D., Simonds, E.F., Levine, J.H., Bendall, S.C., Shenfeld, D.K., Krishnaswamy, S., Nolan, G.P., and Pe'er, D. (2013). viSNE enables visualization of high dimensional single-cell data and reveals phenotypic heterogeneity of leukemia. Nature biotechnology *31*, 545-552.

Amsalem, H., Kwan, M., Hazan, A., Zhang, J., Jones, R.L., Whittle, W., Kingdom, J.C.P., Croy, B.A., Lye, S.J., and Dunk, C.E. (2014). Identification of a Novel Neutrophil Population: Proangiogenic Granulocytes in Second-Trimester Human Decidua. The Journal of Immunology *193*, 3070-3079.

Anandasabapathy, N., Victora, G.D., Meredith, M., Feder, R., Dong, B., Kluger, C., Yao, K., Dustin, M.L., Nussenzweig, M.C., Steinman, R.M.*, et al.* (2011). Flt3L controls the development of radiosensitive dendritic cells in the meninges and choroid plexus of the steady-state mouse brain. The Journal of Experimental Medicine *208*, 1695-1705.

Anderson, K.G., Mayer-Barber, K., Sung, H., Beura, L., James, B.R., Taylor, J.J., Qunaj, L., Griffith, T.S., Vezys, V., Barber, D.L.*, et al.* (2014). Intravascular staining for discrimination of vascular and tissue leukocytes. Nature Protocols *9*, 209-222.

Arvaniti, E., and Claassen, M. (2017). Sensitive detection of rare disease-associated cell subsets via representation learning. Nature Communications *8*, 14825.

Aspelund, a., Antila, S., Proulx, S.T., Karlsen, T.V., Karaman, S., Detmar, M., Wiig, H., and Alitalo, K. (2015). A dural lymphatic vascular system that drains brain interstitial fluid and macromolecules. Journal of Experimental Medicine *212*.

Bandura, D.R., Baranov, V.I., Ornatsky, O.I., Antonov, A., Kinach, R., Lou, X., Pavlov, S., Vorobiev, S., Dick, J.E., and Tanner, S.D. (2009). Mass Cytometry: A Novel Technique for Real-Time Single Cell Multi-Target Immunoassay Based on Inductively Coupled Plasma Time of Flight Mass Spectrometry. Analytical Chemistry *81*, 6813-6822.

Becher, B., Bechmann, I., and Greter, M. (2006). Antigen presentation in autoimmunity and CNS inflammation: how T lymphocytes recognize the brain. Journal of Molecular Medicine *84*, 532-543.

Becher, B., Durell, B.G., Miga, a.V., Hickey, W.F., and Noelle, R.J. (2001). The clinical course of experimental autoimmune encephalomyelitis and inflammation is controlled by the expression of CD40 within the central nervous system. The Journal of experimental medicine *193*, 967-974.

Becher, B., Durell, B.G., and Noelle, R.J. (2003). IL-23 produced by CNS-resident cells controls T cell encephalitogenicity during the effector phase of experimental autoimmune encephalomyelitis. Journal of Clinical Investigation *112*, 1186-1191.

Bechmann, I., Kwidzinski, E., Kovac, A.D., Simburger, E., Horvath, T., Gimsa, U., Dirnagl, U., Priller, J., and Nitsch, R. (2001). Turnover of rat brain perivascular cells. Experimental Neurology *168*, 242-249.

Bendall, S.C., Davis, K.L., Amir, E.A.D., Tadmor, M.D., Simonds, E.F., Chen, T.J., Shenfeld, D.K., Nolan, G.P., and Pe'Er, D. (2014). Single-cell trajectory detection uncovers progression and regulatory coordination in human b cell development. Cell *157*, 714-725.

Bendall, S.C., Nolan, G.P., Roederer, M., and Chattopadhyay, P.K. (2012). A deep profiler's guide to cytometry. Trends in immunology *33*, 323-332.

Bendall, S.C., Simonds, E.F., Qiu, P., Amir, E.-a.D., Krutzik, P.O., Finck, R., Bruggner, R.V., Melamed, R., Trejo, A., Ornatsky, O.I*., et al.* (2011). Single-Cell Mass Cytometry of Differential Immune and Drug Responses Across a Human Hematopoietic Continuum. Science *332*, 687-696.

Benilova, I., Karran, E., and De Strooper, B. (2012). The toxic Abeta oligomer and Alzheimer's disease: an emperor in need of clothes. Nature Neuroscience *15*, 349-357.

Bruggner, R.V., Bodenmiller, B., Dill, D.L., Tibshirani, R.J., and Nolan, G.P. (2014). Automated identification of stratifying signatures in cellular subpopulations. Proceedings of the National Academy of Sciences of the United States of America *111*, E2770-2777.

Buttgereit, A., Lelios, I., Yu, X., Vrohlings, M., Krakoski, N.R., Gautier, E.L., Nishinakamura, R., Becher, B., and Greter, M. (2016). Sall1 is a transcriptional regulator defining microglia identity and function. Nature Immunology *17*, 1397-1406.

Checchin, D., Sennlaub, F., Levavasseur, E., Leduc, M., and Chemtob, S. (2006). Potential role of microglia in retinal blood vessel formation. Investigative Ophthalmology & Visual Science *47*, 3595-3602.

Cheng, Y., Wong, M.T., van der Maaten, L., and Newell, E.W. (2016). Categorical Analysis of Human T Cell Heterogeneity with One-Dimensional Soli-Expression by Nonlinear Stochastic Embedding. Journal of Immunology *196*, 924-932.

Chevrier, S., Crowell, H., Zanotelli, V.R.T., Engler, S., Robinson, M.D., and Bodenmiller, B. (2017a). Channel crosstalk correction in suspension and imaging mass cytometry. bioRxiv.

Chevrier, S., Levine, J.H., Zanotelli, V.R.T., Silina, K., Schulz, D., Bacac, M., Ries, C.H., Ailles, L., Jewett, M.A.S., Moch, H.*, et al.* (2017b). An Immune Atlas of Clear Cell Renal Cell Carcinoma. Cell *169*, 736-749.e718.

Clemente-Casares, X., Hosseinzadeh, S., Barbu, I., Dick, S.A., Macklin, J.A., Wang, Y., Momen, A., Kantores, C., Aronoff, L., Farno, M.*, et al.* (2017). A CD103(+) Conventional Dendritic Cell Surveillance System Prevents Development of Overt Heart Failure during Subclinical Viral Myocarditis. Immunity *47*, 974-989 e978.

Codarri, L., Greter, M., and Becher, B. (2013). Communication between pathogenic T cells and myeloid cells in neuroinflammatory disease. Trends in immunology *34*, 114-119.

Colonna, M., and Butovsky, O. (2017). Microglia Function in the Central Nervous System During Health and Neurodegeneration. Annual Review of Immunology *35*, 441-468.

Compston, A., and Coles, A. (2008). Multiple sclerosis. Lancet *372*, 1502-1517.

Condello, C., Yuan, P., and Grutzendler, J. (2017). Microglia-Mediated Neuroprotection, TREM2, and Alzheimer's Disease: Evidence From Optical Imaging. Biological Psychiatry.

Condello, C., Yuan, P., Schain, A., and Grutzendler, J. (2015). Microglia constitute a barrier that prevents neurotoxic protofibrillar Abeta42 hotspots around plaques. Nature Communications *6*, 6176.

Cossarizza, A., Chang, H.D., Radbruch, A., Andra, I., Annunziato, F., Bacher, P., Barnaba, V., Battistini, L., Bauer, W.M., Baumgart, S.*, et al.* (2017). Guidelines for the use of flow cytometry and cell sorting in immunological studies. Eur J Immunol *47*, 1584-1797.

Croxford, A.L., Lanzinger, M., Hartmann, F.J., Schreiner, B., Mair, F., Pelczar, P., Clausen, B.E., Jung, S., Greter, M., and Becher, B. (2015a). The Cytokine GM-CSF Drives the Inflammatory Signature of CCR2+ Monocytes and Licenses Autoimmunity. Immunity *43*, 502-514.

Croxford, A.L., Spath, S., and Becher, B. (2015b). GM-CSF in Neuroinflammation: Licensing Myeloid Cells for Tissue Damage. Trends in Immunology *36*, 651-662.

David, D.C. (2012). Aging and the aggregating proteome. Frontiers in Genetics *3*, 1-6.

Davies, L.C., Jenkins, S.J., Allen, J.E., and Taylor, P.R. (2013). Tissue-resident macrophages. Nature Immunology *14*, 986-995.

Deleidi, M., Jäggle, M., and Rubino, G. (2015). Immune aging, dysmetabolism, and inflammation in neurological diseases. Frontiers in neuroscience *9*, 172.

Dendrou, C.A., Fugger, L., and Friese, M.A. (2015). Immunopathology of multiple sclerosis. Nature Reviews Immunology *15*, 545-558.

Diggins, K.E., Ferrell, P.B., and Irish, J.M. (2015). Methods for discovery and characterization of cell subsets in high dimensional mass cytometry data. Methods *82*, 55-63.

Diggins, K.E., Greenplate, A.R., Leelatian, N., Wogsland, C.E., and Irish, J.M. (2017). Characterizing cell subsets using marker enrichment modeling. Nature Methods *14*, 275-278.

Elobeid, A., Libard, S., Leino, M., Popova, S.N., and Alafuzoff, I. (2016). Altered Proteins in the Aging Brain. Journal of Neuropathology & Experimental Neurology *75*, 316-325.

Engelhardt, B., Vajkoczy, P., and Weller, R.O. (2017). The movers and shapers in immune privilege of the CNS. Nature Immunology *18*, 123-131.

Epelman, S., Lavine, K.J., Beaudin, A.E., Sojka, D.K., Carrero, J.A., Calderon, B., Brija, T., Gautier, E.L., Ivanov, S., Satpathy, A.T.*, et al.* (2014). Embryonic and adult-derived resident cardiac macrophages are maintained through distinct mechanisms at steady state and during inflammation. Immunity *40*.

Everts, B., Tussiwand, R., Dreesen, L., Fairfax, K.C., Huang, S.C., Smith, A.M., O'Neill, C.M., Lam, W.Y., Edelson, B.T., Urban, J.F., Jr.*, et al.* (2016). Migratory CD103+ dendritic cells suppress helminth-driven type 2 immunity through constitutive expression of IL-12. Journal of Experimental Medicine *213*, 35-51.

Fienberg, H.G., Simonds, E.F., Fantl, W.J., Nolan, G.P., and Bodenmiller, B. (2012). A platinum-based covalent viability reagent for single-cell mass cytometry. Cytometry Part A *81 A*, 467-475.

Finak, G., Perez, J.M., Weng, A., and Gottardo, R. (2010). Optimizing transformations for automated, high throughput analysis of flow cytometry data. BMC Bioinformatics *11*, 546.

Finck, R., Simonds, E.F., Jager, A., Krishnaswamy, S., Sachs, K., Fantl, W., Pe'er, D., Nolan, G.P., and Bendall, S.C. (2013). Normalization of mass cytometry data with bead standards. Cytometry Part A *83 A*, 483-494.

Fulwyler, M.J. (1965). Electronic Separation of Biological Cells by Volume. Science *150*, 910-911.

Galea, I., Bechmann, I., and Perry, V.H. (2007). What is immune privilege (not)? Trends in Immunology *28*, 12-18.

Gautier, E.L., Shay, T., Miller, J., Greter, M., Jakubzick, C., Ivanov, S., Helft, J., Chow, A., Elpek, K.G., Gordonov, S.*, et al.* (2012). Gene-expression profiles and transcriptional regulatory pathways that underlie the identity and diversity of mouse tissue macrophages. Nature Immunology *13*, 1118-1128.

Gentleman, R.C., Carey, V.J., Bates, D.M., Bolstad, B., Dettling, M., Dudoit, S., Ellis, B., Gautier, L., Ge, Y., Gentry, J.*, et al.* (2004). Bioconductor: open software development for computational biology and bioinformatics. Genome Biol *5*, R80.

Ginhoux, F., Greter, M., Leboeuf, M., Nandi, S., See, P., Gokhan, S., Mehler, M.F., Conway, S.J., Ng, L.G., Stanley, E.R.*, et al.* (2010). Fate mapping analysis reveals that adult microglia derive from primitive macrophages. Science (New York, NY) *330*, 841-845.

Goldmann, T., Wieghofer, P., Jordão, M.J.C., Prutek, F., Hagemeyer, N., Frenzel, K., Amann, L., Staszewski, O., Kierdorf, K., Krueger, M.*, et al.* (2016). Origin, fate and dynamics of macrophages at central nervous system interfaces. Nature Immunology *17*, 797-805.

Gomez Perdiguero, E., Klapproth, K., Schulz, C., Busch, K., Azzoni, E., Crozet, L., Garner, H., Trouillet, C., de Bruijn, M.F., Geissmann, F.*, et al.* (2015). Tissue-resident macrophages originate from yolk-sac-derived erythro-myeloid progenitors. Nature *518*, 547-551.

Grathwohl, S.A., Kalin, R.E., Bolmont, T., Prokop, S., Winkelmann, G., Kaeser, S.A., Odenthal, J., Radde, R., Eldh, T., Gandy, S.*, et al.* (2009). Formation and maintenance of Alzheimer's disease beta-amyloid plaques in the absence of microglia. Nat Neurosci *12*, 1361-1363.

Gray, J.W., Carrano, A.V., Steinmetz, L.L., Van Dilla, M.A., Moore, D.H., Mayall, B.H., and Mendelsohn, M.L. (1975). Chromosome measurement and sorting by flow systems. Proceedings of the National Academy of Sciences *72*, 1231-1234.

Greter, M., Heppner, F.L., Lemos, M.P., Odermatt, B.M., Goebels, N., Laufer, T., Noelle, R.J., and Becher, B. (2005). Dendritic cells permit immune invasion of the CNS in an animal model of multiple sclerosis. Nature medicine *11*, 328-334.

Guerreiro, R., Wojtas, A., Bras, J., Carrasquillo, M., Rogaeva, E., Majounie, E., Cruchaga, C., Sassi, C., Kauwe, J.S., Younkin, S.*, et al.* (2013). TREM2 variants in Alzheimer's disease. New England Journal of Medicine *368*, 117-127.

Guilliams, M., Dutertre, C.-A., Scott, Charlotte L., McGovern, N., Sichien, D., Chakarov, S., Van Gassen, S., Chen, J., Poidinger, M., De Prijck, S.*, et al.* (2016). Unsupervised High-Dimensional Analysis Aligns Dendritic Cells across Tissues and Species. Immunity *45*, 669-684.

Hanisch, U.K., and Kettenmann, H. (2007). Microglia: active sensor and versatile effector cells in the normal and pathologic brain. Nature Neuroscience *10*, 1387-1394.

Hartmann, F.J., Bernard-Valnet, R., Quériault, C., Mrdjen, D., Weber, L.M., Galli, E., Krieg, C., Robinson, M.D., Nguyen, X.-H., Dauvilliers, Y.*, et al.* (2016). High-dimensional single-cell analysis reveals the immune signature of narcolepsy. The Journal of Experimental Medicine *213*, 2621-2633.

Hawkes, C.A., and McLaurin, J. (2009). Selective targeting of perivascular macrophages for clearance of beta-amyloid in cerebral amyloid angiopathy. Proc Natl Acad Sci U S A *106*, 1261-1266.

Hellwig, S., Masuch, A., Nestel, S., Katzmarski, N., Meyer-Luehmann, M., and Biber, K. (2015). Forebrain microglia from wild-type but not adult 5xFAD mice prevent amyloid-beta plaque formation in organotypic hippocampal slice cultures. Science Reports *5*, 14624.

Heppner, F.L., Greter, M., Marino, D., Falsig, J., Raivich, G., Hövelmeyer, N., Waisman, A., Rülicke, T., Prinz, M., Priller, J.*, et al.* (2005). Experimental autoimmune encephalomyelitis repressed by microglial paralysis. Nature medicine *11*, 146-152.

Heppner, F.L., Ransohoff, R.M., and Becher, B. (2015). Immune attack: the role of inflammation in Alzheimer disease. Nature Reviews Neuroscience *16*, 358-372.

Herz, J., Filiano, A.J., Smith, A., Yogev, N., and Kipnis, J. (2017). Review Myeloid Cells in the Central Nervous System. Immunity *46*, 943-956.

Herzenberg, L.A., Tung, J., Moore, W.A., and Parks, D.R. (2006). Interpreting flow cytometry data: a guide for the perplexed. Nature Immunology *7*, 681-685.

Hickman, S.E., Kingery, N.D., Ohsumi, T.K., Borowsky, M.L., Wang, L.C., Means, T.K., and El Khoury, J. (2013). The microglial sensome revealed by direct RNA sequencing. Nature Neuroscience *16*, 1896-1905.

Hoeffel, G., Chen, J., Lavin, Y., Low, D., Almeida, F.F., See, P., Beaudin, A.E., Lum, J., Low, I., Forsberg, E.C.*, et al.* (2015). C-Myb(+) erythro-myeloid progenitor-derived fetal monocytes give rise to adult tissue-resident macrophages. Immunity *42*, 665-678.

Houk, R.S., Fassel, V.A., Flesch, G.D., Svec, H.J., Gray, A.L., and Taylor, C.E. (1980). Inductively coupled argon plasma as an ion source for mass spectrometric determination of trace elements. Analytical Chemistry *52*, 2283-2289.

Idoyaga, J., Fiorese, C., Zbytnuik, L., Lubkin, A., Miller, J., Malissen, B., Mucida, D., Merad, M., and Steinman, R.M. (2013). Specialized role of migratory dendritic cells in peripheral tolerance induction. Journal of Clinical Investigation *123*, 844-854.

Jacomy, M., Venturini, T., Heymann, S., and Bastian, M. (2014). ForceAtlas2, a continuous graph layout algorithm for handy network visualization designed for the Gephi software. PLoS One *9*, e98679.

Jonsson, T., Stefansson, H., Steinberg, S., Jonsdottir, I., Jonsson, P.V., Snaedal, J., Bjornsson, S., Huttenlocher, J., Levey, A.I., Lah, J.J.*, et al.* (2013). Variant of TREM2 associated with the risk of Alzheimer's disease. New England Journal of Medicine *368*, 107-116.

Kalaria, R.N., Premkumar, D.R.D., Pax, A.B., Cohen, D.L., and Lieberburg, I. (1996). Production and increased detection of amyloid β protein and amyloidogenic fragments in brain microvessels, meningeal vessels and choroid plexus in Alzheimer's disease. Molecular Brain Research *35*, 58-68.

Kang, J., Park, K.H., Kim, J.J., Jo, E.K., Han, M.K., and Kim, U.H. (2012). The role of CD38 in Fcγ receptor (FcγR)-mediated phagocytosis in murine macrophages. Journal of Biological Chemistry *287*, 14502-14514.

Keren-Shaul, H., Spinrad, A., Weiner, A., Matcovitch-Natan, O., Dvir-Szternfeld, R., Ulland, T.K., David, E., Baruch, K., Lara-Astaiso, D., Toth, B.*, et al.* (2017). A Unique Microglia Type Associated with Restricting Development of Alzheimer's Disease. Cell *169*, 1276-1290.e1217.

Kettenmann, H., Kirchhoff, F., and Verkhratsky, A. (2013). Microglia: new roles for the synaptic stripper. Neuron *77*, 10-18.

Kida, S., Steart, P.V., Zhang, E.-T., and Weller, R.O. (1993). Perivascular cells act as scavengers in the cerebral perivascular spaces and remain distinct from pericytes, microglia and macrophages. Acta Neuropathologica *85*, 646-652.

Kierdorf, K., Katzmarski, N., Haas, C.A., and Prinz, M. (2013). Bone marrow cell recruitment to the brain in the absence of irradiation or parabiosis bias. PLoS One *8*, e58544.

King, I.L., Kroenke, M.a., and Segal, B.M. (2010). GM-CSF-dependent, CD103+ dermal dendritic cells play a critical role in Th effector cell differentiation after subcutaneous immunization. The Journal of experimental medicine *207*, 953-961.

Kingston, D., Schmid, M.A., Onai, N., Obata-Onai, A., Baumjohann, D., and Manz, M.G. (2009). The concerted action of GM-CSF and Flt3-ligand on in vivo dendritic cell homeostasis. Blood *114*, 835-843.

Kivisäkk, P., Imitola, J., Rasmussen, S., Elyaman, W., Zhu, B., Ransohoff, R.M., and Khoury, S.J. (2009). Localizing central nervous system immune surveillance: Meningeal antigen-presenting cells activate T cells during experimental autoimmune encephalomyelitis. Annals of Neurology *65*, 457-469.

Kohonen, T. (1990). The self-organizing map. Proceedings of the IEEE *78*, 1464-1480.

Koning, N., Bo, L., Hoek, R.M., and Huitinga, I. (2007). Downregulation of macrophage inhibitory molecules in multiple sclerosis lesions. Annals of Neurology *62*, 504-514.

Korin, B., Ben-Shaanan, T.L., Schiller, M., Dubovik, T., Azulay-Debby, H., Boshnak, N.T., Koren, T., and Rolls, A. (2017). High-dimensional, single-cell characterization of the brain's immune compartment. Nature Neuroscience.

Kotecha, N., Krutzik, P.O., and Irish, J.M. (2010). Web-Based Analysis and Publication of Flow Cytometry Experiments. In Current Protocols in Cytometry (Hoboken, NJ, USA: John Wiley & Sons, Inc.), pp. 1-24.

Krasemann, S., Madore, C., Cialic, R., Baufeld, C., Calcagno, N., El Fatimy, R., Beckers, L., O'Loughlin, E., Xu, Y., Fanek, Z.*, et al.* (2017). The TREM2-APOE Pathway Drives the Transcriptional Phenotype of Dysfunctional Microglia in Neurodegenerative Diseases. Immunity *47*, 566-581 e569.

Levine, J.H., Simonds, E.F., Bendall, S.C., Davis, K.L., Amir, E.-a.D., Tadmor, M.D., Litvin, O., Fienberg, H.G., Jager, A., Zunder, E.R.*, et al.* (2015). Data-Driven Phenotypic Dissection of AML Reveals Progenitor-like Cells that Correlate with Prognosis. Cell *162*, 184-197.

Liu, K., Victora, G.D., Schwickert, T.A., Guermonprez, P., Meredith, M.M., Yao, K., Chu, F.F., Randolph, G.J., Rudensky, A.Y., and Nussenzweig, M. (2009). In vivo analysis of dendritic cell development and homeostasis. Science *324*, 392-397.

Liu, K., Waskow, C., Liu, X., Yao, K., Hoh, J., and Nussenzweig, M. (2007). Origin of dendritic cells in peripheral lymphoid organs of mice. Nat Immunol *8*, 578-583.

Lodygin, D., Odoardi, F., Schlager, C., Korner, H., Kitz, A., Nosov, M., van den Brandt, J., Reichardt, H.M., Haberl, M., and Flugel, A. (2013). A combination of fluorescent NFAT and H2B sensors uncovers dynamics of T cell activation in real time during CNS autoimmunity. Nature Medicine *19*, 784-790.

Lou, X., Zhang, G., Herrera, I., Kinach, R., Ornatsky, O., Baranov, V., Nitz, M., and Winnik, M.A. (2007). Polymer-based elemental tags for sensitive bioassays. Angew Chem Int Ed Engl *46*, 6111-6114.

Louveau, A., Smirnov, I., Keyes, T.J., Eccles, J.D., Rouhani, S.J., Peske, J.D., Derecki, N.C., Castle, D., Mandell, J.W., Lee, K.S.*, et al.* (2015). Structural and functional features of central nervous system lymphatic vessels. Nature *523*, 337-341.

Lucin, K.M., and Wyss-Coray, T. (2009). Immune Activation in Brain Aging and Neurodegeneration: Too Much or Too Little? Neuron *64*, 110-122.

Macnair, W., Roditi, L.D.V., Ganscha, S., and Claassen, M. (2017). Tree-ensemble analysis tests for presence of multifurcations in single cell data. bioRxiv.

Maecker, H.T., McCoy, J.P., and Nussenblatt, R. (2012). Standardizing immunophenotyping for the Human Immunology Project. Nat Rev Immunol *12*, 191-200.

Mair, F., Hartmann, F.J., Mrdjen, D., Tosevski, V., Krieg, C., and Becher, B. (2016). The end of gating? An introduction to automated analysis of high dimensional cytometry data. European Journal of Immunology *46*, 34-43.

Majonis, D., Herrera, I., Ornatsky, O., Schulze, M., Lou, X., Soleimani, M., Nitz, M., and Winnik, M.A. (2010). Synthesis of a functional metal-chelating polymer and steps toward quantitative mass cytometry bioassays. Anal Chem *82*, 8961-8969.

Majonis, D., Ornatsky, O., Kinach, R., and Winnik, M.A. (2011). Curious results with palladium- and platinum-carrying polymers in mass cytometry bioassays and an unexpected application as a dead cell stain. Biomacromolecules *12*, 3997-4010.

Majumdar, A., Chung, H., Dolios, G., Wang, R., Asamoah, N., Lobel, P., and Maxfield, F.R. (2008). Degradation of fibrillar forms of Alzheimer's amyloid beta-peptide by macrophages. Neurobiology of Aging *29*, 707-715.

Maraskovsky, E., Brasel, K., Teepe, M., Roux, E.R., Lyman, S.D., Shortman, K., and McKenna, H.J. (1996). Dramatic increase in the numbers of functionally mature dendritic cells in Flt3 ligand-treated mice: multiple dendritic cell subpopulations identified. The Journal of experimental medicine *184*, 1953-1962.

Mato, M., Ookawara, S., Sakamoto, A., Aikawa, E., Ogawa, T., Mitsuhashi, U., Masuzawa, T., Suzuki, H., Honda, M., Yazaki, Y.*, et al.* (1996). Involvement of specific macrophage-lineage cells surrounding arterioles in barrier and scavenger function in brain cortex. Proceedings of the National Academy of Sciences *93*, 3269-3274.

Matyszak, M.K., Lawson, L.J., Perry, V.H., and Gordon, S. (1992). Stromal macrophages of the choroid plexus situated at an interface between the brain and peripheral immune system constitutively express major histocompatibility class II antigens. Journal of Neuroimmunology *40*, 173-181.

Matyszak, M.K., and Perry, V.H. (1996a). A comparison of leucocyte responses to heat-killed bacillus Calmette-Guérin in different CNS compartments. Neuropathology and applied neurobiology *22*, 44-53.

Matyszak, M.K., and Perry, V.H. (1996b). The potential role of dendritic cells in immune-mediated inflammatory diseases in the central nervous system. Neuroscience *74*, 599-608.

McGovern, N., Shin, A., Low, G., Low, D., Duan, K., Yao, L.J., Msallam, R., Low, I., Shadan, N.B., Sumatoh, H.R.*, et al.* (2017). Human fetal dendritic cells promote prenatal T-cell immune suppression through arginase-2. Nature.

McMenamin, P.G. (1999). Distribution and phenotype of dendritic cells and resident tissue macrophages in the dura mater, leptomeninges, and choroid plexus of the rat brain as demonstrated in wholemount preparations. The Journal of comparative neurology *405*, 553-562.

Mei, H.E., Leipold, M.D., and Maecker, H.T. (2016). Platinum-conjugated antibodies for application in mass cytometry. Cytometry Part A *89*, 292-300.

Mei, H.E., Leipold, M.D., Schulz, a.R., Chester, C., and Maecker, H.T. (2015). Barcoding of Live Human Peripheral Blood Mononuclear Cells for Multiplexed Mass Cytometry. The Journal of Immunology *194*, 2022-2031.

Merad, M., and Manz, M.G. (2009). Review article Dendritic cell homeostasis. Cell *113*, 3418-3427.

Merad, M., Sathe, P., Helft, J., Miller, J., and Mortha, A. (2013). The dendritic cell lineage: ontogeny and function of dendritic cells and their subsets in the steady state and the inflamed setting. Annual review of immunology *31*, 563-604.

Meyer-Luehmann, M., Spires-Jones, T.L., Prada, C., Garcia-Alloza, M., de Calignon, A., Rozkalne, A., Koenigsknecht-Talboo, J., Holtzman, D.M., Bacskai, B.J., and Hyman, B.T. (2008). Rapid appearance and local toxicity of amyloid-beta plaques in a mouse model of Alzheimer's disease. Nature *451*, 720-724.

Mildner, A., Schmidt, H., Nitsche, M., Merkler, D., Hanisch, U.-K., Mack, M., Heikenwalder, M., Brück, W., Priller, J., and Prinz, M. (2007). Microglia in the adult brain arise from Ly-6ChiCCR2+ monocytes only under defined host conditions. Nature neuroscience *10*, 1544-1553.

Mossadegh-Keller, N., Gentek, R., Gimenez, G., Bigot, S., Mailfert, S., and Sieweke, M.H. (2017). Developmental origin and maintenance of distinct testicular macrophage populations. Journal of Experimental Medicine *214*, 2829-2841.

Mrdjen, D., Hartmann, F.J., and Becher, B. (2017). High Dimensional Cytometry of Central Nervous System Leukocytes During Neuroinflammation. In Inflammation: Methods and Protocols, B.E. Clausen, and J.D. Laman, eds. (New York, NY: Springer New York), pp. 321-332.

Murphy, J.B., and Sturm, E. (1923). Conditions determining the transplantability of tissues in the brain. The Journal of experimental medicine *38*, 183-197.

Nimmerjahn, A., Kirchhoff, F., and Helmchen, F. (2005). Resting microglial cells are highly dynamic surveillants of brain parenchyma in vivo. Science *308*, 1314-1318.

Ornatsky, O., Bandura, D., Baranov, V., Nitz, M., Winnik, M.A., and Tanner, S. (2010). Highly multiparametric analysis by mass cytometry. Journal of Immunological Methods *361*, 1-20.

Ornatsky, O.I., Kinach, R., Bandura, D.R., Lou, X., Tanner, S.D., Baranov, V.I., Nitz, M., and Winnik, M.A. (2008). Development of analytical methods for multiplex bio-assay with inductively coupled plasma mass spectrometry. J Anal At Spectrom *23*, 463-469.

Owens, T., Bechmann, I., and Engelhardt, B. (2008). Perivascular spaces and the two steps to neuroinflammation. Journal of Neuropatholgy & Experimental Neurology *67*, 1113-1121.

Paolicelli, R.C., Bolasco, G., Pagani, F., Maggi, L., Scianni, M., Panzanelli, P., Giustetto, M., Ferreira, T.A., Guiducci, E., Dumas, L.*, et al.* (2011). Synaptic pruning by microglia is necessary for normal brain development. Science *333*, 1456-1458.

Parkhurst, C.N., Yang, G., Ninan, I., Savas, J.N., Yates, J.R., 3rd, Lafaille, J.J., Hempstead, B.L., Littman, D.R., and Gan, W.B. (2013). Microglia promote learning-dependent synapse formation through brain-derived neurotrophic factor. Cell *155*, 1596-1609.

Parks, D.R., Roederer, M., and Moore, W.A. (2006). A new "Logicle" display method avoids deceptive effects of logarithmic scaling for low signals and compensated data. Cytometry A *69*, 541-551.

Perfetto, S.P., Ambrozak, D., Nguyen, R., Chattopadhyay, P., and Roederer, M. (2006). Quality assurance for polychromatic flow cytometry. Nature Protocols *1*, 1522-1530.

Perry, V.H., and Holmes, C. (2014). Microglial priming in neurodegenerative disease. Nature reviews Neurology *10*, 217-224.

Peterson, V.M., Zhang, K.X., Kumar, N., Wong, J., Li, L., Wilson, D.C., Moore, R., McClanahan, T.K., Sadekova, S., and Klappenbach, J.A. (2017). Multiplexed quantification of proteins and transcripts in single cells. Nature Biotechnology *35*, 936-939.

Polfliet, M.M.J., van de Veerdonk, F., Döpp, E.A., van Kesteren-Hendrikx, E.M.L., van Rooijen, N., Dijkstra, C.D., and van den Berg, T.K. (2002). The role of perivascular and meningeal macrophages in experimental allergic encephalomyelitis. Journal of Neuroimmunology *122*, 1-8.

Prinz, M., Erny, D., and Hagemeyer, N. (2017). Ontogeny and homeostasis of CNS myeloid cells. Nature Immunology *18*, 385.

Prinz, M., and Priller, J. (2014). Microglia and brain macrophages in the molecular age: from origin to neuropsychiatric disease. Nature reviews Neuroscience *15*, 300-312.

Pugliatti, M., Rosati, G., Carton, H., Riise, T., Drulovic, J., Vécsei, L., and Milanov, I. (2006). The epidemiology of multiple sclerosis in Europe. European journal of neurology : the official journal of the European Federation of Neurological Societies *13*, 700-722.

Qiu, P., Simonds, E.F., Bendall, S.C., Gibbs, K.D., Jr., Bruggner, R.V., Linderman, M.D., Sachs, K., Nolan, G.P., and Plevritis, S.K. (2011). Extracting a cellular hierarchy from high-dimensional cytometry data with SPADE. Nature Biotechnology *29*, 886-891.

Radde, R., Bolmont, T., Kaeser, S.A., Coomaraswamy, J., Lindau, D., Stoltze, L., Calhoun, M.E., Jaggi, F., Wolburg, H., Gengler, S*., et al.* (2006a). Abeta42-driven cerebral amyloidosis in transgenic mice reveals early and robust pathology. EMBO Reports *7*, 940-946.

Radde, R., Bolmont, T., Kaeser, S.A., Coomaraswamy, J., Lindau, D., Stoltze, L., Calhoun, M.E., Jaggi, F., Wolburg, H., Gengler, S*., et al.* (2006b). Abeta42-driven cerebral amyloidosis in transgenic mice reveals early and robust pathology. EMBO Rep *7*, 940-946.

Ransohoff, R.M., and Engelhardt, B. (2012). The anatomical and cellular basis of immune surveillance in the central nervous system. Nature reviews Immunology *12*, 623-635.

Reed-Geaghan, E.G., Savage, J.C., Hise, A.G., and Landreth, G.E. (2009). CD14 and toll-like receptors 2 and 4 are required for fibrillar A{beta}-stimulated microglial activation. Journal of Neuroscience *29*, 11982-11992.

Reu, P., Khosravi, A., Bernard, S., Mold, J.E., Salehpour, M., Alkass, K., Perl, S., Tisdale, J., Possnert, G., Druid, H*., et al.* (2017). The Lifespan and Turnover of Microglia in the Human Brain. Cell Reports *20*, 779-784.

Robinson, J.P., and Roederer, M. (2015). Flow cytometry strikes gold. Science *350*, 739-740.

Roumier, A., Bechade, C., Poncer, J.C., Smalla, K.H., Tomasello, E., Vivier, E., Gundelfinger, E.D., Triller, A., and Bessis, A. (2004). Impaired synaptic function in the microglial KARAP/DAP12-deficient mouse. Journal of Neuroscience *24*, 11421-11428.

Saeys, Y., Gassen, S.V., and Lambrecht, B.N. (2016). Computational flow cytometry: helping to make sense of high-dimensional immunology data. Nature Reviews Immunology.

Safaiyan, S., Kannaiyan, N., Snaidero, N., Brioschi, S., Biber, K., Yona, S., Edinger, A.L., Jung, S., Rossner, M.J., and Simons, M. (2016). Age-related myelin degradation burdens the clearance function of microglia during aging. Nature Neurosciience *19*, 995-998.

Salter, M.W., and Beggs, S. (2014). Sublime microglia: expanding roles for the guardians of the CNS. Cell *158*, 15-24.

Samusik, N., Good, Z., Spitzer, M.H., Davis, K.L., and Nolan, G.P. (2016). Automated mapping of phenotype space with single-cell data. Nature Methods *13*, 493-496.

Savina, A., and Amigorena, S. (2007). Phagocytosis and antigen presentation in dendritic cells. Immunological Reviews *219*, 143-156.

Schläger, C., Körner, H., Krueger, M., Vidoli, S., Haberl, M., Mielke, D., Brylla, E., Issekutz, T., Cabañas, C., Nelson, P.J.*, et al.* (2016). Effector T-cell trafficking between the leptomeninges and the cerebrospinal fluid. Nature *530*, 349-353.

Schlitzer, A., McGovern, N., Teo, P., Zelante, T., Atarashi, K., Low, D., Ho, A.W., See, P., Shin, A., Wasan, P.S.*, et al.* (2013a). IRF4 transcription factor-dependent CD11b+ dendritic cells in human and mouse control mucosal IL-17 cytokine responses. Immunity *38*, 970-983.

Schlitzer, A., McGovern, N., Teo, P., Zelante, T., Atarashi, K., Low, D., Ho, A.W.S., See, P., Shin, A., Wasan, P.S.*, et al.* (2013b). IRF4 transcription factor-dependent CD11b+ dendritic cells in human and mouse control mucosal IL-17 cytokine responses. Immunity *38*, 970-983.

Schlitzer, A., Sivakamasundari, V., Chen, J., Sumatoh, H.R.B., Schreuder, J., Lum, J., Malleret, B., Zhang, S., Larbi, A., Zolezzi, F.*, et al.* (2015). Identification of cDC1- and cDC2-committed DC progenitors reveals early lineage priming at the common DC progenitor stage in the bone marrow. Nature Immunology, 1-13.

Schreiner, B., Heppner, F.L., and Becher, B. (2009). Modeling multiple sclerosis in laboratory animals. Seminars in Immunopathology *31*, 479-495.

Serafini, B., Rosicarelli, B., Magliozzi, R., Stigliano, E., Capello, E., Mancardi, G.L., and Aloisi, F. (2006). Dendritic cells in multiple sclerosis lesions: maturation stage, myelin uptake, and interaction with proliferating T cells. Journal of neuropathology and experimental neurology *65*, 124-141.

Setty, M., Tadmor, M.D., Reich-Zeliger, S., Angel, O., Salame, T.M., Kathail, P., Choi, K., Bendall, S., Friedman, N., and Pe'er, D. (2016). Wishbone identifies bifurcating developmental trajectories from single-cell data. Nature Biotechnology.

Shechter, R., London, A., and Schwartz, M. (2013a). Orchestrated leukocyte recruitment to immune-privileged sites: absolute barriers versus educational gates. Nat Rev Immunol *13*, 206-218.

Shechter, R., Miller, O., Yovel, G., Rosenzweig, N., London, A., Ruckh, J., Kim, K.W., Klein, E., Kalchenko, V., Bendel, P.*, et al.* (2013b). Recruitment of Beneficial M2 Macrophages to Injured Spinal Cord Is Orchestrated by Remote Brain Choroid Plexus. Immunity *38*, 555-569.

Shirai, Y. (1921). On the transplant of the rat sarcoma in adult heterogenous animals. Japan Medical World, 14-15.

Sica, A., and Mantovani, A. (2012). Macrophage plasticity and polarization: in vivo veritas. The Journal of Clinical Investigation *122*, 787-795.

Spath, S., Komuczki, J., Hermann, M., Pelczar, P., Mair, F., Schreiner, B., and Becher, B. (2017). Dysregulation of the Cytokine GM-CSF Induces Spontaneous Phagocyte Invasion and Immunopathology in the Central Nervous System. Immunity *46*, 245-260.

Spitzer, M.H., Carmi, Y., Reticker-Flynn, N.E., Kwek, S.S., Madhireddy, D., Martins, M.M., Gherardini, P.F., Prestwood, T.R., Chabon, J., Bendall, S.C.*, et al.* (2017). Systemic Immunity Is Required for Effective Cancer Immunotherapy. Cell *168*, 487-502 e415.

Spitzer, M.H., Gherardini, P.F., Fragiadakis, G.K., Bhattacharya, N., Yuan, R.T., Hotson, A.N., Finck, R., Carmi, Y., Zunder, E.R., Fantl, W.J.*, et al.* (2015). An interactive reference framework for modeling a dynamic immune system. Science *349*, 1259425.

Stevens, S.M., von Gise, A., VanDusen, N., Zhou, B., and Pu, W.T. (2016). Epicardium is required for cardiac seeding by yolk sac macrophages, precursors of resident macrophages of the adult heart. Develomental Biology *413*, 153-159.

Streit, W.J., Braak, H., Xue, Q.S., and Bechmann, I. (2009). Dystrophic (senescent) rather than activated microglial cells are associated with tau pathology and likely precede neurodegeneration in Alzheimer's disease. Acta Neuropathologica *118*, 475-485.

Streit, W.J., Sammons, N.W., Kuhns, A.J., and Sparks, D.L. (2004). Dystrophic microglia in the aging human brain. Glia *45*, 208-212.

Sudo, T., Nishikawa, S., Ogawa, M., Kataoka, H., Ohno, N., Izawa, A., Hayashi, S., and Nishikawa, S. (1995). Functional hierarchy of c-kit and c-fms in intramarrow production of CFU-M. Oncogene *11*, 2469-2476.

Tanner, S.D., Baranov, V.I., Ornatsky, O.I., Bandura, D.R., and George, T.C. (2013). An introduction to mass cytometry: fundamentals and applications. Cancer immunology, immunotherapy : CII *62*, 955-965.

Tremblay, M.E., Lowery, R.L., and Majewska, A.K. (2010). Microglial interactions with synapses are modulated by visual experience. PLoS Biol *8*, e1000527.

Trotter, J. (2007). Alternatives to log-scale data display. Current Protocols in Cytometry *Chapter 10*, Unit 10.16.

Tussiwand, R., Everts, B., Grajales-Reyes, G., Kretzer, N., Iwata, A., Bagaitkar, J., Wu, X., Wong, R., Anderson, D., Murphy, T.*, et al.* (2015). Klf4 expression in conventional dendritic cells is required for T helper 2 cell responses: Supplement. Immunity *42*, 916-928.

Ulrich, J.D., Ulland, T.K., Colonna, M., and Holtzman, D.M. (2017). Elucidating the Role of TREM2 in Alzheimer's Disease. Neuron *94*, 237-248.

van der Maaten, L. (2013). Barnes-Hut-SNE (ARXIV), pp. 1-11.

Van Der Maaten, L., and Hinton, G. (2008). Visualizing Data using t-SNE. Journal of Machine Learning Research *9*, 2579-2605.

Van Gassen, S., Callebaut, B., Van Helden, M.J., Lambrecht, B.N., Demeester, P., Dhaene, T., and Saeys, Y. (2015). FlowSOM: Using self-organizing maps for visualization and interpretation of cytometry data. Cytometry Part A *87*, 636-645.

Vercellino, M., Trebini, C., Capello, E., Mancardi, G.L., Giordana, M.T., and Cavalla, P. (2017). Inflammatory responses in Multiple Sclerosis normal-appearing white matter and in non-immune mediated neurological conditions with wallerian axonal degeneration: A comparative study. J Neuroimmunol *312*, 49-58.

Vom Berg, J., Prokop, S., Miller, K.R., Obst, J., Kälin, R.E., Lopategui-Cabezas, I., Wegner, A., Mair, F., Schipke, C.G., Peters, O.*, et al.* (2012). Inhibition of IL-12/IL-23 signaling reduces Alzheimer's disease-like pathology and cognitive decline. Nature medicine *18*, 1812-1819.

Waskow, C., Liu, K., Darrasse-Jeze, G., Guermonprez, P., Ginhoux, F., Merad, M., Shengelia, T., Yao, K., and Nussenzweig, M. (2008). The receptor tyrosine kinase Flt3 is required for dendritic cell development in peripheral lymphoid tissues. Nat Immunol *9*, 676-683.

Weber, L.M., and Robinson, M.D. (2016). Comparison of clustering methods for high-dimensional single-cell flow and mass cytometry data. Cytometry Part A *89*, 1084-1096.

Wynn, T.A., Chawla, A., and Pollard, J.W. (2013). Macrophage biology in development, homeostasis and disease. Nature *496*, 445-455.

Wyss-Coray, T. (2016). Ageing, neurodegeneration and brain rejuvenation. Nature *539*, 180-186.

Yamasaki, R., Lu, H., Butovsky, O., Ohno, N., Rietsch, A.M., Cialic, R., Wu, P.M., Doykan, C.E., Lin, J., Cotleur, A.C., *et al.* (2014). Differential roles of microglia and monocytes in the inflamed central nervous system. J Exp Med *211*, 1533-1549.

Yona, S., Kim, K.W., Wolf, Y., Mildner, A., Varol, D., Breker, M., Strauss-Ayali, D., Viukov, S., Guilliams, M., Misharin, A., *et al.* (2013). Fate mapping reveals origins and dynamics of monocytes and tissue macrophages under homeostasis. Immunity *38*, 79-91.

Yuan, P., Condello, C., Keene, C.D., Wang, Y., Bird, T.D., Paul, S.M., Luo, W., Colonna, M., Baddeley, D., and Grutzendler, J. (2016). TREM2 Haplodeficiency in Mice and Humans Impairs the Microglia Barrier Function Leading to Decreased Amyloid Compaction and Severe Axonal Dystrophy. Neuron *90*, 724-739.

Yuri, S., Fujimura, S., Nimura, K., Takeda, N., Toyooka, Y., Fujimura, Y., Aburatani, H., Ura, K., Koseki, H., Niwa, H., *et al.* (2009). Sall4 is essential for stabilization, but not for pluripotency, of embryonic stem cells by repressing aberrant trophectoderm gene expression. Stem Cells *27*, 796-805.

Zhan, Y., Paolicelli, R.C., Sforazzini, F., Weinhard, L., Bolasco, G., Pagani, F., Vyssotski, A.L., Bifone, A., Gozzi, A., Ragozzino, D., *et al.* (2014). Deficient neuron-microglia signaling results in impaired functional brain connectivity and social behavior. Nat Neurosci *17*, 400-406.

Zrzavy, T., Hametner, S., Wimmer, I., Butovsky, O., Weiner, H.L., and Lassmann, H. (2017). Loss of 'homeostatic' microglia and patterns of their activation in active multiple sclerosis. Brain *140*, 1900-1913.

Zunder, E.R., Finck, R., Behbehani, G.K., Amir, E.-a.D., Krishnaswamy, S., Gonzalez, V.D., Lorang, C.G., Bjornson, Z., Spitzer, M.H., Bodenmiller, B., *et al.* (2015a). Palladium-based mass tag cell barcoding with a doublet-filtering scheme and single-cell deconvolution algorithm. Nature Protocols *10*, 316-333.

Zunder, E.R., Lujan, E., Goltsev, Y., Wernig, M., and Nolan, G.P. (2015b). A continuous molecular roadmap to iPSC reprogramming through progression analysis of single-cell mass cytometry. Cell Stem Cell *16*, 323-337.